Royal Netherlands
Meteorological Institute
Ministry of Infrastructure
and Water Management

Quality analysis of the continuous data recorded by KNMI's first-generation borehole geophone network

C. Weemstra and E. Ruigrok

De Bilt, 2026| Technical report; TR 26-07

Summary

In the Netherlands, monitoring of induced seismicity by means of borehole stations dates back to the 1990's: the first "prototype" station was installed near Finsterwolde in 1991. A borehole station consist of a string of (typically four) three-component borehole geophones. Based on the positive experience with the first station near Finsterwolde, eleven additional borehole stations were installed around 1995, and another six in 2010. Together, these 18 stations constitute KNMI's first-generation borehole geophone network. Prior to 2015, seismic monitoring of induced seismicity in the north of the Netherlands predominantly relied on this first-generation borehole network. In this report, the characteristics of the first-generation borehole network are detailed, their instrument responses are carefully evaluated, and the quality of the network's continuous recordings is assessed.

The reported instrument responses are validated by means of an exhaustive, quantitative evaluation of the specifications of the geophones and dataloggers. A seismic station's instrument response typically describes the conversion from physical units (e.g., particle velocity in meters per second) to digital units of information (e.g., counts). The instrument-responses reported in the meta-data are evaluated against the description of the actual instrumentation installed in the field. The reported instrument responses are found to deviate slightly from the reconstructed instrument responses. This deviation, however, merely results in amplitude and phase differences of less than a few percent. It is shown that, in terms of magnitude estimations and arrival-time picks, this deviation can be considered negligible.

A seismic station's meta-data also includes the orientation and dip of its channels. Based on both teleseismic and induced earthquake phases, the polarization of the reported dips and the orientations are checked. In addition, the orientation of the horizontal channels for three of the 18 borehole stations are estimated. The orientations of these three stations were not determined at the time of installation. We find that the meta-data needs to be updated for a number of stations. First, the polarization of both vertical and horizontal channels of a number of stations turn out to be flipped. Second, a polarity flip was induced while replacing the (old) acquisition setup with a new datalogger; for most stations this occurred around 2016. This update has been implemented.

The final objective that is met in this report pertains data quality. First, the presence of gaps in the recordings is investigated. In this respect, samples with coinciding time stamps are frequently observed up to 2016. That is, prior to the replacement of the dataloggers. This typically concerns a single sample, i.e., an overlap of one sample. Similarly, numerous gaps that have a length of a single sample are found in these recordings. A processing approach is proposed which allows a user to remove these data glitches, and which prevents the deconvolution underlying the removal of the instrument response to result in corrupt data. Second, corrupt data streams are identified. Three metrics are used to achieve this. These are (i) the (presumed) stability of a channels recording in terms of amplitude, (ii) the spectograms routinely computed as part of KNMI's suite of quality control tools, and (iii) the recordings of nearby induced events. This analysis results in a table listing for each station, geophone, and channel, which recordings (if any) has been removed from our archive. The cause of the data corruption is typically not investigated, but plenty abound. Examples include broken wires, a severe 50Hz grid distortion, badly connected cables, etc.

Based on the findings presented in this report, (i) the meta-data of the first-generation borehole stations has been updated (dips and orientations), and (ii) our waveform archive has been cleaned up. The cleanup involved the removal of the recordings listed in Table 4.9. Accounting for the aforementioned single-sample data glitches is left to the discretion of the data users, who can benefit from the proposed processing approach. Together, the meta-data updates and archive cleanup resulted in a high-quality data set, serving our own operations (and as such the general public) as well as research institutes and academic institutions working with our data.

Contents

1 Introduction **4**

1.1 Objectives 5

2 Network characteristics **7**

3 Instrument response **9**

3.1 Second epoch 10

3.2 Third epoch 12

3.3 On the shunt resistor and the associated damping 13

3.3.1 Consequences for the second epoch 13

3.3.2 Consequences for the third epoch 14

4 Data quality **16**

4.1 Data availability 16

4.2 Polarity and orientation 18

4.2.1 Polarity of the vertical components 20

4.2.2 Orientation of the horizontal components 29

4.3 Amplitudes 39

5 Conclusions **63**

Appendices: **67**

A A StationXML example **68**

B On the response of a shunted geophone **71**

B.1 General (spring-dashpot) description of an inertial seismometer 71

B.2 Poles and zeros 72

B.3 A modern geophone 73
B.4 response function for output voltage 74
B.5 The (potential) effect of the datalogger 74

C Daily data availability of channel HHE of geophone FSW5 **76**

1. Introduction

Induced seismicity in the north of the Netherlands is chiefly monitored by means of three-component borehole geophones. Typically, four geophones are installed at four different depth levels, with depths of 50, 100, 150, and 200 meters being most common. Such a string of borehole geophones is often also referred to as a 'vertical borehole array'. In the remainder of this report, however, we will refer to such a vertical borehole array as a 'borehole station' (or sometimes even simply 'station').

Most of KNMI's borehole stations were only installed in the last decade. Prior to 2015, seismic monitoring in the north of the Netherlands relied predominantly on a set of 18 first-generation borehole stations. In the period from 2010 to 2015, during which the gas-extraction-induced seismic energy release peaked (Hainzl et al., 2025), these 18 stations have been particularly instrumental. The map in Figure 1.1 depicts their locations while Table 1.1 provides their name and longitude & latitude.

This introduction gives the context of the quality analysis performed in this study. This quality analysis pertains only the continuous waveforms collected by the first-generation borehole stations. A detailed analysis of the "triggered" recordings by these 18 borehole stations can be found in Dost et al. (2023). Real-time continuous waveform collection started around 2010. In Section 2, we give a brief overview of the network of borehole stations whose data are quality checked. These data have been quality checked till the first of January 2024. The instrument responses are described in Section 3. The results of an

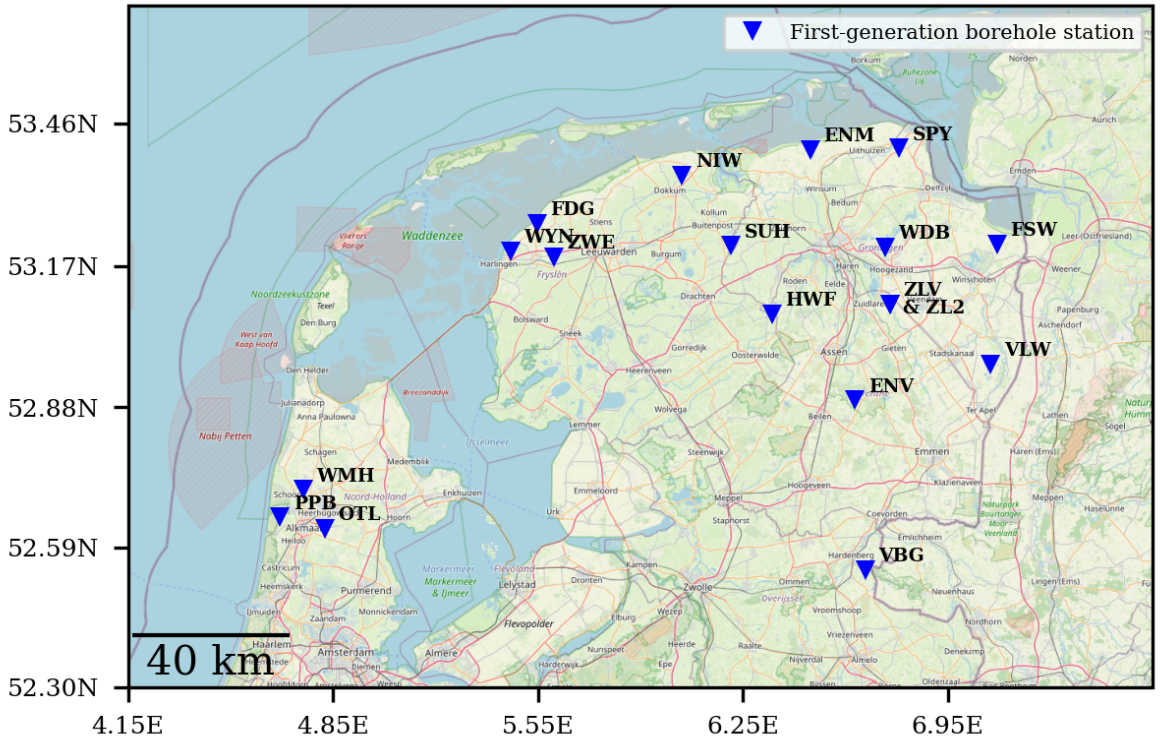

Figure 1.1: *KNMI's first-generation vertical borehole arrays (blue inverted triangles). Mind that ZLV and ZL2 are co-located.*

Table 1.1: *The 18 borehole stations whose continuous recordings have been quality checked in this report.*

Name	**Place name**	**Latitude**	**Longitude**
FSW	Finsterwolde	53.2135	7.1195
ENM	Eenrum (Westernieland)	53.4064	6.4817
WDB	Woudbloem	53.2083	6.7355
ZLV	Zuidlaarderveen 1	53.0921	6.7533
ZL2	Zuidlaarderveen 2	53.0921	6.7533
ENV	Elp (Enerveen)	52.8944	6.6337
VLW	Vlagtwedde	52.9682	7.0972
VBG	Venebrugge	52.5440	6.6693
HWF	Haulerwijk (Een)	53.0710	6.3512
OTL	Oterleek	52.6289	4.8227
PPB	Philisteinsche Polder	52.6526	4.6700
WMH	Warmenhuizen	52.7096	4.7498
NIW	Niawier (Wetzens)	53.3548	6.0430
SUH	Surhuizum	53.2113	6.2110
SPY	Spijk (Roodeschool)	53.4098	6.7838
FDG	Firdgum	53.2562	5.5481
ZWE	Zweins	53.1885	5.6045
WYN	Wijnaldum	53.1995	5.4578

exhaustive data quality analysis are presented in Section 4. This section consists of separate analyses of the data availability (Section 4.1), the polarity and orientations of the different channels (Section 4.2), and the overall quality and amplitudes of the recordings (Section 4.3). Finally, in Section 5 we draw conclusions.

1.1 Objectives

Consisting of sensors at multiple depth levels, vertical borehole arrays are inherently suitable for quality control tests. Important issues are component malfunctioning, instability of waveform amplitude measurements, reversed polarities and/or incorrect orientations of the horizontal channels.

The objective of this study is manifold. The first objective involves an evaluation of the *instrument responses*. These instrument responses are part of what is referred to as the *meta-data*. The meta-data includes station siting, channel orientations, and a (quantitative) description of the instrumentation. In the absence of meta-data, a station's recordings are difficult to interpret and utilize. Seismic meta-data is typically stored and exchanged using FDSN's *StationXML* format (International Federation of Digital Seismographs Networks (FDSN), 2022). KNMI's seismic data archive, however, is integrated in *SeisComP*'s architecture (Helmholtz-Centre Potsdam - GFZ German Research Centre for Geosciences and gempa GmbH, 2008). SeisComP has its own (slightly different) implementation of FDSN's StationXML standard. Conversion between a station's StationXML file and SeisComP's implementation of that standard is possible, but should be dealt with with care. In this report we adhere to FDSN's StationXML standard in our description of the meta-data.

The reported instrument responses describe the conversion from particle velocity in meters per second to counts. These responses are evaluated against the description of the instrumentation in Dost and Haak (2002) and Dost et al. (2023). The objective of this evaluation is to confirm the consistency between the actual instrumentation installed in the field on the one hand, and the reported instrument response on the other hand. This evaluation includes an explicit computation of the *response function* based on the electronic specifications provided by the geophone and datalogger manufacturers. This objective is addressed in Section 3.

A second objective is to identify reversed (vertical) polarities and incorrect orientations of the horizontal components, with the underlying goal being of course to correct these in the meta-data. The fidelity of

the vertical polarity reported in the meta-data is evaluated using teleseismic PKIKP and P phases (see Storchak et al., 2003, for details). The accuracy of the orientations reported in the meta-data is assessed using P-waves generated by nearby induced seismic events. Both analyses are described in detail in Section 4.2. The meta-data were updated accordingly.

A third objective is the identification of corrupt data streams. By meeting this objective we can remove corrupt data from our archive. This results in a high-quality data set, which serves our own operations (and as such the general public) as well as research institutes and academic institutions working with our data (e.g., Masfara & Weemstra, 2024; Hainzl et al., 2025). It fosters and expedites both earthquake nucleation studies and subsurface characterization studies in Groningen and surroundings. Furthermore, it brings down the yearly costs we bear to have our archive stored on Amazon Web Services. Identifying corrupt data streams is achieved through computation and inspection of spectograms, checking the stability of the amplitudes, and inspection of the seismograms of both teleseismic events and nearby induced events. It additionally includes the identification of sampling issues and timing issues. This objective is met in Section 4.3, with Table 4.9 summarizing our main findings.

2. Network characteristics

Of the 18 first-generation borehole stations, 11 were installed in spring 1995 and one in 1991 (Dost et al., 2023). The other six were installed around 2010. The advantage of borehole geophones is the relatively high signal-to-noise ratio (SNR) at depth, which significantly increases the detectability of (induced) earthquakes (Ruigrok & Dost, 2019). This conclusion was drawn based on the first prototype borehole array (FSW) which was installed near Finsterwolde in 1991, and which consisted of five three-component geophones with 75 m vertical spacing down to a depth of 300 m. This station was in fact specifically designed to analyze the noise reduction at depth. It was found that most of the noise reduction is achieved within the first 75 m, with a further smaller improvement at larger depths. Based on these results it was decided to limit the depth of future boreholes to a maximum of 200 m. The eleven additional borehole geophone arrays installed in 1995 therefore consisted of four three-component geophones with 50 m vertical spacing and had a total depth of 200 m.

Of the eleven geophone arrays installed in 1995, two geophone arrays (ZLV and ZL2) were installed in the same borehole in a staggered fashion. That is, similar to the other nine geophone arrays installed in 1995, the geophones of ZLV can be found at depths of 50, 100, 150, and 200 meters, whereas the geophones of ZL2 were installed at depths of 25, 75, 125 and 175 meters. Consequently, and in accordance with the fact that they bear different names, ZLV and ZL2 are considered separate stations in this report. Three of the eleven borehole arrays installed in 1995 were installed in a region around the city of Alkmaar, in the northwestern part of the Netherlands. This was because this region hosts a number of (small) gas fields. The seven remaining borehole stations (of the eleven installed in 1995) were installed in the northeast of the Netherlands (Figure 1.1) to monitor the Groningen gas field and a number of smaller surrounding gas fields.

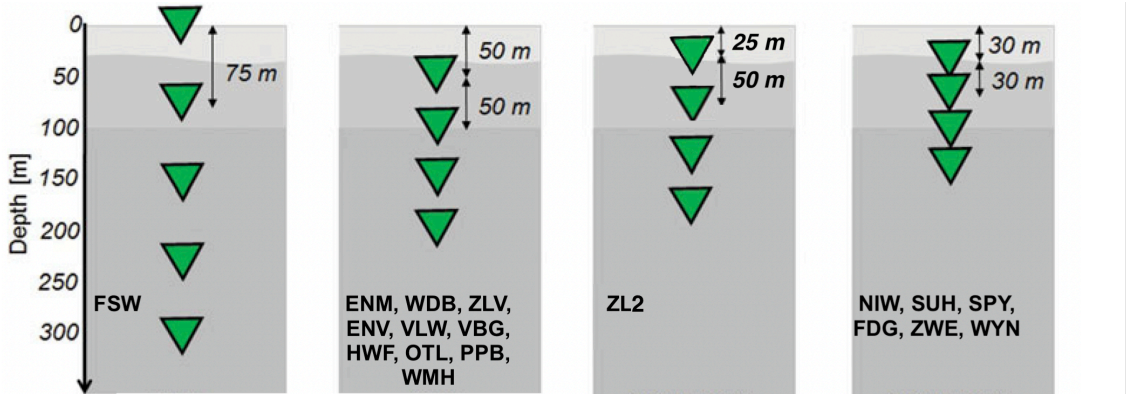

Figure 2.1: *Overview of the four different borehole configurations of the first-generation borehole geophone network in the northern Netherlands. Inverted green triangles denote depth levels of 4.5 Hz geophones. Station names for which the configuration applies are shown at the bottom. Details of individual stations are provided in Table 2.1. Figure adapted from Dost et al. (2017a).*

For the first 15 years, the 12 borehole stations installed in the nineties operated in an off-line, triggered mode. Starting in 2009, but mostly in 2010, data collection was gradually converted to a real-time operation. Approximately simultaneously with this transition to real-time waveform collection, the six additional borehole geophone arrays were installed. These geophone arrays were installed to (i) cover a larger region to the west of the Groningen gas field (NIW, SUH), (ii) to cover the north-eastern part of the Groningen gas field (SPY), and (iii) to monitor potential seismicity due to salt mining in the

Table 2.1: *Starting date for each of the borehole stations. This date refers to the date at which real-time (continuous) waveform collection started. The first 12 stations operated in a triggered mode for about 15 years prior to this date. Station ZL2 was discontinued on 2018-03-23.*

	Continuous since	Levels	Geophones	Depths
FSW	2010-04-29	5	FSW1, FSW2, FSW3, FSW4, FSW5	0, 75, 150, 225, 300
ENM	2010-01-22	4	ENM1, ENM2, ENM3, ENM4	50, 100, 150, 200
WDB	2010-04-29	4	WDB1, WDB2, WDB3, WDB4	47, 97, 147, 197
ZLV	2010-05-18	5	ZLV0, ZLV1, ZLV2, ZLV3, ZLV4	0, 50, 100, 150, 200
ZL2	2009-04-10	4	ZL21, ZL22, ZL23, ZL24	25, 75, 125, 175
ENV	2009-12-04	4	ENV1, ENV2, ENV3, ENV4	50, 100, 150, 200
VLW	2010-10-29	4	VLW1, VLW2, VLW3, VLW4	50, 100, 150, 200
VBG	2010-09-01	4	VBG1, VBG2, VBG3, VBG4	42, 92, 142, 192
HWF	2010-11-24	4	HWF1, HWF2, HWF3, HWF4	50, 100, 150, 200
OTL	2010-10-11	4	OTL1, OTL2, OTL3, OTL4	50, 100, 150, 200
PPB	2010-10-16	4	PPB1, PPB2, PPB3, PPB4	15, 90, 165, 240
WMH	2010-10-11	4	WMH1, WMH2, WMH3, WMH4	50, 100, 150, 200
NIW	2009-05-20	4	NIW1, NIW2, NIW3, NIW4	30, 60, 90, 120
SUH	2009-08-26	4	SUH1, SUH2, SUH3, SUH4	30, 60, 90, 120
SPY	2010-07-08	4	SPY1, SPY2, SPY3, SPY4	30, 60, 90, 120
FDG	2009-10-13	4	FDG1, FDG2, FDG3, FDG4	30, 60, 90, 120
ZWE	2010-03-24	4	ZWE1, ZWE2, ZWE3, ZWE4	30, 60, 90, 120
WYN	2010-03-03	4	WYN1, WYN2, WYN3, WYN4	30, 60, 90, 120

western part of the province of Friesland (FDG, ZWE and WYN). Station SPY was co-located with a LOFAR-node (Low Frequency Array for the Radio-astronomy; e.g., Drijkoningen, 2007). Due to the fact that, at that time, drilling costs could be reduced considerably if depth was limited to 120 m, these geophone arrays extend down to that depth only. Just as the older borehole arrays, these arrays consist of four three-component geophones (30 m vertical spacing between the sensors). The different types of configurations of the 18 first-generation vertical geophone arrays are shown in Figure 2.1. Table 2.1 lists for each station the start of continuous data collection, the number of geophones, the geophone codes, and their respective depths. Data collection by station ZL2 was discontinued at the beginning of 2018. All real-time data collected are directly accessible to users through the KNMI webpages and through a webservice (KNMI, 1993).

3. Instrument response

With the 'instrument response' of a borehole station we refer to the response of the entire system that converts the actual ground motion at a site expressed in m/s to a digital recording expressed in counts. We follow Dost et al. (2023) and distinguish between three epochs. The first epoch concerns the period during which the borehole stations operated in an off-line, triggered mode. The instrument responses during this period are exhaustively described in Dost et al. (2023) and is beyond the scope of this report. The second epoch runs from either the moment that triggered data collection was converted to a real-time operation (first 12 stations in Table 1.1) or from the moment the station was installed (last six stations in Table 1.1). Note that this implies that there does not exist first-epoch data for the latter stations. Station-specific dates for the start of the second epoch are given in column 2 of Table 2.1. The third epoch starts at the moment that a station's datalogger is replaced by a Kinemetrics datalogger, type Granite (see Table 3.1). This replacement was paired with a complete overhaul of the acquisition system (except for the geophones which are fixed in the subsurface) and hence implies a significant change of the instrument response. The start of the third epoch also coincides with an increase in sample rate from 100 to 200 Hz. An exception is station ZL2, which continued to sample the wavefield at 100 Hz during the third epoch. Because the Kinemetrics dataloggers allowed a maximum of 12 channels to be connected, stations FSW and ZLV had one of their (five) geophones left disconnected (FSW4 and ZLV0, respectively; see Table 3.1).

The first station that transitioned to the third epoch was ZL2 (2014-09-23; see Table 3.1). Importantly, ZL2's third epoch is preceded by a one-and-a-half month "epoch" (2014-08-14 – 2014-09-23) during which merely the datalogger was replaced by a Kinemetrics datalogger, whereas the rest of the original

Table 3.1: *Borehole stations whose datalogger has been replaced. The replacement date marks the start of the third epoch. Note that the datalogger of station was ZL2 was in reality replaced by a Kinemetrics datalogger on 2014-08-14; about one-and-half-month prior to the listed date. Since the rest of the original acquisition system was left in place at that point in time, however, the start of ZL2's third epoch is defined to be the moment that also all original analog filters were dismantled (2014-09-23). Station ZL2 was discontinued on 2018-03-23. The three stations in Western Friesland (FDG, ZWE, and WYN) did not have their datalogger replaced (prior to 01-01-2024), and are hence not listed here.*

	Datalogger replaced	Geophones	Depths
FSW	2016-06-14	FSW1, FSW2, FSW3, FSW5	0, 75, 150, 300
ENM	2016-05-04	ENM1, ENM2, ENM3, ENM4	50, 100, 150, 200
WDB	2016-06-14	WDB1, WDB2, WDB3, WDB4	47, 97, 147, 197
ZLV	2016-06-15	ZLV1, ZLV2, ZLV3, ZLV4	50, 100, 150, 200
ZL2	2014-09-23	ZL21, ZL22, ZL23, ZL24	25, 75, 125, 175
ENV	2016-06-16	ENV1, ENV2, ENV3, ENV4	50, 100, 150, 200
VLW	2016-06-15	VLW1, VLW2, VLW3, VLW4	50, 100, 150, 200
VBG	2016-06-16	VBG1, VBG2, VBG3, VBG4	42, 92, 142, 192
HWF	2016-06-13	HWF1, HWF2, HWF3, HWF4	50, 100, 150, 200
OTL	2019-07-02	OTL1, OTL2, OTL3, OTL4	50, 100, 150, 200
PPB	2019-07-02	PPB1, PPB2, PPB3, PPB4	15, 90, 165, 240
WMH	2019-07-02	WMH1, WMH2, WMH3, WMH4	50, 100, 150, 200
NIW	2018-02-15	NIW1, NIW2, NIW3, NIW4	30, 60, 90, 120
SUH	2016-06-13	SUH1, SUH2, SUH3, SUH4	30, 60, 90, 120
SPY	2016-06-14	SPY1, SPY2, SPY3, SPY4	30, 60, 90, 120

acquisition system was left in place. This is explained in more detail below. We have the impression that station ZL2, at that time, served as "test station" for the new acquisition setup. Data collection by this station was discontinued 2018-03-23.

Ten stations had the new acquisition system put in place in 2016. Of the other seven borehole stations, four stations had their datalogger replaced at a later time: Station NIW had its datalogger replaced in 2018 and stations OTL, PPB, and WMH simultaneously mid 2019. These last three are located around the city of Alkmaar, in the northwestern part of the Netherlands. Finally, the three remaining stations (FDG, ZWE, and WYN) never had their datalogger replaced and hence never made it into the third epoch. These stations stopped delivering data toward the end of the period considered in this report: FDG in 2021, ZWE in 2022, and WYN in 2023. These are the three stations that are located in the western part of the Province of Friesland (Figure 1.1).

Below, we describe first the instrument responses reported for the second and third epoch (Sections 3.1 and 3.2, respectively). To that end, we extract all relevant details from the reports by Dost and Haak (2002) and Dost et al. (2023), and confirm that the reported instrument responses match those in the StationXMLs. In Section 3.3, we subsequently account for the fact that the assumed damping of 0.707 does not coincide with the true damping. This is because of the fact that (i) the shunt resistance is slightly too low to achieve such damping and (ii) that the datalogger's resistance is too low to be neglected. We additionally describe the consequences of this inconsistency for the recorded waveforms. Fortunately, the deviation of the true response, in terms of both phase and amplitude, is in the order of only a few percent. This renders it unnecessary to update the StationXMLs of these stations.

3.1 Second epoch

In the period 1995-2010, the first twelve borehole stations in Table 1.1 operated in a triggered mode. In this period, these stations all used the same electronics and A/D converter. This includes the sensor, a 4.5 Hz SM-6 low frequency geophone (B coil), followed by a shaping filter to move the corner frequency to 1 Hz, a high-pass filter at 0.15 Hz to minimize low frequency noise and an anti-alias filter (8-order Butterworth) at 28 Hz. Replacement of the triggered systems with continuous-data-streaming systems in 2010 (station-specific dates given in column 2 of Table 2.1) did not alter the hardware setup (Dost et al., 2023). The A/D boards and PCs, however, were updated during replacement. In terms of instrument response, this update merely resulted in a reduction of the overall gain by a factor of 4. The update also resulted in a decrease of the sampling rate from 120 Hz to 100 Hz. For the epoch starting from 2010, until the moment the stations' dataloggers were replaced by Kinemetrics dataloggers (2016 for most stations; see Table 3.1), we benefit from the instrument response description in Dost et al. (2023).

The description of the instrument response in Dost et al. (2023) partly builds on the earlier description by Dost and Haak (2002). We therefore adhere to the conventions and symbols in these two reports. The description of the instrument response consists of two "stages". The first stage is described by a response function (or transfer function), $T(s)$, giving the complex, frequency-dependent ratio between the system's output in Volts (V), and the Earth's particle velocity in meters per second (m/s). The second stage merely involves the gain associated with the datalogger's response, which describes the ratio between the datalogger's input in Volts and its output in counts. These dataloggers (PC-LabCard PCL-816, Advantech Corp.) are 16 bit A/D converters, where a maximum of 65536 Counts (2^{16}) are used for maximum input difference of 20 Vpp (peak-to-peak Voltage). Consequently, the gain associated with the second stage evaluates to 65536/20=**3276.8** Counts/V.

The response of the system is typically written as a transfer function in the Laplace-domain. The parameter s is defined as $\sigma + j\omega$, where j is the imaginary unit, and σ and ω are both real; the latter can be shown to coincide with the angular frequency, i.e., $\omega \equiv 2\pi f$. The frequency response of the system is hence obtained by evaluating $T(s)$ on the imaginary axis of the s-plane, i.e., when $s = j\omega$ (International Federation of Digital Seismographs Networks (FDSN), 2022). The first stage's response function $T(s)$ is the product of (i) the SM-6's response function $T_{\mathrm{s}}(s)$, (ii) a correction filter $T_{\mathrm{corr}}(s)$ to move the corner frequency of the system from 4.5 to 1 Hz, (iii) a high-pass filter $T_{\mathrm{hp}}(s)$ (corner frequency 0.15 Hz) to suppress low-frequency noise, and (iv) the transfer function $T_{\mathrm{al}}(s)$ describing the low-pass 8th order

Butterworth filter (corner frequency 28 Hz). Details of the individual contributions are provided in Dost and Haak (2002). Multiplying these four contributions gives (Dost et al., 2023),

$$\begin{aligned} T(s) =& T_{\mathrm{s}} \cdot T_{\mathrm{corr}} \cdot T_{\mathrm{hp}} \cdot T_{\mathrm{al}} \\ =& \frac{s^2 S}{(s-s_1)\,(s-s_1^*)} \frac{(s-s_2)^2}{(s-s_3)^2} \frac{s^2}{(s-s_4)\,(s-s_4^*)} \prod_{k=3}^{6} \frac{\omega_3^2}{(s-s_{k+2})\,(s-s_{k+2}^*)}, \end{aligned} \tag{3.1}$$

where the * indicates complex conjugation. Both the angular corner frequency ω_3 and the first stage's sensitivity S are detailed further below. Note that T_{s} differs from the description in Dost and Haak (2002, eq. 3.1) by a factor s due to the fact that division by the response function above yields particle velocity (m/s), whereas division by the response function provided in Dost and Haak (2002) yields particle displacement (m).

Dost et al. (2023) carefully re-evaluated the electronic schemes associated with the different filters constituting the response function above, resulting in poles that slightly differ from the ones reported in Dost and Haak (2002). The obtained response function $T(s)$ has 4 zeros of (0.0, 0.0) and two zeros s_2 with a value of $(-28.4377, 0.0)$. There are 14 poles, which can be described by the following seven values (the other seven poles being their complex conjugates):

$$\begin{aligned} s_1 &= (-19.990, 19.996) \\ s_3 &= (-6.28931, 0.0) \\ s_4 &= (-0.666667, 0.700877) \\ s_5 &= (-34.3278, 173.108) \\ s_6 &= (-98.348, 145.623) \\ s_7 &= (-147.079, 96.3482) \\ s_8 &= (-174.203, 29.8213), \end{aligned}$$

where the numbers in between brackets are values in the complex plane, with the first value representing the real part and the second value the imaginary part (e.g., $\Re[s_1]$=19.990 and $\Im[s_1]$=19.996). Pole s_1 is associated with the geophone, s_3 with the shaping filter, s_4 with the high-pass filter and s_5-s_8 with the Butterworth filter. Note that the real part of s_1 is erroneously reported to be positive in Dost et al. (2023), but that it is correct in the StationXML's (see Appendix A for an example).

The normalization factor associated with the poles and zeros in $T(s)$, reported at 10 Hz, coincides with 7.9814e+17. This does not include the factors S and ω_3^8.

The poles and zeros reported above are marginally different from the poles and zeros reported in Dost and Haak (2002) due to the recalculation by Dost et al. (2023). This recalculation also resulted in a small change of the factor ω_3 associated with the Butterworth filter (initially coinciding with $2\pi \times 28$; Dost & Haak, 2002). Consequently, instead of $\omega_3^8 = (2\pi \times 28)^8$=9.17705e+17, it was evaluated to be 9.2871e+17 (at 10 Hz). Note that the stationXMLs of the 18 borehole stations were all updated based on the re-evaluation by Dost et al. (2023).

The factor S in equation (3.1) is the product of the sensor's sensitivity of 28.8 V/(m/s), a factor (8200/(8200+375))$\approx$ 0.956, due to the shunt resistor of 8200 Ohm and Coil resistance of 375 Ohm (see Appendix B for details), and an electronic amplification factor of 1023 (for details we refer to Dost and Haak (2002) and Dost et al. (2023)). Multiplication of these three factors gives S=28174 V/(m/s). The gain of the first stage therefore evaluates to (28174 × 9.2871e+17)/7.9814e+17 = **32783** V/(m/s). Up to some (intermediate) rounding errors, this coincides with the stationXML reported gain of 32786.02 V/(m/s).

Combining the first stage's gain with the second stage's gain gives an **overall gain** of 3276.8 Counts/V × 32783 V/(m/s)= **1.074234e+8** Counts/(m/s) at 10 Hz. This is indeed the sensitivity reported in the StationXML. The borehole stations' frequency-dependent instrument response during the second epoch is depicted in Figure 3.1 using solid blue lines.

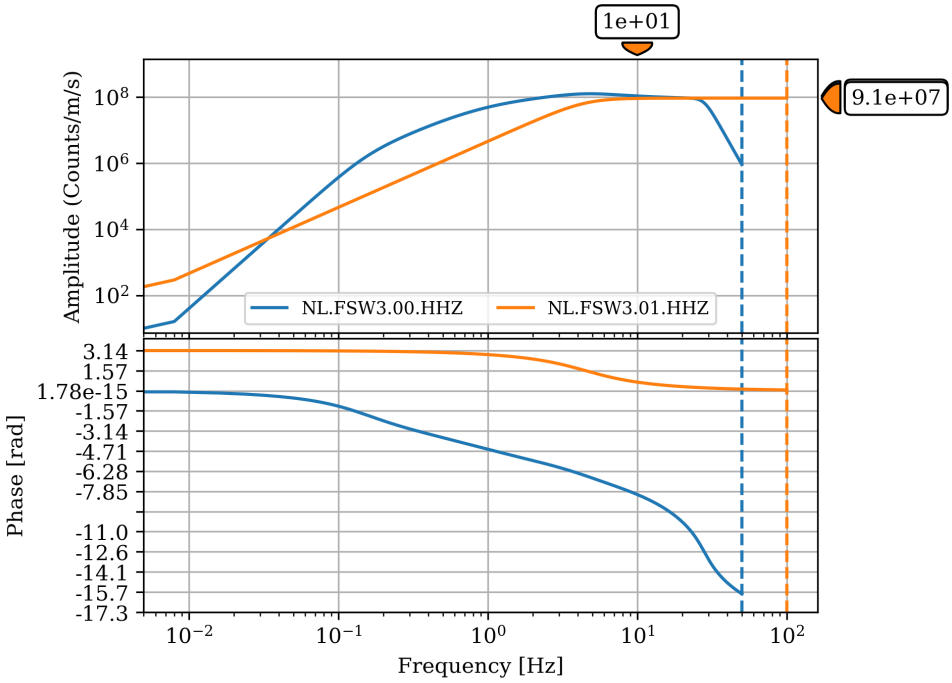

Figure 3.1: *Instrument response of channel HHZ of geophone FSW3 during the second (solid blue curve) and third (solid orange curve) epoch. These instrument responses are representative for (all channels of all geophones of) all borehole stations during these two epochs. The vertical dashed lines indicate the Nyquist frequency of 50 and 100 Hz during the second and third epoch, respectively.*

3.2 Third epoch

As we mentioned above, 15 of the 18 stations had their datalogger replaced by a Kinemetrics datalogger (see column 2 of Table 3.1 for station-specific dates). This replacement marks the start of the third epoch and an increase in sample rate from 100 Hz to 200 Hz. Simultaneously with this replacement, the electronics were simplified by removal of the analog high-pass, shaping, and anti-alias filters (Dost et al., 2023). Consequently, the instrument response also simplified considerably at this point. Recall that the start of ZL2's third epoch is preceded by a one-and-a-half month period during which merely the datalogger was replaced by a Kinemetrics datalogger, but during which the original analog filters were left in place. And although a separate epoch is defined in the StationXMLs of ZL2's geophones for this period, it should be understood that in this report the epoch starting at 2014-09-23 is referred to as the ZL2's third epoch. In addition, this station continued to sample the wavefield at 100 Hz during the third epoch.

Just as for the second epoch, the description of the instrument response consists of two stages. The response function describing the first stage is considerably simpler than that of the second epoch's first stage. This is due to the absence of the analog high-pass, shaping, and anti-alias filters. Specifically, the correction filter's transfer function $T_{\text{corr}}(s)$, the high-pass filter's transfer function $T_{\text{hp}}(s)$, and the the low-pass, 8th order Butterworth filter's transfer function $T_{\text{al}}(s)$ are all absent. The response function for this stage therefore reads (Aki & Richards, 2002),

$$T(s) = S\frac{-s^2}{(s-s_1)\,(s-s_1^*)}, \tag{3.2}$$

This response function has only two zeros of (0.0, 0.0), and two poles (s_1 and it's complex conjugate; see above). The normalization factor associated with these poles and zeros (at 10 Hz, and without the factor S), coincides with 1.02024. In this case, S is merely the sensor's sensitivity of 28.8 V/(m/s) multiplied by the correction resulting from the shunt resistor, i.e., 8200/(8200+375). Consequently, the gain of the first stage indeed evaluates to the reported gain (at 10 Hz) of 28.8 × 8200/(8200+375)/1.02024 ≈ **26.9893** V/(m/s) (a StationXML-implementation is provided Appendix A).

The second stage describes the digitization of the analog (voltage) signal. The Kinemetrics dataloggers are of the type Granite, which have a 127-dB dynamic range defining the smallest possible increment in motion that can be represented between clip levels and typical self-noise. Recording at a sampling rate of 200 Hz, the Granite provides a flat frequency response between DC (0 Hz) and 80 Hz, after which a strong anti-alias filter diminishes the signal amplitude to avoid signal aliasing. The Granite's 24 bit AD converter is used to cover a range of 5 Vpp (peak-to-peak Voltage), which implies a gain of 3355440 Counts/V. This is the gain reported as the second stage's gain in the StationXMLs. We finally note that the StationXML typically also contains an overall *InstrumentSensitivity*, which is obtained by multiplying the individual *StageGains*. Here, the InstrumentSensitivity hence evaluates to $26.9893 \times 3355440 = 90,561,076$ counts/(m/s).

It is important to note that the low-pass anti-alias filters are not included in the StationXMLs. Their absence implies that end-users who would like to exploit the signal above 80 Hz should implement the removal of the anti-alias filter themselves. This can be achieved based on the description in the user guide of the Granites (Kinemetrics, 2023). Since almost all seismological studies focus on signal below 80 Hz, however, this will typically not be needed.

3.3 On the shunt resistor and the associated damping

Dost and Haak (2002) state that "according to the specifications a shunt resistance of 8200 Ohm is needed to give a damping of 0.707". These authors therefore assume this amount of damping while computing the poles and zeros of the geophone-shunt resistor system. The values reported for s_1 and its complex conjugate s_1^* are hence contingent on the validity of this assumption. Given the specifications of the SM-6 low frequency geophone (B-coil), however, a slightly different shunt resistance is needed to give a damping of 0.707. In other words, the used shunt resistance of 8200 Ohm results in a slightly different damping and hence different poles s_1 and s_1^* and a different gain. This implies that the values reported in the StationXMLs (and which are described above in Sections 3.1 and 3.2) do not allow the true particle velocity to be recovered. In addition, the Granite dataloggers, whose installation marks the start of the third epoch, also affect the instrument response. This effect was not accounted for while computing the poles and zeros and the gain for this epoch. As we will show in the following sections, the difference between the reported instrument response and the correct instrument response is, for both epochs, in the order of a few percent.

3.3.1 Consequences for the second epoch

In Appendix B we describe in detail how the instrument response of a geophone equipped with a shunt resistance can be computed. Let us use this description to first compute the (correct) poles and gain for the second epoch. Considering that the used shunt resistance is 8200 Ohm, and that according to the geophone's specifications, its sensitivity G is 28.8 V/m/s, the resistance R_c of its coil is 375 Ohm, the inductance L_c of its coil is 0 Henry, its eigenfrequency (or natural frequency) f_0 is 4.5 Hz, its (moving) mass m is 11.1 gram, and its open circuit damping is 0.56, the true damping (h) of the shunted geophone becomes 0.714 instead of the 0.707 that was assumed (and which is considered ideal; Telford et al., 1990). Consequently, the poles s_1 and s_1^* do not coincide with $-19.990 + j19.996$ and $-19.990 - j19.996$, respectively, but instead evaluate to $-20.191 + j19.793$ and $-20.191 - j19.793$, respectively. In Figure 3.2 we show the amplitude and phase associated with the poles and gain reported in the StationXML (solid blue line) and the amplitude and phase associated with correct poles and gain (solid green line). The two curves are indistinguishable, and the relative amplitude difference does not exceed 1 % (bottom graph). The phase difference is not shown, but is negligible.

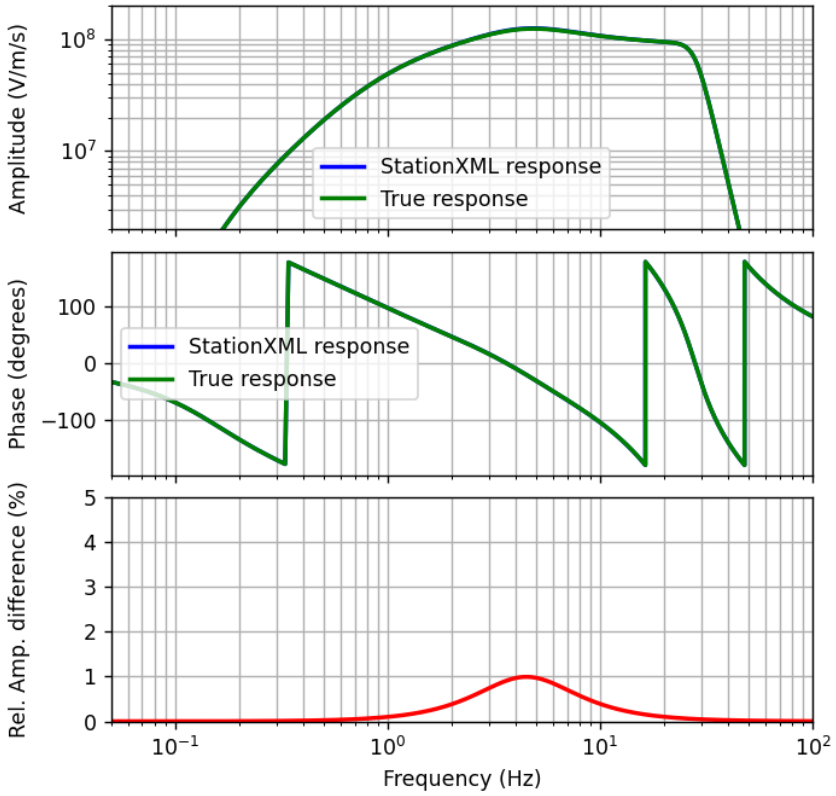

Figure 3.2: *Amplitude (top graph) and phase (center graph) associated with the poles and gain reported in the StationXML (solid blue curve) and the correct poles and gain (solid green curves) during the second epoch. Due to a strong overlap, the blue curves cannot be seen. The solid blue curves coincide with the solid blue curves in Figure 3.1. The bottom graph depicts the relative difference in amplitude between the reported (StationXML) response and the correct response.*

3.3.2 Consequences for the third epoch

Let us now compute the (correct) poles and gain for the third epoch. Of course, the geophones's specifications did not change between these two epochs. However, the installation of new dataloggers (Granites from Kinemetrics) does have some effect on the instrument responses due to fact that their resistance is not sufficiently high to ignore. The effect of the datalogger on the system's sensitivity can be ignored if its resistance is several orders of magnitude higher than that of the shunt. The input resistance of the Granite dataloggers is 102.4 kOhm. In addition, a breakout board is mounted on top of the dataloggers, which also effectuates a resistance of 118.0 kOhm. These two values were verified by means of a test with a multimeter. Together, this gives a resistance of 220.4 kOhm. The datalogger (with the breakout board) forms a parallel circuit with the shunt resistor.

Using the same specifications for the geophone as during the second epoch, the aforementioned datalogger resistance (including breakout board) implies that the true damping (h) of the shunted geophone becomes 0.720 instead of the 0.707 that was assumed (for details of the underlying theory and computations we again refer to Appendix B). Consequently, the poles s_1 and s_1^* do not coincide with $-19.990 + j19.996$ and $-19.990 - j19.996$, respectively, but instead evaluate to $-20.346 + j19.634$ and $-20.346 - j19.634$, respectively. In Figure 3.3 we show the amplitude and phase associated with the poles and gain reported in the StationXML (solid orange line) and the amplitude and phase associated with correct poles and gain (solid green line). The relative amplitude difference peaks at the geophone's eigenfrequency of 4.5 Hz, and does not exceed 2 % (third graph). The phase error pivots around 4.5 Hz, and does not exceed 0.5 degree (bottom graph). Note that for a sinusoid with a frequency of 8 Hz, a 0.5 degree phase difference translates to an " error" of $(0.5/360)\times(1/8)$=1.74e-4 s. This is negligible compared to a typical P-wave traveltime uncertainty of 0.137 s (Spetzler et al., 2024).

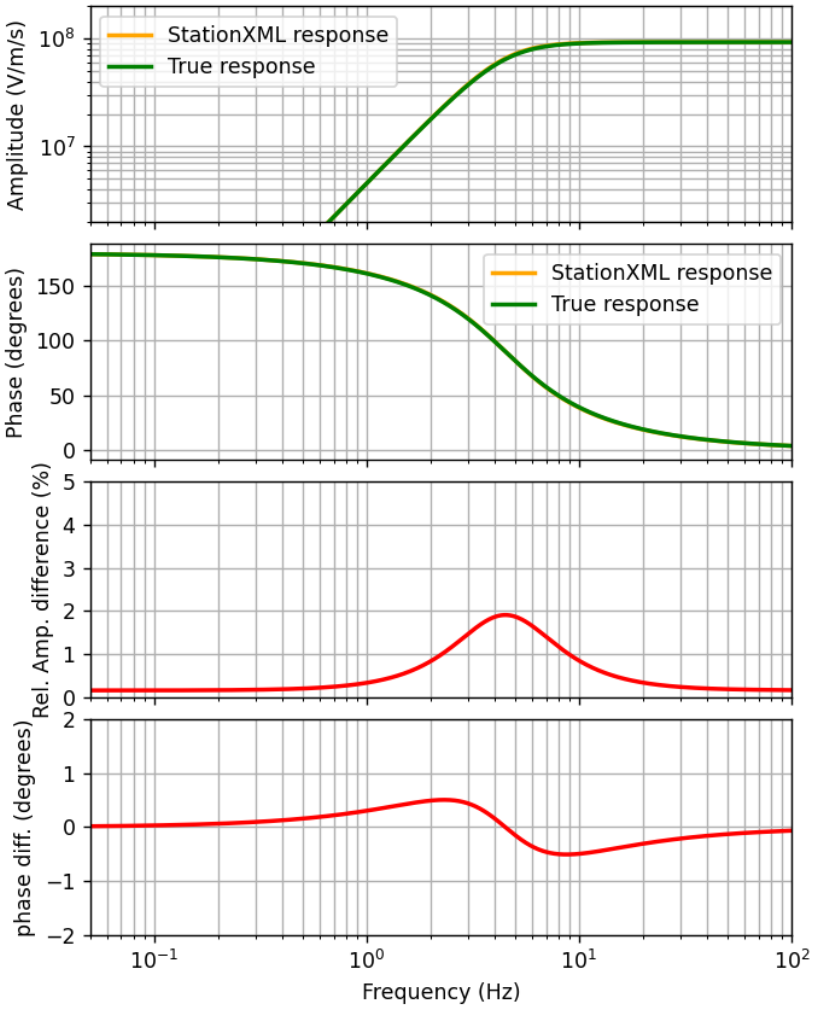

Figure 3.3: *Amplitude (top graph) and phase (second graph) associated with the poles and gain reported in the StationXML (solid orange curve) and the correct poles and gain (solid green curves) during the third epoch. The solid orange curves are identical to the solid orange curves in Figure 3.1. The two bottom graph depict (i) the relative difference in amplitude between the reported (StationXML) response and the correct response and (ii) the phase difference (in degrees) between the two responses.*

4. Data quality

In this section, we present the results of a comprehensive data quality analysis. This analysis has been performed for the continuous recordings of all 18 borehole stations (see Tables 1.1 and 2.1). We separately discuss data availability (Section 4.1), polarity and orientation (Section 4.2), and the amplitude and spectral content of the recordings (Section 4.3).

4.1 Data availability

Visualizing data availability is not straightforward for a total of 70 three-component geophones continuously sampling the wavefield for more than ten years. Fortunately, ORFEUS (Observatories & Research Facilities for European Seismology) offers numerous data services on their website. One of these services involves the ability to visualize daily *data availability*, which is part of the European Integrated Data Archive (EIDA). The central node of EIDA (the ODC or 'Orfeus Data Center' node) is hosted at the KNMI. This EIDA node archives and distributes the continuous recordings by the 18 vertical borehole arrays whose data is investigated in this report. Data availability can be checked on the following webpage. In Appendix C, we provide an example of the visualization of daily data availability (for borehole station FSW). The daily data availability of channel HHE of the lowest geophone of the other borehole arrays can be found in the repository accompanying this report (Weemstra & Ruigrok, 2026). We only generated overviews for channel HHE of the lowest geophone of each vertical array. The data availability of the other two channels appears to coincide with HHE. We performed a brief check, and the data availability (of all channels) of the other geophones of the same borehole array in fact also largely coincides with the data availability of the lowest sensor. This is not surprising given that all borehole sensors of a station were hooked up to the same datalogger.

```
21 Trace(s) in Stream:
NL.PPB3.00.HHZ | 2011-09-03T23:59:59.999999Z - 2011-09-04T00:53:32.859999Z | 100.0 Hz, 321287 samples
NL.PPB3.00.HHZ | 2011-09-04T00:53:32.849999Z - 2011-09-04T00:54:00.529999Z | 100.0 Hz, 2769 samples
NL.PPB3.00.HHZ | 2011-09-04T00:54:00.549999Z - 2011-09-04T03:19:33.999999Z | 100.0 Hz, 873346 samples
NL.PPB3.00.HHZ | 2011-09-04T03:19:33.989998Z - 2011-09-04T03:20:01.179998Z | 100.0 Hz, 2720 samples
NL.PPB3.00.HHZ | 2011-09-04T03:20:01.199999Z - 2011-09-04T05:44:50.159999Z | 100.0 Hz, 868897 samples
NL.PPB3.00.HHZ | 2011-09-04T05:44:50.149999Z - 2011-09-04T05:45:03.869999Z | 100.0 Hz, 1373 samples
NL.PPB3.00.HHZ | 2011-09-04T05:45:03.889999Z - 2011-09-04T08:05:46.779999Z | 100.0 Hz, 844290 samples
NL.PPB3.00.HHZ | 2011-09-04T08:05:46.769999Z - 2011-09-04T08:06:06.179999Z | 100.0 Hz, 1942 samples
NL.PPB3.00.HHZ | 2011-09-04T08:06:06.199999Z - 2011-09-04T10:22:44.529999Z | 100.0 Hz, 819834 samples
NL.PPB3.00.HHZ | 2011-09-04T10:22:44.519999Z - 2011-09-04T10:23:03.889999Z | 100.0 Hz, 1938 samples
NL.PPB3.00.HHZ | 2011-09-04T10:23:03.909999Z - 2011-09-04T12:40:48.079999Z | 100.0 Hz, 826418 samples
NL.PPB3.00.HHZ | 2011-09-04T12:40:48.069999Z - 2011-09-04T12:41:01.409999Z | 100.0 Hz, 1335 samples
NL.PPB3.00.HHZ | 2011-09-04T12:41:01.429999Z - 2011-09-04T15:00:48.429999Z | 100.0 Hz, 838701 samples
NL.PPB3.00.HHZ | 2011-09-04T15:00:48.419999Z - 2011-09-04T15:01:01.199999Z | 100.0 Hz, 1279 samples
NL.PPB3.00.HHZ | 2011-09-04T15:01:01.219999Z - 2011-09-04T17:21:38.619999Z | 100.0 Hz, 843741 samples
NL.PPB3.00.HHZ | 2011-09-04T17:21:38.609999Z - 2011-09-04T17:22:04.399999Z | 100.0 Hz, 2580 samples
NL.PPB3.00.HHZ | 2011-09-04T17:22:04.419999Z - 2011-09-04T19:42:35.669999Z | 100.0 Hz, 843126 samples
NL.PPB3.00.HHZ | 2011-09-04T19:42:35.659999Z - 2011-09-04T19:43:02.939999Z | 100.0 Hz, 2729 samples
NL.PPB3.00.HHZ | 2011-09-04T19:43:02.959999Z - 2011-09-04T22:03:18.649999Z | 100.0 Hz, 841570 samples
NL.PPB3.00.HHZ | 2011-09-04T22:03:18.639999Z - 2011-09-04T22:04:06.239999Z | 100.0 Hz, 4761 samples
NL.PPB3.00.HHZ | 2011-09-04T22:04:06.259999Z - 2011-09-04T23:59:59.999999Z | 100.0 Hz, 695375 samples
```

Figure 4.1: *Example of separate segments in a 24-hours, vertical component recording by geophone PPB3 (each line represents a separate segment). Start- and end-times of individual segments are marked by either an overlap of one or two samples, or a gap of one or two samples.*

The transition from the first to the second epoch is marked by the replacement of the triggered systems

with a continuous data streaming system. Station-specific dates for the start of the second epoch are given in Column 2 of Table 2.1). This transition did not alter the hardware setup, but did involve an update of the A/D boards and PCs (Dost et al., 2023). Contrary to the Kinemetric dataloggers active during the third epoch, the timing of the recordings during the second epoch is therefore based on communication between a separate GPS receiver and the A/D board. This results in the timing of the continuous recordings being slightly unstable for some stations. For these stations, this instability manifests itself as a series of overlapping and absent samples at specific, seemingly random times. An example of this can be seen in Figure 4.1. The overlapping spells and the gaps usually only involve one or two samples. These samples appear to still have the correct time stamp and as such the overlap and absence of samples did not lead to timing errors.

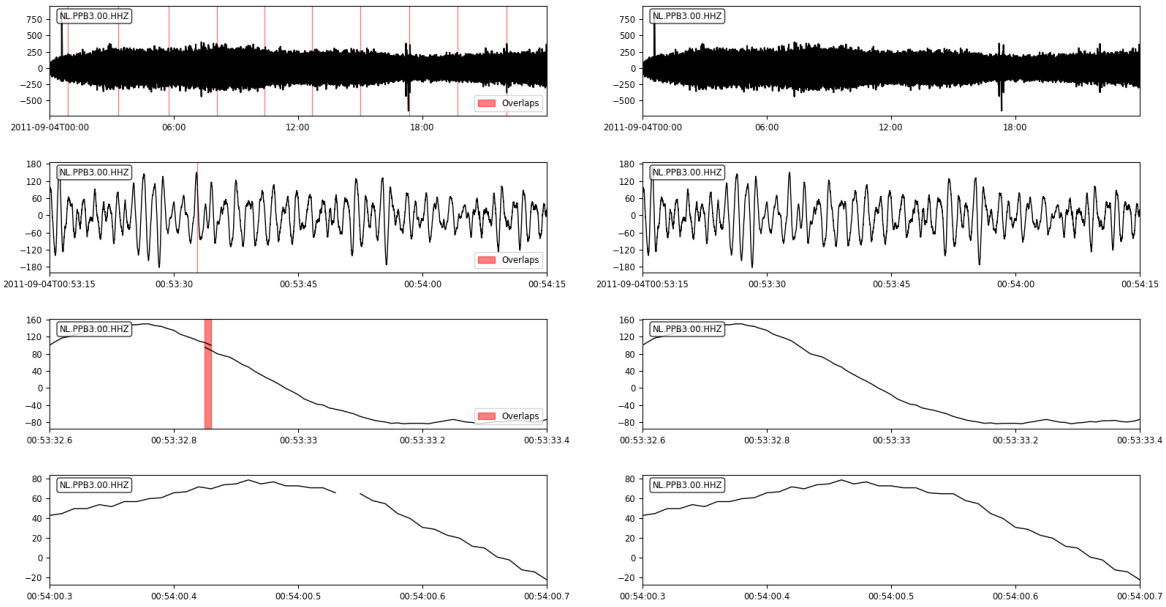

Figure 4.2: *Example of segmentation in the raw data (prior to removal of the instrument response). First row: One-day recording by the vertical channel of geophone PPB3 prior to (left) and after (right) merging overlapping samples and filling gaps (see also Figure 4.1). Second row: One-minute recording by that same vertical channel prior to (left) and after (right) merging overlapping samples and filling gaps. Third row: 0.8 second recording by that same vertical channel prior to (left) and after (right) merging overlapping samples. Fourth row: 0.6 second recording by that same vertical channel prior to (left) and after (right) filling a gap.*

Despite the fact that few overlapping or absent samples have no adverse effects on time-critical studies, one has to take care while processing such recordings. Specifically, the presence of gaps and discontinuities in the data leads to artefacts after removal of the instrument response; the latter being, in principle, a standard and routine operation in seismic data processing. In Figures 4.2 and 4.3, we exemplify this using vertical-component recordings by geophone PPB3. In Figure 4.2, we compare the raw data (vertical axis has units 'counts') prior to (left column) and after (right column) merging overlapping samples and filling gaps. In this case, this was implemented using Obspy's merge (https://docs.obspy.org/packages/autogen/obspy.core.stream.Stream.merge.html), with the *method* set to '1', *interpolation_samples* to '-1', and *fill_value* to 'interpolate'. The difference between the left and right column is minimal in the sense that, apart from the removal of overlapping samples and gaps, the traces coincide. In Figure 4.3, we compare these same traces after the instrument response has been removed. Note that the units along the vertical axes are meters per second in this figure. Clearly, the removal of the instrument response from the recording that contains overlapping samples and gaps gives rise to undesirable artifacts (left column), whereas removal of the instrument response after the overlapping samples and gaps have been merged and filled does not give rise to such artifacts. We therefore recommend researchers that would like to exploit the continuous recordings by our first-generation borehole network to apply this (or a similar) merge procedure prior to removal of the instrument response.

The continuous recording's segmentation described in this section is not observed to the same degree on

each borehole station. A quick check taught us that stations ENM, SPY, WYN and ZWE appear to be the most affected stations.

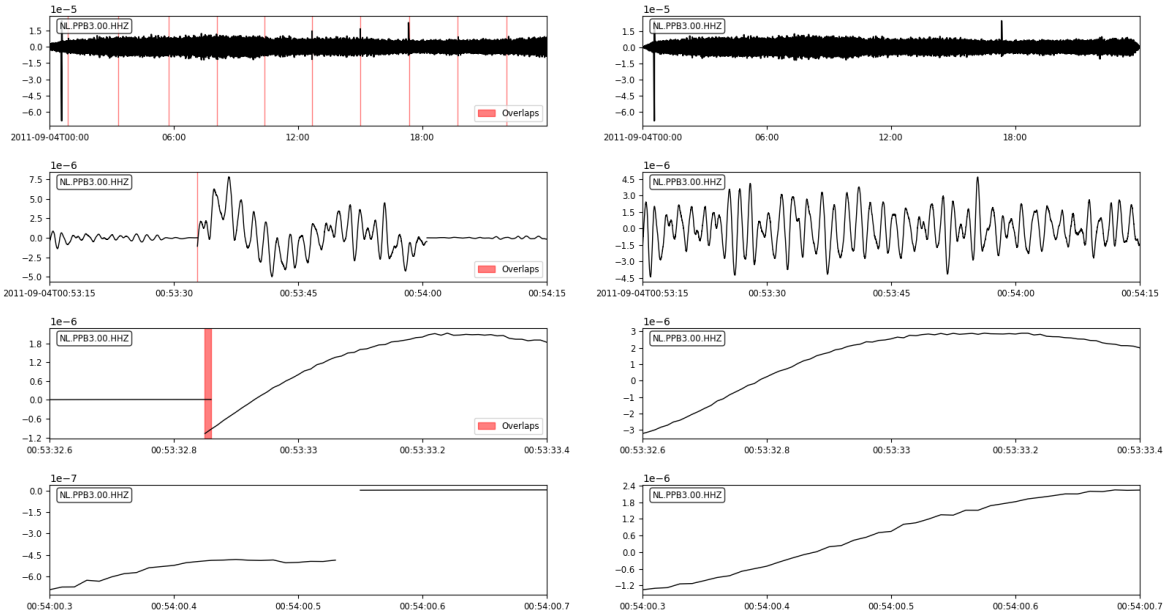

Figure 4.3: *Example of segmentation after removal of the instrument response. Essentially, these are the traces shown in Figure 4.2, but after removal of the instrument response. First row: One-day recording by the vertical channel of geophone PPB3 prior to (left) and after (right) merging overlapping samples and filling gaps. Second row: One-minute recording by that same vertical channel prior to (left) and after (right) merging overlapping samples and filling gaps. Third row: 0.8 second recording by that same vertical channel prior to (left) and after (right) merging overlapping samples. Fourth row: 0.6 second recording by that same vertical channel prior to (left) and after (right) filling a gap.*

4.2 Polarity and orientation

In this section, we separately evaluate (i) the polarity of the vertical component recordings and (ii) the orientation of the horizontal components. In the left column of Figure 4.4, the typical configuration of a KNMI borehole array is displayed. It shows how the three-component SM-6 geophones are installed in the borehole. It is safe to assume that the vertical orientation of one of the three components is retained. This is positive down, and indicated by a 'Z' (channel code HHZ). The orientation of the horizontal components is a priori unknown due to rotation of the borehole cable while lowering it in the borehole. The orientation of these components is usually determined afterwards using multiple *check shots* (Ruigrok et al., 2019; Dost et al., 2023). The set-up in the left column of Figure 4.4 pertains to the first-generation borehole network described in this report (albeit with different depth levels for FSW, ZL2, NIW, SUH, SPY, FDG, ZWE, and WYN; see Figure 2.1), the second-generation borehole network in Groningen (usually referred to as the G-network; see, e.g., Dost et al. (2017b) and Ntinalexis et al. (2019)), and many of our smaller regional networks (e.g., in Drenthe, Twente, and South-Holland; Ruigrok et al., 2023).

At the time of installation of the first-generation borehole network, the FDSN standards were unfortunately not adhered to (see FDSN, 2020). That is, instead of using '1' and '2' to indicate the orientation of the horizontal components in the StationXMLs (i.e., channel codes HH1 and HH2), 'N' and 'E' were used (i.e., channel codes HHN and HHE; with HHE being oriented 90 degrees clockwise from HHN). Furthermore, the vertical polarity was reversed in the electronics (Dost et al., 2023). The resulting StationXML coordinate system is shown, for each depth level, in the center of Figure 4.4. The use of the HHN and HHE codes of course suggest the orientations of the two horizontal channels to be North and East, even though that is not the case. To avoid confusion and for the sake of temporal consistency, however, it was decided to stick to channel codes HHN and HHE for the two horizontal components

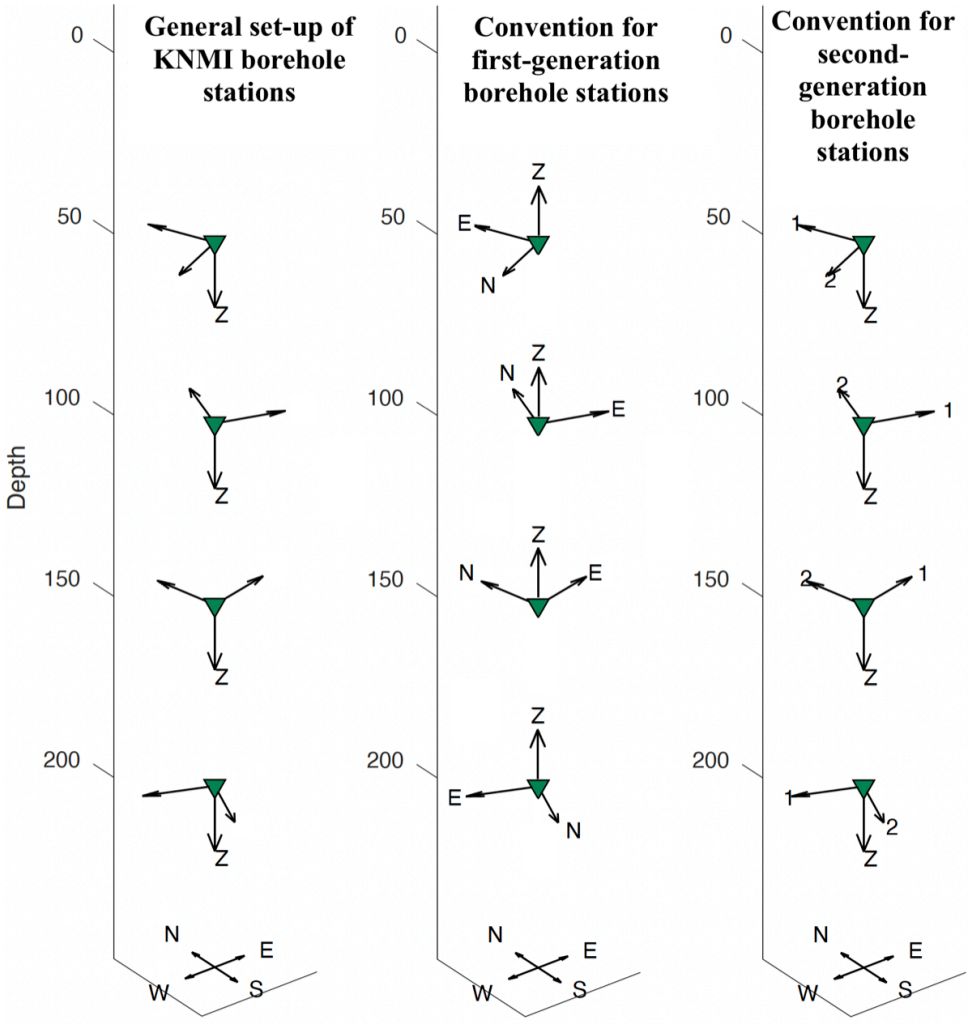

Figure 4.4: *Convention used for the polarity and associated orientation characters of the channel codes of KNMI's borehole network (this the third letter of the channel code, which is referred to as the subsource character by the FDSN; FDSN, 2020). Geophones are installed in the borehole with the vertical (Z) component being positive down (left). For the first-generation borehole stations this vertical polarity was reversed in the electronics (Dost et al., 2023). Furthermore, the horizontal channels are labeled HHN and HHE in the StationXMLs (center), despite these two channels not necessarily being oriented towards the North and East. For the second-generation borehole network (G-stations and our smaller, regional borehole networks), the positive down vertical polarity is retained and the horizontal channels are labeled HH2 and HH1, with HH1 being positive in a direction 90 degrees clockwise from HH2 (right).*

(Dost et al., 2023). In this report, we comply with this. For most components, the orientation of the channel has been estimated and listed in the StationXML. If an estimate is known, it is listed under *azimuth* as an orientation deviating from 0 or 90°.

4.2.1 Polarity of the vertical components

In the description of the FDSN's StationXML format (International Federation of Digital Seismographs Networks (FDSN), 2022), the polarity of a seismic sensor's vertical component is defined as positive down from the horizontal. Therefore, if a sensor has a positive movement downwards the dip is 90 degrees, whereas for a sensor that has a positive movement upwards, the dip is -90 degrees. The installation set-up of a KNMI borehole array (Figure 4.4; left) has a vertical component polarity that is positive down, which suggests the dip of each of the geophone's vertical components to have a value of 90 degrees. Confusingly, however, the positive down polarity of the geophones was reversed by means of the electronic components effectuating the different filters (see Section 3.1 of Dost et al., 2023, for a detailed description of these filters). In other words, a flip of the polarity was induced electronically. Consequently, the StationXMLs of the geophones report a dip of -90 degrees and the recording's motion is positive upwards.

Using teleseismic events, we compare the polarity from the vertical channels of the borehole geophones with that of the vertical channels of a number of selected broadband stations in- and outside the region. These broadband stations are WIT, HGN, WTSB, G81B and G82B. These broadband stations have a validated polarity that is positive upwards (dip of -90 degrees). (details of these stations can be retrieved on http://rdsa.knmi.nl/fdsnws/station/1/builder). In order to reliably compare the geophone recordings with the recordings by the broadband stations, we corrected the recordings for the instrument response. Since the vertical component recordings of both the broadband stations and the borehole geophones have a dip of -90, we expect the teleseismic arrivals to look very similar on both types of instruments (after instrument response removal). We compare the vertical component recordings of these geophones to the vertical component broadband recordings for each depth level separately (see Table 2.1). We then later validate these results by separately comparing the vertical-component polarity between different geophones (i.e., different depth levels) of the same borehole array. We adopt a systematic approach, which we will now describe in detail.

The first step of our procedure involves generating a catalog containing all earthquakes that fulfill either a set of conditions that favours the retrieval of direct P phases, or a set of conditions that favours the retrieval of PKIKP-phases (see Storchak et al., 2003, for a detailed description of these phases). The first set consists of all events whose epicentral distance is between 45 and 90 degrees (measured from broadband station WIT, which is located in the north of the Netherlands; see Figure 4.6), whose magnitude exceeds 7.8, and which occurred at a depth greater than 10 km and less than 500 km. The second set contains all events whose epicentral distance exceeds 140 degrees, whose magnitude exceeds 7.0, and which occurred at a depth greater than 100 km. These parameters were determined based on a preliminary assessment of the signal-to-noise ratio (SNR) of the desired phases. Both sets are then merged and sorted chronologically, after which the first event (as a function of time) in each half-year period is selected; the other events are discarded. Unfortunately, not every half-year period contains an event that fulfills one of the two sets of conditions. This implies that occasionally there are periods of (even) more than one year during which we cannot check the vertical polarity of the borehole geophones. Our findings (presented further below), however, show that this has no major implications.

The second step of our procedure involves the retrieval and processing of the events' waveforms. To that end, the approximate time of arrival and ray parameter of each phase is calculated using the TauP toolkit (Crotwell et al., 1999) assuming the IASP91 Earth model (Kennett & Engdahl, 1991). Again, the location of broadband station WIT is used as reference location. We subsequently retrieve one minute of vertical component recordings of both the selected broadband stations and the borehole stations. This one-minute time window starts 15 seconds prior to the computed arrival time. The signal is then deconvolved with the instrument response of the station, which implies a conversion from raw data in (digital) counts to vertical particle velocity in m/s. After detrending and tapering the data, we finally apply a second order zero-phase band-pass filter which retains signal between 0.05 and 0.4 Hz. Figure 4.5 exemplifies the band-pass filtered vertical component recordings by geophones at depth level 2 for a single teleseismic event. In this case, the recordings of a PKIKP phase due to a magnitude 7.0 event close to New Caledonia. We conclude from Figure 4.5 that geophones NIW2, SUH2, and FDG2, exhibit a flipped polarity of the vertical component (on the third of September, 2011).

The repository accompanying this report (Weemstra & Ruigrok, 2026) contains figures similar to Figure 4.5. That is, for each selected teleseismic phase (either P or PKIKP) the results of the just described

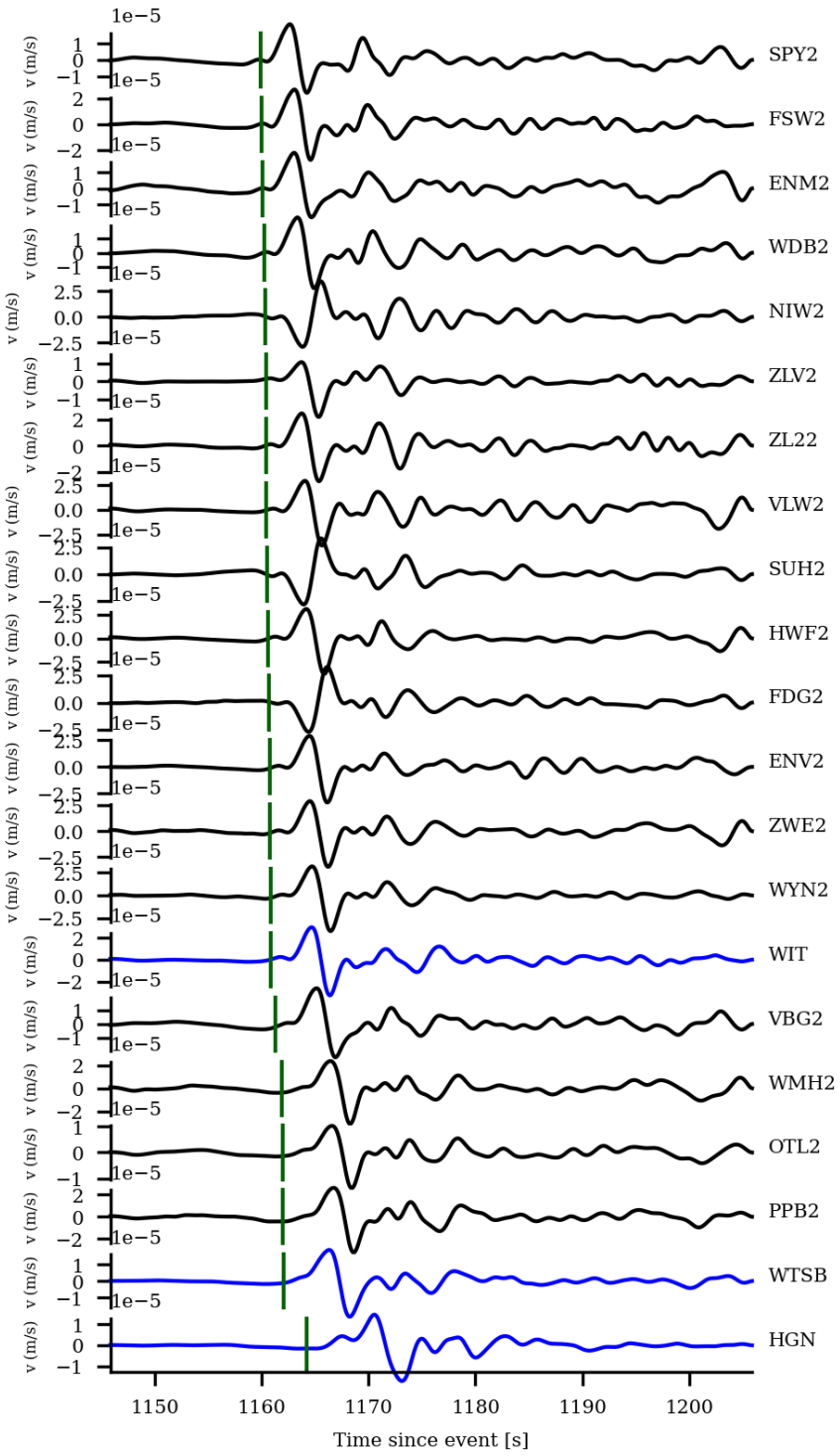

Figure 4.5: *The borehole network's recordings (second depth level) of a PKIKP phase of a magnitude 7.0 event close to New Caledonia (solid black traces). Recordings by broadband stations are depicted as solid blue traces. The time window for which waveform data is retrieved coincides for all instruments, and is based on the (computed) arrival time at broadband station WIT. Estimated arrival times for the individual instruments, which are computed using the TauP toolkit (Crotwell et al., 1999) applied to the IASP91 Earth model (Kennett & Engdahl, 1991), are depicted by means of vertical solid green lines. The one-minute long recordings are sorted and plotted based on these travel times.*

analysis are presented. Specifically, we (i) compare the vertical polarity for each depth level separately with the vertical component polarity of (relatively) nearby broadband stations. Recordings by broadband stations are depicted as solid blue traces. The time window for which waveform data is retrieved coincides for all instruments, and is based on the computed arrival time at the broadband station that is most nearby. This broadband station varies from one event to the other, as these stations are not continuously online and also not all broadband stations are operational during the whole period for which the first-generation borehole network is evaluated (2010–2024). The travel times estimated using the TauP toolkit in conjunction with the IASP91 Earth model are depicted by means of vertical solid green lines. The one-minute long recordings are sorted and plotted based on these travel times.

In a third step, we use the correlation coefficient (e.g., Hadziioannou et al., 2009) to quantify the waveform coherence between the phase recorded by one of the broadband stations and the recording of that same phase by the geophone. We select the broadband station located closest to the set of geophones that recorded the phase. Recall from Section 4.1 that not all borehole stations were online continuously. Similarly, the data availability of the selected broadband stations varies as function of time. Consequently, the (reference) broadband station that is used to assess the borehole stations' polarity varies from one event to the other.

The correlation coefficient is defined as

$$CC(t) \equiv \frac{\int_{t'=t_1}^{t'=t_2} v_{bb}(t+t')v_{geo}(t')\mathrm{d}t'}{\sqrt{\int_{t'=t_1}^{t'=t_2} v_{bb}^2(t')\mathrm{d}t'}\sqrt{\int_{t'=t_1}^{t'=t_2} v_{geo}^2(t')\mathrm{d}t'}}, \tag{4.1}$$

where $v_{bb}(t)$ and $v_{geo}(t)$ denote the phase's vertical component recordings, and t_1 and t_2 the start and end time of the time window containing the arrival of the phase. We set t_1 to the computed arrival time (vertical solid green lines in Figure 4.5) and t_2 to $t_1 + 30$, and evaluate $CC(t)$ for time lags up to 5 s (maximum period of 20 seconds, divided by 4). The maximum of $CC(t)$ coincides with unity (i.e., 1) in case v_{bb} and v_{geo} coincide for a specific time lag $t \equiv t_{max}$. We denote the correlation coefficient's maximum by CC_{max}. In case the geophone's waveform needs to be multiplied with minus one in order to have $v_{bb}(t)$ and $v_{geo}(t)$ coincide for a specific time lag, the correlation coefficient will coincide with minus one for that time lag. We denote the correlation coefficient's minimum by CC_{min}. In reality CC_{min} and CC_{max} will never attain values of minus one and one, respectively, due to (i) small differences in the medium underlying the broadband station and the borehole station and (ii) station-specific noise. Nonetheless, a negative correlation coefficient whose absolute value exceeds CC_{max}, and which is sufficiently large, suggests a polarity that is flipped with respect to the polarity of the (reference) broadband station (and hence incorrect). Explicitly, we have

$$\text{Polarity} \equiv \begin{cases} \checkmark, & CC_{\max} > |CC_{\min}| \ \text{ and } \ CC_{max} > 0.6 \\ \times, & |CC_{\min}| > CC_{\max} \ \text{ and } \ |CC_{\min}| > 0.6 \\ \text{N/A}, & CC_{max} < 0.6 \ \text{ and } \ |CC_{\min}| < 0.6 \end{cases} \tag{4.2}$$

Figure 4.6 visualizes the polarity of the vertical component as determined using the teleseismic phase in Figure 4.5. The correlation coefficient is clearly a good indicator of a channel's polarity, with the teleseismic arrivals of the vertical channels of the aforementioned geophones NIW2, SUH2, and FDG2 having a $|CC_{\min}|$ exceeding both $CC_{\max}$ and 0.6. Similar figures, each associated with a specific event's teleseismic phase, can be found in the repository accompanying this report (Weemstra & Ruigrok, 2026). In general, the broadband station whose vertical component recording of the teleseismic phase was used to compute the correlation coefficient (see Equation (4.1)), is only plotted in case it is located on the map. For example, station WTSB, whose recording was used to determine the polarity of the geophones for the event on the 8th of August, 2017, is not within the extent of the map.

We extracted the results for the vertical components of all geophones of KNMI's first-generation borehole network, and present these in the six tables below (Tables 4.1, 4.2, 4.3, 4.4, 4.5, and 4.6). Note that station ZL2 was discontinued at the beginning of 2018. A number of conclusions can be drawn. First, the geophones of borehole stations NIW, SUH, and FDG inadvertently had their vertical polarity flipped during installation (recall that these are three of the six borehole stations that were newly installed

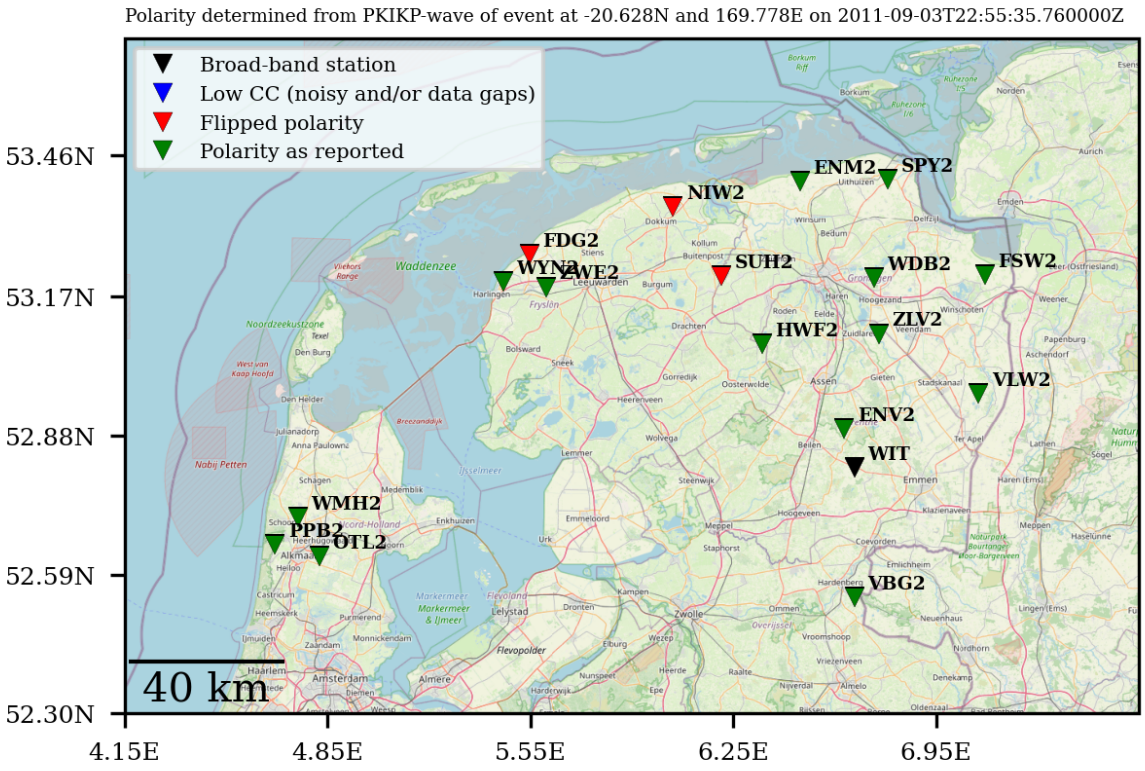

Figure 4.6: *Result of the evaluation of the conditions listed in Equation* (4.2) *using the teleseismic phase in Figure 4.5. Starting from the computed travel time, 30 seconds of this phase's vertical component recording by broadband station WIT constitute* v_{bb} *in Equation* (4.1).

around 2010, whereas the other twelve stations had been operational in a triggered mode since the nineties). Second, the replacement of the old systems with the Kinemetrics dataloggers (see Table 3.1) resulted in a flip of the polarity. Consequently, the reported polarity (dip of -90) does not match the actual polarity after the date of replacement for most borehole stations. We attribute this to the fact that the flip of the polarity induced in the electronics (from positive down to positive up; Dost et al., 2023), was not taken into consideration during installation of the Kinemetrics dataloggers. Obviously, this should have been accounted for. Note that stations NIW and SUH, whose vertical polarities were incorrect from the onset, therefore ended up with correct polarities after the Kinemetrics dataloggers were introduced (station FDG never had its datalogger replaced). Third, we observe that the vertical polarities (of the different geophones) of station FSW are rather ambiguous and require further scrutiny. Finally, several geophones start to generate rather noisy vertical component recordings at some point, which is manifested by the low correlation coefficients during later years. In Section 5, we provide a list of StationXML updates that should be implemented.

On a final note, we emphasize that although the vertical polarities of most of the first-generation borehole stations have been incorrect since 2016/2017, this has not affected the magnitudes that have been reported by the KNMI since that time. The reason for this is that the absolute amplitudes of the recordings are not affected by a flipped polarity. Moreover, the induced event's S-phases are used for estimating local magnitudes, and these phases are most pronounced on the horizontal channels.

Table 4.1: *Evaluation of the vertical polarity of all geophones at depth level 0 using teleseismic arrivals. Green check marks indicate that the vertical polarity is consistent with the dip reported in the StationXML file, whereas X marks indicate that this is not the case. In case recordings of a specific event were absent (geophone off-line), this is indicated by 'N/A' written in a black font. In case the event was only partly recorded (data gaps), or in case the phase's recording was of low quality (manifested by an absolute correlation coefficient that does not exceed 0.6), this is indicated by 'N/A' written in a blue font. Gray shaded cells indicate that the datalogger has been replaced at the time of the event.*

	ZLV0
2011-03-11	✓
2011-09-03	✓
2012-04-11	N/A
2013-05-23	N/A
2014-06-23	✓
2015-04-25	N/A
2016-04-17	✓

Table 4.2: *Evaluation of the vertical polarity of all geophones at depth level 1 using teleseismic arrivals. Green check marks indicate that the vertical polarity is consistent with the dip reported in the StationXML file, whereas X marks indicate that this is not the case. In case recordings of a specific event were absent (station down), this is indicated by 'N/A' written in a black font. In case the event was only partly recorded (data gaps), or in case the phase's recording was of low quality (manifested by an absolute correlation coefficient that does not exceed 0.6), this is indicated by 'N/A' written in a blue font. Gray shaded cells indicate that the datalogger has been replaced at the time of the event.*

	FSW1	**ENM1**	**WDB1**	**ZLV1**	**ZL21**	**ENV1**	**VLW1**	**VBG1**	**OTL1**
2011-03-11	✓	✓	✓	✓	✓	✓	✓	✓	✓
2011-09-03	✓	✓	✓	✓	✓	✓	✓	✓	✓
2012-04-11	✓	✓	✓	✓	✓	✓	✓	✓	✓
2013-05-23	✓	✓	✓	✓	✓	✓	✓	✓	✓
2014-06-23	✓	✓	✓	✓	✓	N/A	✓	✓	✓
2016-04-17	✓	✓	✓	✓	✗	✓	✓	✓	✓
2017-09-08	✓	✗	N/A	✗	✗	✗	✗	✗	✓
2018-01-23	✓	✗	N/A	✗	✗	✗	✗	✗	✓
2018-08-19	✗	✗	N/A	N/A		✗	✗	✗	✓
2019-05-26	✓	✗	N/A	N/A		✗	✗	N/A	✓
2020-07-22	N/A	✗	N/A	✗		N/A	N/A	✗	✗
2021-07-29	✓	✗	N/A	✗		✗	✗	✗	✗
2022-09-14	N/A	✗	N/A	✗		✗	N/A	✗	✗
2022-11-12	N/A	✗	N/A	N/A		✗	✗	✗	N/A
2023-05-10	N/A	✗	N/A	N/A		✗	N/A	✗	✗

	WMH1	**NIW1**	**SUH1**	**SPY1**	**FDG1**	**ZWE1**	**WYN1**	**HWF1**	**PPB1**
2011-03-11	✓	✗	✗	✓	✗	✓	✓	N/A	N/A
2011-09-03	✓	✗	✗	✓	✗	✓	✓	✓	✓
2012-04-11	✓	✗	✗	✓	✗	✓	✓	✓	✓
2013-05-23	✓	N/A	N/A	✓	✗	✓	✓	✓	✓
2014-06-23	✓	✗	✗	✓	✗	✓	✓	✓	✓
2016-04-17	N/A	✗	✗	N/A	✗	✓	✓	✓	✓
2017-09-08	N/A	✗	N/A	✗	✗	✓	✓	✗	✓
2018-01-23	N/A	✗	✓	✗	✗	✓	✓	✗	✓
2018-08-19	✓	✓	✓	✗	✗	✓	✓	✗	✓
2019-05-26	✓	N/A	N/A	N/A	✗	✓	✓	✗	✓
2020-07-22	✗	✓	✓	N/A	✗	✓	✓	✗	✗
2021-07-29	✗	✓	N/A	N/A	N/A	✓	✓	✗	✗
2022-09-14	✗	✓	✓	N/A	N/A	N/A	✓	✗	✗
2022-11-12	N/A	✓	✓	N/A	N/A	N/A	✓	✗	N/A
2023-05-10	✗	✓	✓	N/A	N/A	N/A	✓	✗	✗

Table 4.3: *Evaluation of the vertical polarity of all geophones at depth level 2 using teleseismic arrivals. Green check marks indicate that the vertical polarity is consistent with the dip reported in the StationXML file, whereas X marks indicate that this is not the case. In case recordings of a specific event were absent (station down), this is indicated by 'N/A' written in a black font. In case the event was only partly recorded (data gaps), or in case the phase's recording was of low quality (manifested by an absolute correlation coefficient that does not exceed 0.6), this is indicated by 'N/A' written in a blue font. Gray shaded cells indicate that the datalogger has been replaced at the time of the event.*

	FSW2	**ENM2**	**WDB2**	**ZLV2**	**ZL22**	**ENV2**	**VLW2**	**VBG2**	**OTL2**
2011-03-11	✓	✓	✓	✓	✓	✓	✓	✓	✓
2011-09-03	✓	✓	✓	✓	✓	✓	✓	✓	✓
2012-04-11	✓	✓	✓	✓	✓	✓	✓	✓	✓
2013-05-23	✓	✓	✓	✓	✓	✓	✓	✓	✓
2014-06-23	✓	✓	✓	✓	✓	N/A	N/A	✓	✓
2016-04-17	✓	✓	✓	✓	✗	✓	✗	✓	✓
2017-09-08	✗	✗	N/A	✗	✗	✗	N/A	✗	✓
2018-01-23	✗	✗	N/A	✗	✗	✗	N/A	✗	N/A
2018-08-19	N/A	✗	N/A	N/A		✗	N/A	✗	✓
2019-05-26	N/A	✗	N/A	N/A		✗	N/A	N/A	✓
2020-07-22	N/A	✗	✗	✗		N/A	N/A	✗	✗
2021-07-29	N/A	✗	N/A	✗		✗	N/A	✗	✗
2022-09-14	N/A	✗	✗	✗		✗	N/A	✗	✗
2022-11-12	✗	✗	✗	✗		N/A	N/A	N/A	✗
2023-05-10	N/A	✗	N/A	✗		✗	N/A	✗	✗

	WMH2	**NIW2**	**SUH2**	**SPY2**	**FDG2**	**ZWE2**	**WYN2**	**HWF2**	**PPB2**
2011-03-11	✓	✗	✗	✓	✗	✓	✓	N/A	N/A
2011-09-03	✓	✗	✗	✓	✗	✓	✓	✓	✓
2012-04-11	✓	✗	✗	✓	✗	✓	✓	✓	✓
2013-05-23	✓	N/A	N/A	✓	✗	✓	✓	✓	✓
2014-06-23	✓	✗	✗	✓	✗	✓	✓	✓	✓
2016-04-17	N/A	✗	✗	N/A	N/A	✓	✓	✓	✓
2017-09-08	N/A	✗	N/A	✗	N/A	✓	✓	✗	✓
2018-01-23	N/A	N/A	✓	✗	N/A	✓	✓	✗	✓
2018-08-19	✓	N/A	✓	✗	N/A	✓	✓	✗	✓
2019-05-26	✓	N/A	N/A	✗	N/A	✓	✓	✗	✓
2020-07-22	✗	N/A	✓	✗	N/A	✓	✓	✗	✗
2021-07-29	✗	✓	N/A	✗	N/A	✓	✓	N/A	✗
2022-09-14	✗	N/A	✓	✗	N/A	N/A	✓	N/A	✗
2022-11-12	✗	N/A	✓	✗	N/A	N/A	✓	N/A	N/A
2023-05-10	✗	✓	✓	✗	N/A	N/A	✓	N/A	✗

Table 4.4: *Evaluation of the vertical polarity of all geophones at depth level 3 using teleseismic arrivals. Green check marks indicate that the vertical polarity is consistent with the dip reported in the StationXML file, whereas X marks indicate that this is not the case. In case recordings of a specific event were absent (station down), this is indicated by 'N/A' written in a black font. In case the event was only partly recorded (data gaps), or in case the phase's recording was of low quality (manifested by an absolute correlation coefficient that does not exceed 0.6), this is indicated by 'N/A' written in a blue font. Gray shaded cells indicate that the datalogger has been replaced at the time of the event.*

	FSW3	**ENM3**	**WDB3**	**ZLV3**	**ZL23**	**ENV3**	**VLW3**	**VBG3**	**OTL3**
2011-03-11	✓	✓	N/A	✓	✓	✓	✓	✓	✓
2011-09-03	✓	✓	N/A	✓	✓	✓	✓	✓	✓
2012-04-11	✓	✓	✓	✓	✓	✓	✓	✓	✓
2013-05-23	✓	✓	N/A	✓	✓	✓	✓	✓	✓
2014-06-23	✓	✓	N/A	✓	✓	N/A	✓	✓	✓
2016-04-17	✓	✓	✗	✓	✗	✓	✓	✓	✓
2017-09-08	✗	✗	N/A	✗	✗	✗	✗	✗	N/A
2018-01-23	N/A	✗	N/A	✗	✗	✗	✗	✗	✓
2018-08-19	N/A	✗	N/A	N/A		✗	✗	✗	✓
2019-05-26	✗	✗	N/A	N/A		✗	✗	N/A	✓
2020-07-22	N/A	✗	N/A	✗		N/A	N/A	✗	✗
2021-07-29	N/A	✗	N/A	✗		✗	✗	✗	✗
2022-09-14	N/A	✗	N/A	✗		✗	N/A	✗	✗
2022-11-12	✓	✗	✓	✗		✗	✗	N/A	N/A
2023-05-10	N/A	✗	N/A	✗		✗	N/A	✗	✗

	WMH3	**NIW3**	**SUH3**	**SPY3**	**FDG3**	**ZWE3**	**WYN3**	**HWF3**	**PPB3**
2011-03-11	✓	✗	✗	✓	✗	✓	✓	N/A	N/A
2011-09-03	✓	✗	✗	✓	✗	✓	✓	✓	✓
2012-04-11	✓	✗	✗	✓	✗	✓	✓	✓	✓
2013-05-23	✓	N/A	N/A	✓	✗	✓	✓	✓	✓
2014-06-23	✓	✗	✗	✓	✗	✓	N/A	✓	✓
2016-04-17	N/A	✗	✗	N/A	N/A	✓	✗	✓	✓
2017-09-08	N/A	N/A	N/A	✗	N/A	✓	N/A	✗	✓
2018-01-23	N/A	N/A	✓	✗	N/A	✓	N/A	✗	✓
2018-08-19	✓	✓	✓	✗	N/A	✓	N/A	✗	✓
2019-05-26	✓	N/A	N/A	✗	N/A	✓	N/A	✗	✓
2020-07-22	✗	✓	✓	✗	N/A	✓	N/A	✗	✗
2021-07-29	✗	✓	N/A	✗	N/A	✓	N/A	✗	✗
2022-09-14	✗	✓	✓	N/A	N/A	N/A	N/A	✗	✗
2022-11-12	✗	✓	✓	✗	N/A	N/A	N/A	✗	N/A
2023-05-10	✗	✗	✓	N/A	N/A	N/A	N/A	✗	✗

Table 4.5: *Evaluation of the vertical polarity of all geophones at depth level 4 using teleseismic arrivals. Green check marks indicate that the vertical polarity is consistent with the dip reported in the StationXML file, whereas X marks indicate that this is not the case. In case recordings of a specific event were absent (station down), this is indicated by 'N/A' written in a black font. In case the event was only partly recorded (data gaps), or in case the phase's recording was of low quality (manifested by an absolute correlation coefficient that does not exceed 0.6), this is indicated by 'N/A' written in a blue font. Gray shaded cells indicate that the datalogger has been replaced at the time of the event.*

	FSW4	**ENM4**	**WDB4**	**ZLV4**	**ZL24**	**ENV4**	**VLW4**	**VBG4**	**OTL4**
2011-03-11	✓	✓	✓	✓	✓	✓	N/A	✓	✓
2011-09-03	✓	✓	✓	✓	✓	✓	N/A	✓	✓
2012-04-11	✓	✓	✓	✓	✓	✓	✓	✓	✓
2013-05-23	✓	✓	✓	✓	✓	✓	N/A	✓	✓
2014-06-23	✓	✓	✓	✓	✓	N/A	N/A	✓	✓
2016-04-17	✓	✓	✓	✓	✗	N/A	✗	✓	✓
2017-09-08		✗	N/A	✗	✗	✗	N/A	✗	N/A
2018-01-23		✗	N/A	✗	✗	✗	N/A	✗	N/A
2018-08-19		✗	N/A	N/A		✗	N/A	✗	✓
2019-05-26		✗	N/A	N/A		✗	N/A	N/A	✓
2020-07-22		✗	✗	✗		N/A	N/A	✗	✗
2021-07-29		✗	N/A	✗		✗	N/A	✗	✗
2022-09-14		✗	✓	✗		✗	N/A	✗	✗
2022-11-12		✗	✗	✗		N/A	✗	N/A	N/A
2023-05-10		✗	N/A	✗		✗	N/A	✗	✗

	WMH4	**NIW4**	**SUH4**	**SPY4**	**FDG4**	**ZWE4**	**WYN4**	**HWF4**	**PPB4**
2011-03-11	✓	✗	✗	✓	✗	✓	✓	N/A	N/A
2011-09-03	✓	✗	✗	✓	✗	✓	✓	✓	✓
2012-04-11	✓	✗	✗	✗	✗	✓	✓	✓	✓
2013-05-23	✓	N/A	N/A	✓	✗	✓	✓	✓	✓
2014-06-23	✓	✗	✗	✓	✗	✓	✓	✓	✓
2016-04-17	N/A	✗	✗	N/A	✓	✓	✓	✓	✓
2017-09-08	N/A	✗	N/A	✗	N/A	✓	✓	✗	✓
2018-01-23	N/A	✗	✓	✗	N/A	✓	✓	✗	✓
2018-08-19	✓	✓	✓	✗	N/A	✓	✓	✗	✓
2019-05-26	✓	N/A	N/A	✗	N/A	✓	✓	✗	✓
2020-07-22	✗	✓	✓	✗	N/A	✓	✓	✗	✗
2021-07-29	✗	✓	N/A	✗	N/A	✓	✓	✗	✗
2022-09-14	✗	✓	✓	N/A	N/A	N/A	✓	✗	✗
2022-11-12	N/A	✓	N/A	✗	N/A	N/A	✓	✗	N/A
2023-05-10	✗	✓	✓	✓	N/A	N/A	✓	✗	✗

Table 4.6: *Evaluation of the vertical polarity of all geophones at depth level 5 using teleseismic arrivals. Green check marks indicate that the vertical polarity is consistent with the dip reported in the StationXML file, whereas X marks indicate that this is not the case. In case recordings of a specific event were absent (geophone off-line), this is indicated by 'N/A' written in a black font. In case the event was only partly recorded (data gaps), or in case the phase's recording was of low quality (manifested by an absolute correlation coefficient that does not exceed 0.6), this is indicated by 'N/A' written in a blue font. Gray shaded cells indicate that the datalogger has been replaced at the time of the event.*

	FSW5
2011-03-11	✓
2011-09-03	✓
2012-04-11	✓
2013-05-23	✓
2014-06-23	✓
2015-04-25	N/A
2016-04-17	✓
2017-09-08	N/A
2018-01-23	N/A
2018-08-19	N/A
2019-05-26	N/A
2020-07-22	N/A
2021-07-29	N/A
2022-09-14	N/A
2022-11-12	✓
2023-05-10	N/A

We validate the teleseismic-derived polarities in Tables 4.1 - 4.6 by comparing the vertical-component recordings at the different depth levels. This is done for each borehole station separately using the same teleseismic recordings. These results can be found in the repository accompanying this report (Weemstra & Ruigrok, 2026). The first conclusion that can be drawn from this comparison is that, for all borehole stations, the polarities of the HHZ channels at the different depth levels are consistent (apart from dead/noisy/malfunctioning channels). In other words, we do not observe polarities to be flipped from one depth level to another depth level. Second, the recordings by the HHZ channels of the geophones of station FSW appear to be corrupted from (at the latest) 2017-09-08. As we detail in Section 4.3, all recordings by this station are in fact corrupt from the moment the datalogger has been replaced (2016-06-14). This was the result of miswiring in the shunt-box. The recordings by FSW during the third epoch have therefore been removed from our waveform archive. Note that, in general, the evaluated waveforms allow for the identification of malfunctioning or noisy HHZ channels. The evaluation of the quality of the recordings (Section 4.3) is hence partly based on these waveform comparisons.

4.2.2 Orientation of the horizontal components

The StationXML's dip describing the polarity of vertical channels is either -90 or 90 degrees. This is because we know that the vertical component's amplitudes are positive either for motions towards the Earth's surface or away from it. Instead, the orientations of the horizontal components take on values on a continuous scale between 0 and 360 degrees (their dip being 0). For most of the first-generation borehole stations, the orientations of the geophones were determined by check shots (Diephuis & Asmussen, 1995). These orientations vary from one depth level to another, and are listed in the StationXMLs as a channels' *azimuth*. Assuming, apart from a 180 degrees ambiguity, these reported azimuths to be correct, we limit the analysis of these stations to an evaluation of the polarity of the reported orientations.

The StationXML azimuths of channel HHN of all geophones of the first-generation borehole network are listed in Table 4.7. HHE channels have an azimuth that is 90 degrees higher. The orientations of the geophones of NIW, SUH, SPY, FDG, ZWE, and WYN were not determined. For three of these six stations (NIW, SUH, and SPY), however, we have sufficient data to determine the orientations of the

Table 4.7: *Reported (StationXML) orientations of all borehole geophones. The azimuths of the N-components are listed. For both epochs we checked the polarity of the reported orientations. Green checkmarks indicate that the polarity appears to be consistent with the reported orientation, whereas X marks indicate that 180 degrees need to added to the reported orientations. Note that the orientations of NIW, SUH, SPY, FDG, ZWE, and WYN were not determined. The data recorded by FSW during the third epoch has been removed (detailed in Section 4.3); hence the 'N/A'.*

	level 1	level 2	level 3	level 4	level 5	epoch 2	epoch 3
FSW	FSW1: 53	FSW2: 204	FSW3: 11	FSW4: 214	FSW5: 278	✓	N/A
ENM	ENM1: 122	ENM2: 177	ENM3: 164	ENM4: 91		✓	✗
WDB	WDB1: 274	WDB2: 52	WDB3: 311	WDB4: 70		✗	✓
ZLV	ZLV0: 0	ZLV1: 244	ZLV2: 313	ZLV3: 42	ZLV4: 310	✗	✓
ZL2	ZL21: 205	ZL22: 170	ZL23: 340	ZL24: 224		✗	✓
ENV	ENV1: 142	ENV2: 157	ENV3: 27	ENV4: 131		✗	✓
VLW	VLW1: 22	VLW2: 72	VLW3: 303	VLW4: 269		✗	✓
VBG	VBG1: 340	VBG2: 294	VBG3: 104	VBG4: 90		✓	✗
HWF	HWF1: 346	HWF2: 77	HWF3: 162	HWF4: 19		✗	✓
OTL	OTL1: 269	OTL2: 11	OTL3: 145	OTL4: 295		✗	✓
PPB	PPB1: 355	PPB2: 135	PPB3: 276	PPB4: 116		✓	✗
WMH	WMH1: 80	WMH2: 189	WMH3: 100	WMH4: 30		✗	✓
NIW	NIW1: 0	NIW2: 0	NIW3: 0	NIW4: 0		N/A	N/A
SUH	SUH1: 0	SUH2: 0	SUH3: 0	SUH4: 0		N/A	N/A
SPY	SPY1: 0	SPY2: 0	SPY3: 0	SPY4: 0		N/A	N/A
FDG	FDG1: 0	FDG2: 0	FDG3: 0	FDG4: 0		N/A	N/A
ZWE	ZWE1: 0	ZWE2: 0	ZWE3: 0	ZWE4: 0		N/A	N/A
WYN	WYN1: 0	WYN2: 0	WYN3: 0	WYN4: 0		N/A	N/A

horizontal components using explosions and local induced events; this is described further below. The other three stations (FDG, ZWE, and WYN) are located in western Friesland, which makes it more difficult to determine the geophone orientations. This is due to the absence of induced events in that area. For these stations, we will estimate the orientations of the geophones in a future study. For the geophones whose StationXMLs do list non-zero azimuths for the horizontal channels (first twelve stations in Table 4.7), we assess the validity of the reported geophone orientations by means of direct P-waves generated by nearby induced seismic events.

The orientations of the geophones of NIW, SUH, and SPY are determined using local induced events and explosions. From the local events we use a time window around the incoming P wave. Typically, for each geophone, many dozens of local earthquakes with sufficient signal-to-noise can be used. For the explosions we distinguish between (i) controlled explosions of UXO (un-exploded ordnance) in the North Sea (Ruigrok et al., 2019) and (ii) controlled explosions commissioned by the NAM (the operator of the Groningen gas field) for better characterizing the top 800 meters of unconsolidated sediments. For both type of explosions very accurate locations are known and they both generate radially polarized guided waves that travel through the loose sediments with approximately P-wave velocities.

For estimating the orientation, a time window around the specific arrival is taken and the polarization is extracted from the data variance tensor, as described, e.g., in Aster et al. (1990). The angle between the measured polarization and the radial direction is an estimate of the geophone's azimuth. By an anti-clockwise rotation of the components with this azimuth, the components are rotated to North and East, or South and West, due to the existence of a 180° ambiguity. This ambiguity is solved by ensuring that the radial component for an incoming P-wave is in phase with the vertical component (Figure 4.7).

Each local earthquake or controlled explosion yields an estimate of the azimuth and a variance thereof, which is based on the deviation from linearity of the polarization. If there are no interfering arrivals, incoming P waves and guided waves have a near perfect linear polarization. In practice, there are also scattered waves that arrive within the same time window, which result in a deviation from linearity and a higher uncertainty of the estimated azimuth. The individual estimates are combined to a weighted average in which the weights are the variances of the individual estimates, and the variances over all

Table 4.8: *Azimuths for the HHN channels of the borehole geophones of NIW, SUH, and SPY during the second epoch. The last column indicates whether the determined azimuths remained the same during the third epoch (green checkmark) or whether the horizontal polarity appears to have flipped while transitioning from the second to the third epoch (red X mark). The latter implies that 180 degrees needs to added to the listed azimuths to obtain the correct horizontal orientations during the third epoch. The azimuths in the meta-data have been updated based on these findings.*

	level 1		level 2		level 3		level 4		epoch 3
NIW	NIW1:	159	NIW2:	198	NIW3:	234	NIW4:	210	✗
SUH	SUH1:	108	SUH2:	87	SUH3:	105	SUH4:	72	✗
SPY	SPY1:	316	SPY2:	286	SPY3:	303	SPY4:	220	✗

P-wave based and all guided-wave based estimates. The resulting weighted averages, rounded off to integer degrees and 180°-ambiguity corrected, are tabulated in Table 4.8.

In the first iteration, the above approach did not result in estimating the azimuths with a reasonable uncertainty. It turned out that the HHE and HHN components were switched for all geophones at NIW, SPY and SUH. After locally renaming the HHN component to HHE and vice versa, the above results were obtained. This renaming has also been performed in KNMI's waveform database.

There is a fair chance that a similar component switching has occurred at other borehole stations that were installed in 2009 and 2010: FDG, WYN and ZWE. As previously noted, component orientations are still to be estimated at these locations. In this future exercise, the likely component switching will be a point of attention.

The polarities of the orientations reported in Table 4.7 are checked using P-waves generated by nearby induced seismic events. This merely applies to the first twelve stations. Specifically, we create station-specific catalogs which contain all eligible induced events. These events are selected based on their epicentral distance and (local) magnitude. The larger the epicentral distance, the larger the magnitude needs to be in order for an event to be included in the station-specific catalog. For each of the events in the station-specific catalog, we rotate the recordings by the horizontal components towards a radial and transverse direction (e.g., Hofman et al., 2017; Masfara & Weemstra, 2024). In case the radial and vertical component's recording of the (incoming) direct P wave are *in phase*, the reported azimuth can be assumed to be correct. If, instead, the recordings of the direct P wave exhibit an opposite polarity on the radial and vertical component, 180 degrees needs to be added to the reported azimuths. While plotting the waveforms, we of course ensure the vertical component recordings to be positive up. That is, we multiplied vertical component recordings by minus one in case the vertical polarity was found to be incorrect (see Tables 4.1 – 4.6).

The plots of the incoming P-waves of the events in the station-specific catalogs can be found in Weemstra and Ruigrok (2026). We do not only plot the vertical component and radial component's recording around the (expected) time of the arrival of the P-wave, but also the vertical, radial, and transverse component's recording around the expected time of arrival of the direct S-wave. If the reported azimuth is correct, then the radial and vertical component's recording of the (incoming) direct S wave are in *anti-phase*. Average arrival times are computed using the (simple) polynomial travel time models described in Section 2.6.1 of Ruigrok et al. (2023). Although all plots are stored on Weemstra and Ruigrok (2026), we include in this report two clear examples for each of the eleven borehole stations: one showing the (dis)agreement of the vertical and radial polarity during the second epoch and another showing the (dis)agreement during the third epoch. These are shown in Figures 4.7 - 4.24.

For most events in the station-specific catalogs, visual inspection suffices to determine whether or not the polarity of the N and E components is correct. We therefore neither discuss Figures 4.8 - 4.24 separately, nor the other figures in Weemstra and Ruigrok (2026). We will only do this briefly for station FSW (Figure 4.7). The other figures speak for themselves and the final outcome of our visual inspections can be found in the last two columns of Table 4.7. Figure 4.7 reveals that the direct P-wave, which arrives at approximately 8.2 seconds after the event at FSW5 and at about 8.35 seconds at FSW1, has the same phase on both the radial and vertical component. In other words, the azimuths reported in

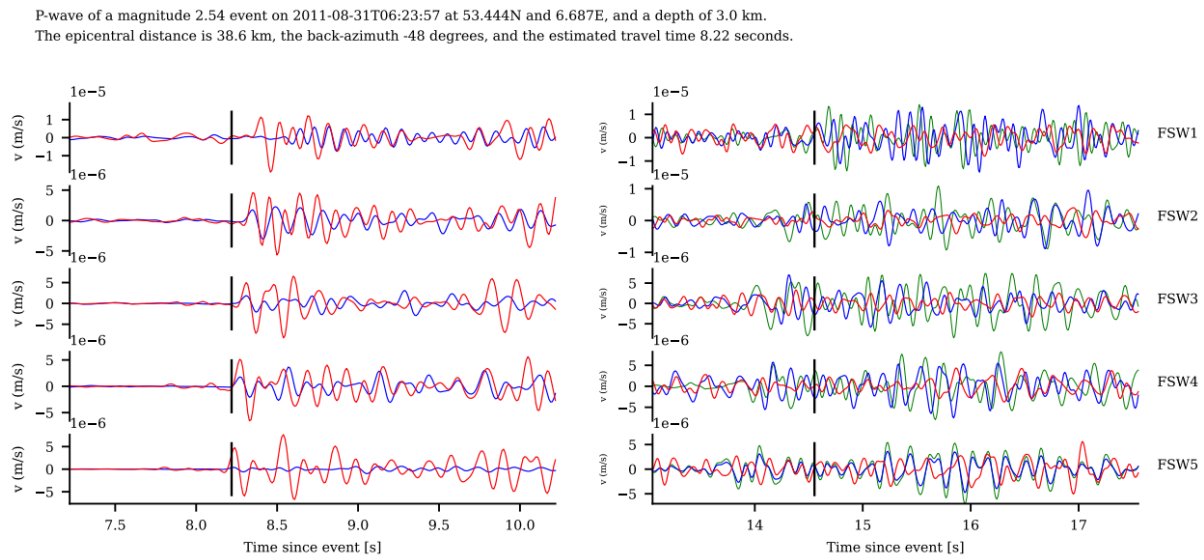

Figure 4.7: *Direct P-wave (left) and direct S-wave (right) at station FSW of a (relatively) nearby induced event in the north of the Netherlands during the second epoch; event details are provided at the top of the figure. The red, blue, and green traces represent the vertical, radial, and transverse components, respectively. The latter two are the result of a first rotation of the HHN and HHE recordings to north and east using the azimuths listed in Table 4.7, and a consecutive rotation using the back-azimuth of the event to the radial and transverse directions. The vertical black lines indicate the mean expected time of arrival predicted by the polynomial travel time models in Ruigrok et al. (2023).*

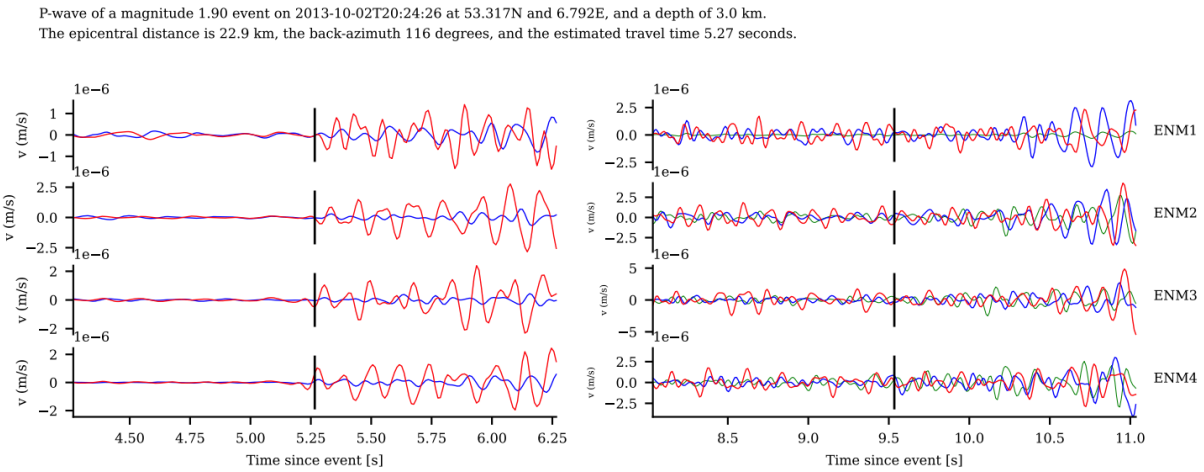

Figure 4.8: *Direct P-wave (left) and direct S-wave (right) at station ENM of a (relatively) nearby induced event in the north of the Netherlands during the second epoch; event details are provided at the top of the figure. For an explanation of the colors, we refer to the caption of Figure 4.7.*

the StationXML are most likely correct. The direct S-wave is less pronounced, which applies to many event-station combinations.

Table 4.7 lists for each of the stations whether the polarity of the reported orientations is correct (Green checkmarks) or 180 degrees off (red checkmarks). This is done on a per-epoch basis. In occurs regularly that one or more channels are either dead or extremely noisy. We do not indicate this explicitly here, since these channels are discussed in detail in Section 4.3; a summary of the dead channels can be found in Table 4.9. Station FSW is an extreme case in the sense that all channels of all geophones appear to be corrupt staring from the transition from the second to the third epoch (discussed in more detail in Section 4.3). Consequently, we could not (and need not) determine its horizontal polarity during the third epoch.

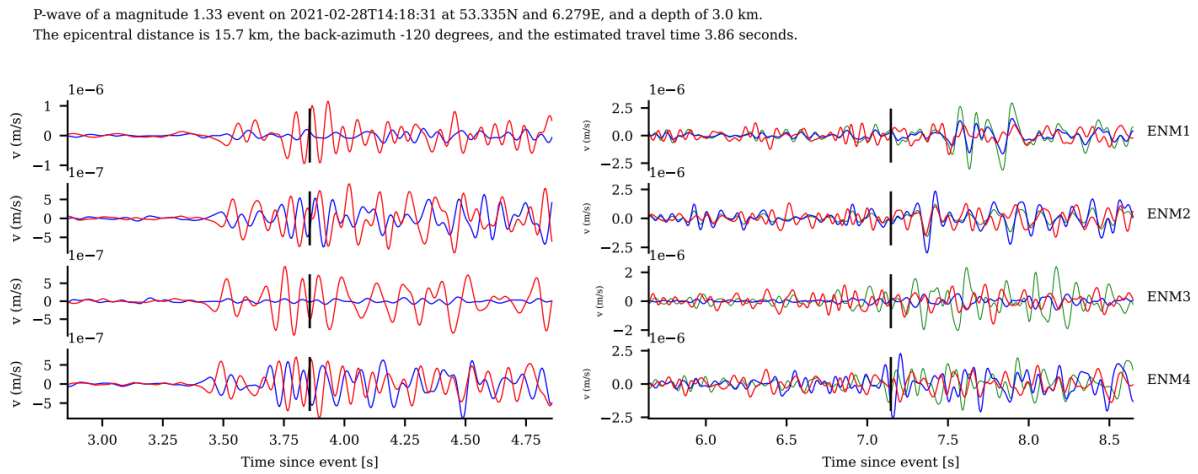

Figure 4.9: *Direct P-wave (left) and direct S-wave (right) at station ENM of a (relatively) nearby induced event in the north of the Netherlands during the third epoch; event details are provided at the top of the figure. For an explanation of the colors, we refer to the caption of Figure 4.7.*

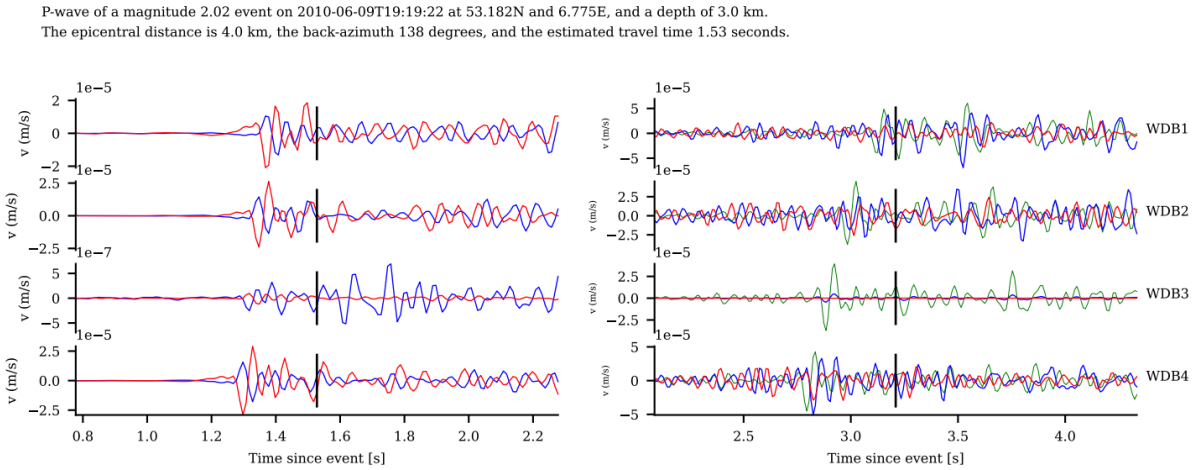

Figure 4.10: *Direct P-wave (left) and direct S-wave (right) at station WDB of a (relatively) nearby induced event in the north of the Netherlands during the second epoch; event details are provided at the top of the figure. For an explanation of the colors, we refer to the caption of Figure 4.7.*

We find that only the azimuths of the horizontal components for FSW, ENM, PPB and VBG appear to agree with the ones in the StationXML. For the other eight borehole stations, the azimuths appear to be 180 degrees off. This due to the fact that, while determining the orientations, Diephuis and Asmussen (1995) suspected a difference in the vertical component. Instead, this appeared to be the case for the horizontal components of these stations (Dost et al., 2023). Consequently, azimuths were filed that deviated 180 degrees from the actual azimuths for these seven stations. This was already recognized by Dost et al. (2023), but the meta-data was only updated for the epoch that was investigated in that report (Epoch 1). We have now also updated the orientations in the meta-data for both the second and third epoch.

Recall from our description of the vertical components' polarities (Section 4.2.1) that a flip of the polarity was induced by the electronic circuits effectuating the different filters during the first and second epoch. Our analysis reveals that, perhaps not surprisingly, this was also the case for the horizontal components. And because this electronically induced polarity flip was not accounted for while hooking these stations up to the Kinemetric dataloggers at the start of the third epoch, stations hitherto exhibiting a horizontal polarity that was 180 degrees off had a correct horizontal orientation during the third epoch. Similarly, the azimuths of the HHN and HHE channels of borehole stations FSW, ENM, PPB and VBG are 180 degrees off during the third epoch. We finally note that the absence of (sufficiently strong) induced events

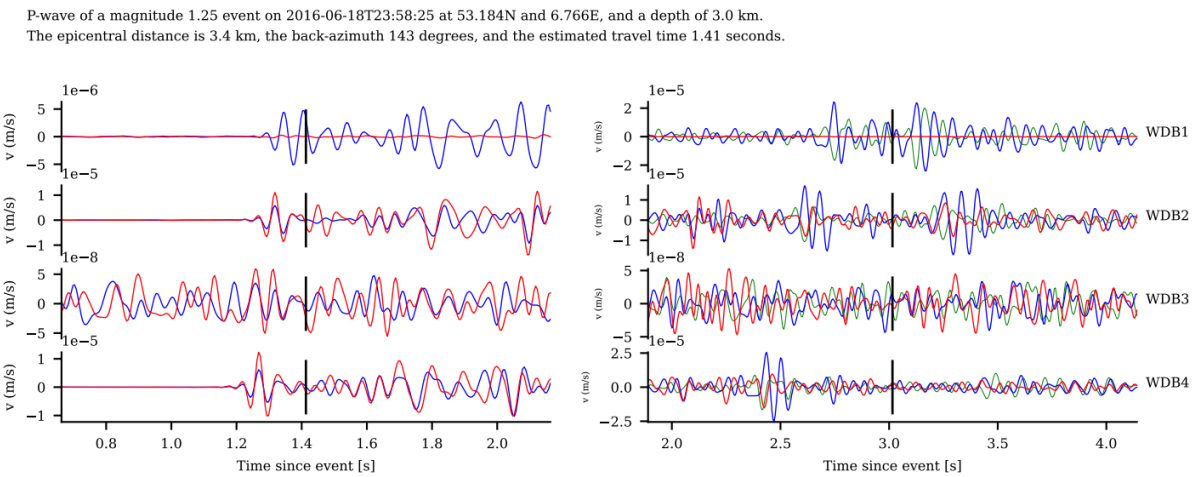

Figure 4.11: *Direct P-wave (left) and direct S-wave (right) at station WDB of a (relatively) nearby induced event in the north of the Netherlands during the third epoch; event details are provided at the top of the figure. For an explanation of the colors, we refer to the caption of Figure 4.7.*

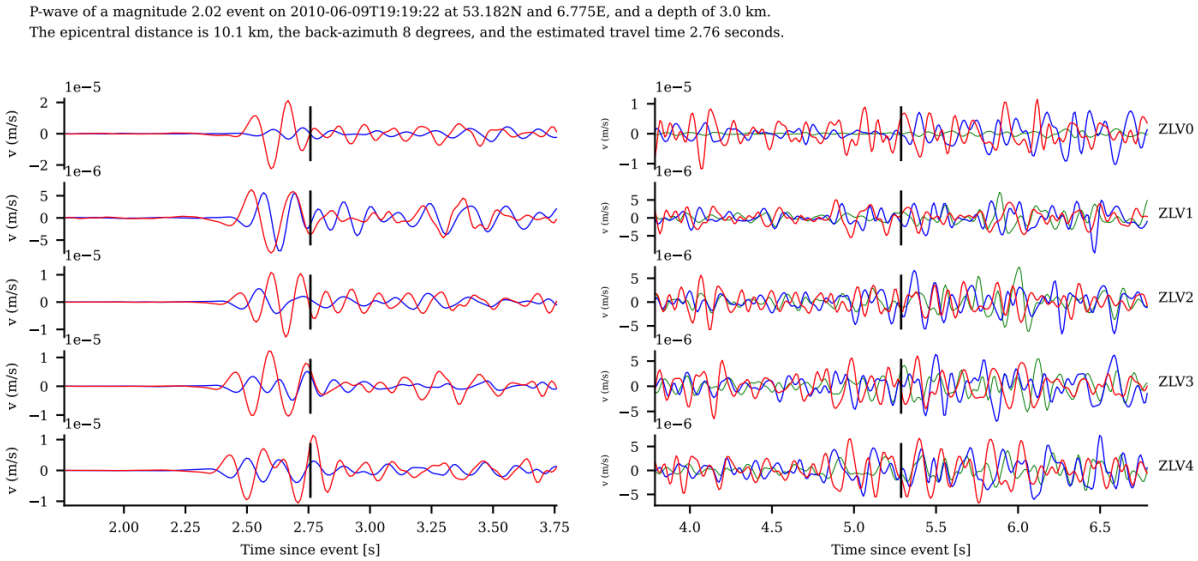

Figure 4.12: *Direct P-wave (left) and direct S-wave (right) at station ZLV of a (relatively) nearby induced event in the north of the Netherlands during the second epoch; event details are provided at the top of the figure. For an explanation of the colors, we refer to the caption of Figure 4.7.*

in North-Holland during the third epoch rendered it difficult to determine the validity of the azimuths of stations OTL, PPB, and WMH during that epoch. Because the same hardware was removed and placed at these three stations while transitioning to the third epoch, however, we simply assume that the horizontal orientation of these three stations also flipped while transitioning from the second to the third epoch (see Table 4.7). This assumption will be validated in a future study of the orientations.

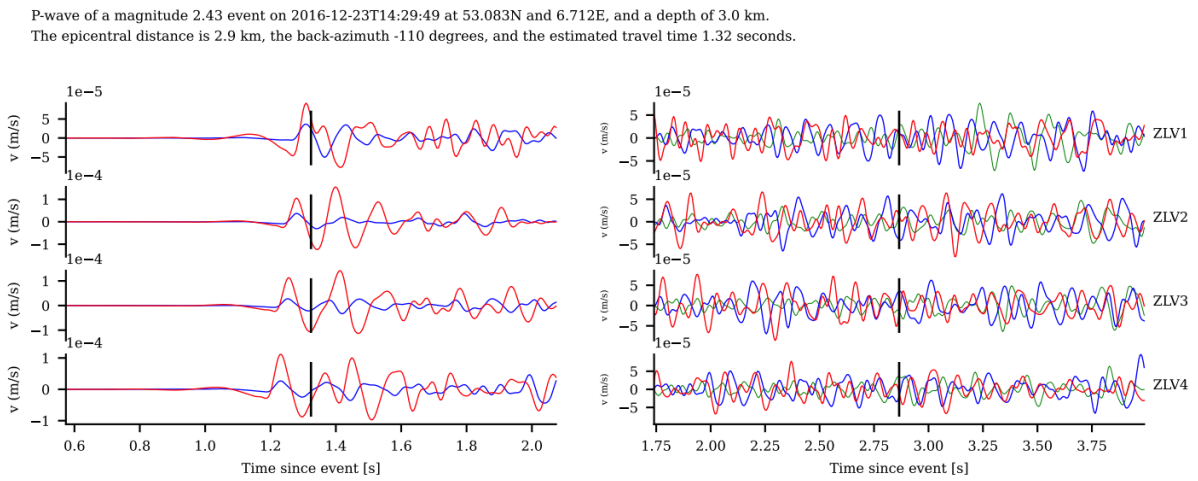

Figure 4.13: *Direct P-wave (left) and direct S-wave (right) at station ZLV of a (relatively) nearby induced event in the north of the Netherlands during the third epoch; event details are provided at the top of the figure. For an explanation of the colors, we refer to the caption of Figure 4.7.*

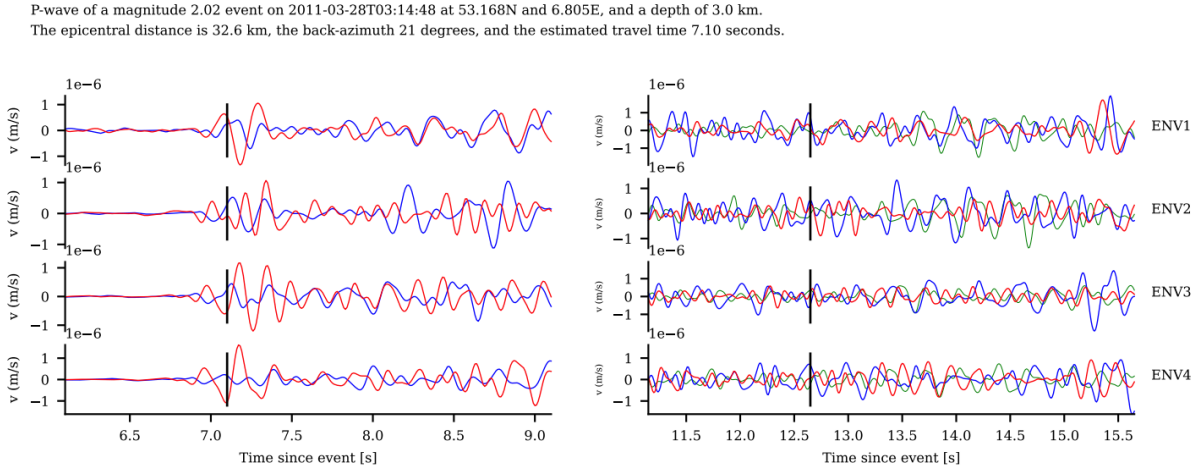

Figure 4.14: *Direct P-wave (left) and direct S-wave (right) at station ENV of a (relatively) nearby induced event in the north of the Netherlands during the second epoch; event details are provided at the top of the figure. For an explanation of the colors, we refer to the caption of Figure 4.7.*

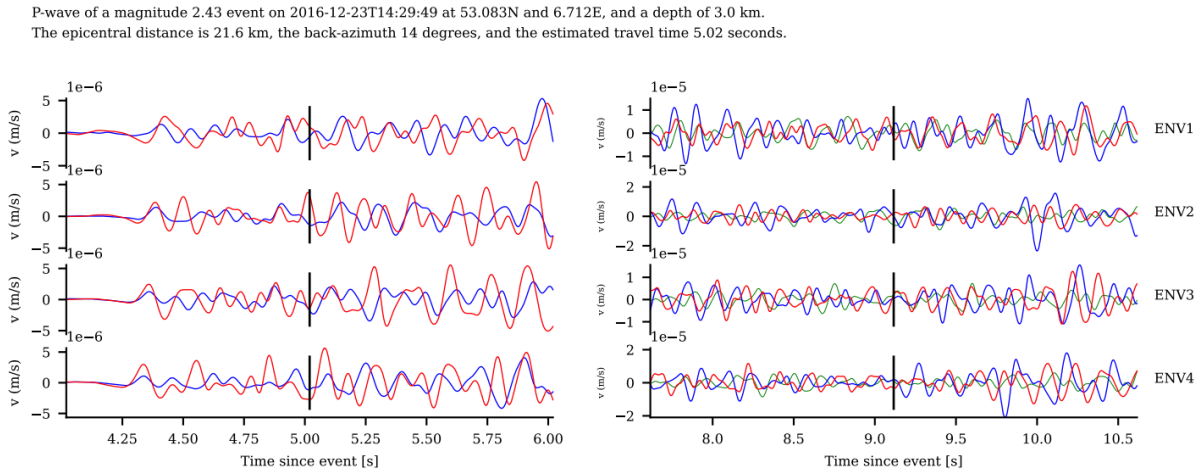

Figure 4.15: *Direct P-wave (left) and direct S-wave (right) at station ENV of a (relatively) nearby induced event in the north of the Netherlands during the third epoch; event details are provided at the top of the figure. For an explanation of the colors, we refer to the caption of Figure 4.7.*

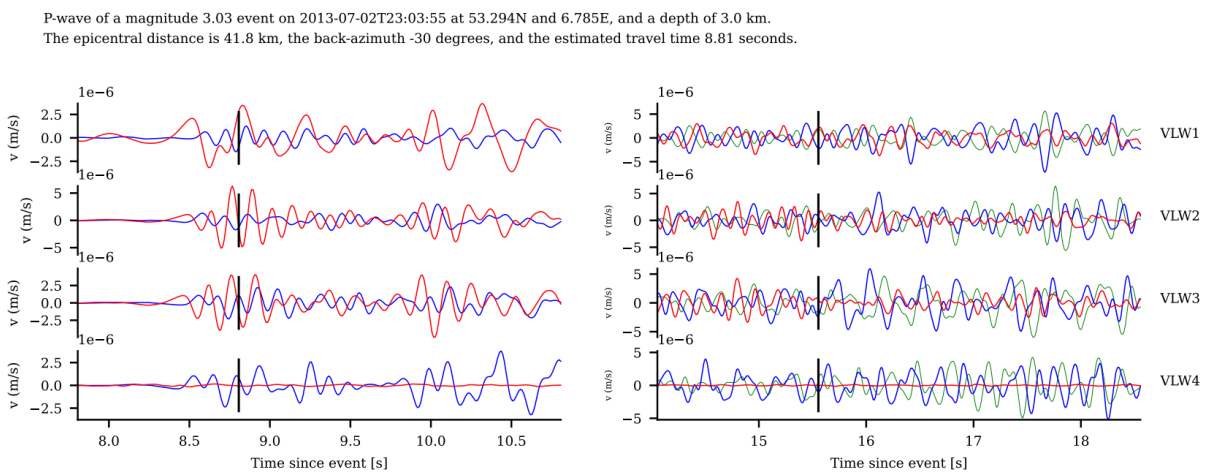

Figure 4.16: *Direct P-wave (left) and direct S-wave (right) at station VLW of a (relatively) nearby induced event in the north of the Netherlands during the second epoch; event details are provided at the top of the figure. For an explanation of the colors, we refer to the caption of Figure 4.7.*

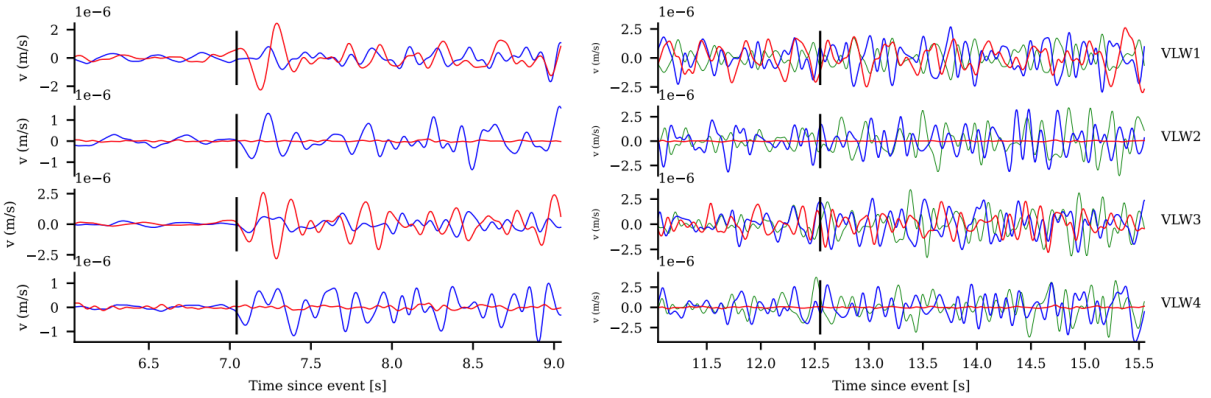

Figure 4.17: *Direct P-wave (left) and direct S-wave (right) at station VLW of a (relatively) nearby induced event in the north of the Netherlands during the third epoch; event details are provided at the top of the figure. For an explanation of the colors, we refer to the caption of Figure 4.7.*

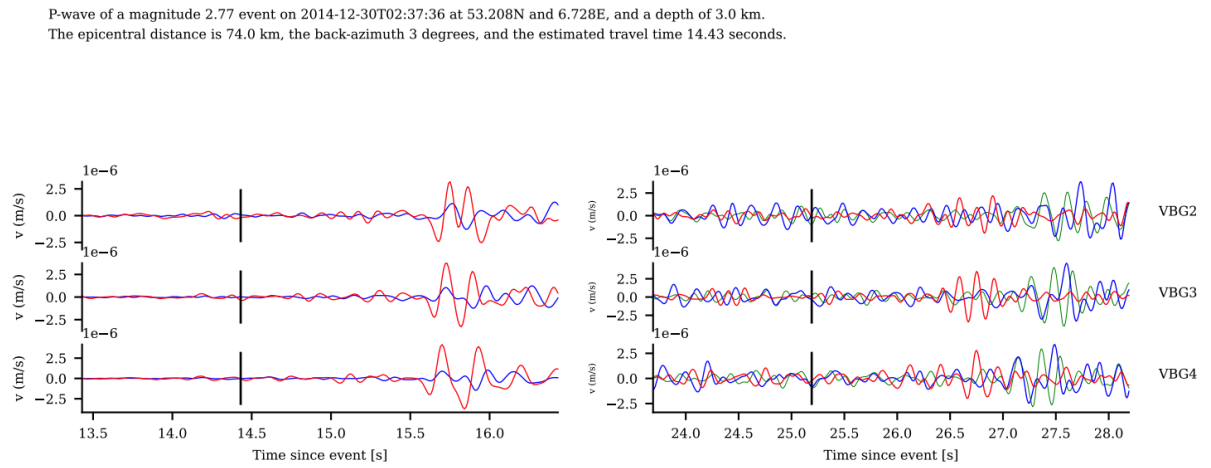

Figure 4.18: *Direct P-wave (left) and direct S-wave (right) at station VBG of a (relatively) nearby induced event in the north of the Netherlands during the second epoch; event details are provided at the top of the figure. For an explanation of the colors, we refer to the caption of Figure 4.7.*

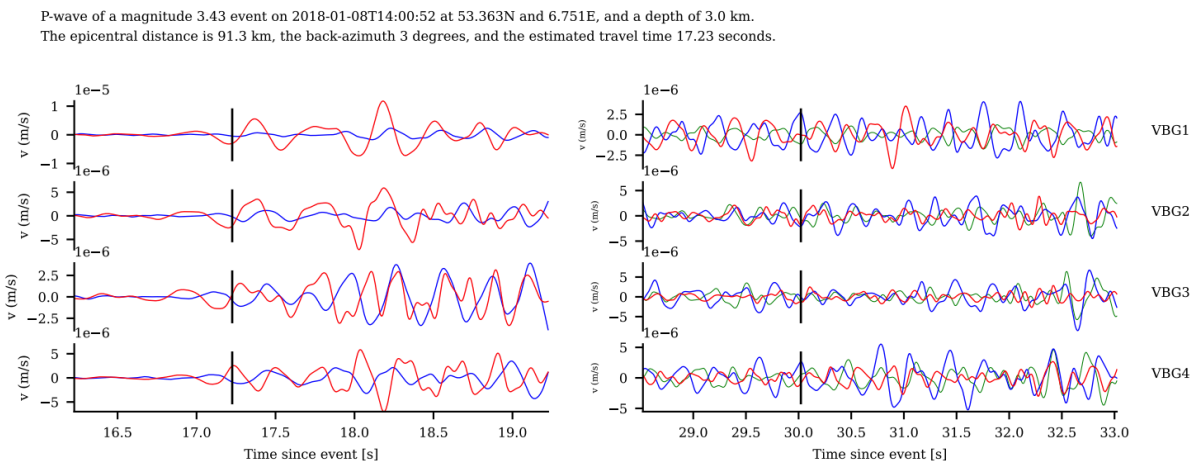

Figure 4.19: *Direct P-wave (left) and direct S-wave (right) at station VBG of a (relatively) nearby induced event in the north of the Netherlands during the third epoch; event details are provided at the top of the figure. For an explanation of the colors, we refer to the caption of Figure 4.7.*

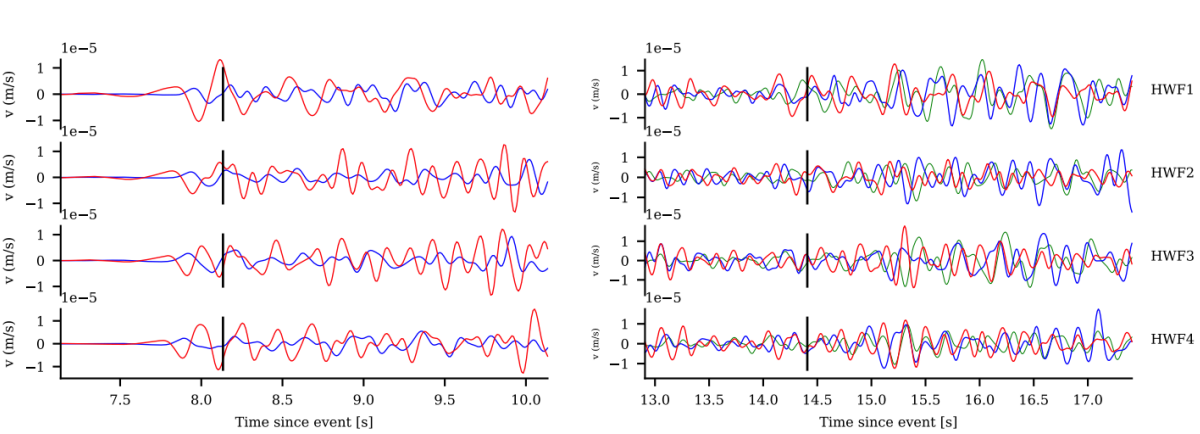

Figure 4.20: *Direct P-wave (left) and direct S-wave (right) at station HWF of a (relatively) nearby induced event in the north of the Netherlands during the second epoch; event details are provided at the top of the figure. For an explanation of the colors, we refer to the caption of Figure 4.7.*

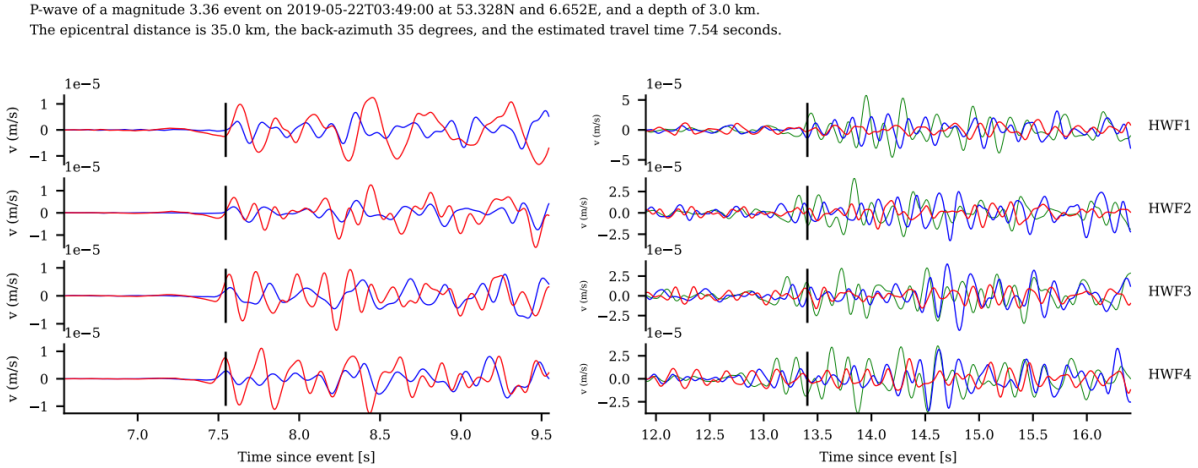

Figure 4.21: *Direct P-wave (left) and direct S-wave (right) at station HWF of a (relatively) nearby induced event in the north of the Netherlands during the third epoch; event details are provided at the top of the figure. For an explanation of the colors, we refer to the caption of Figure 4.7.*

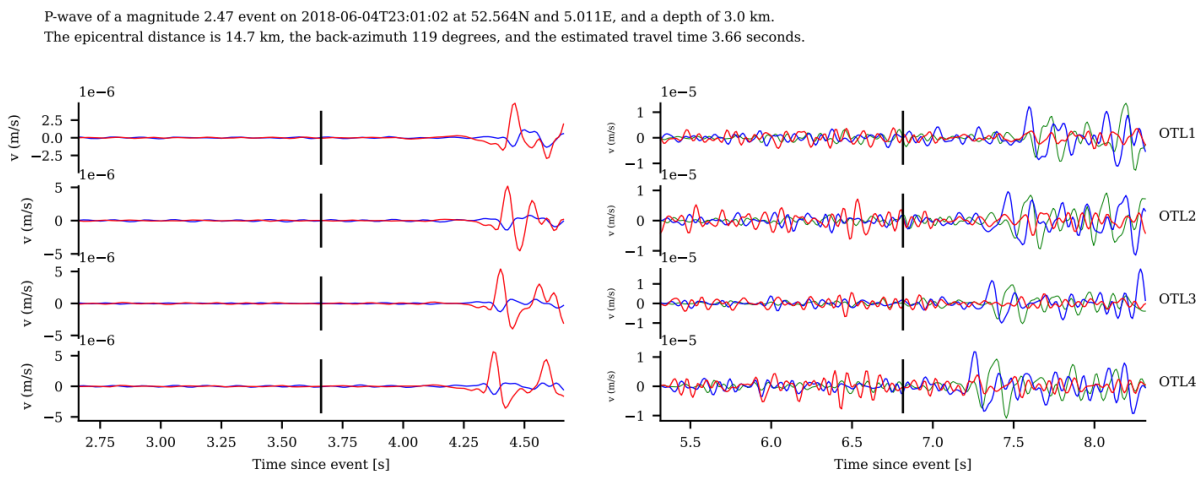

Figure 4.22: *Direct P-wave (left) and direct S-wave (right) at station OTL of a (relatively) nearby induced event in the north of the Netherlands during the third epoch; event details are provided at the top of the figure. For an explanation of the colors, we refer to the caption of Figure 4.7.*

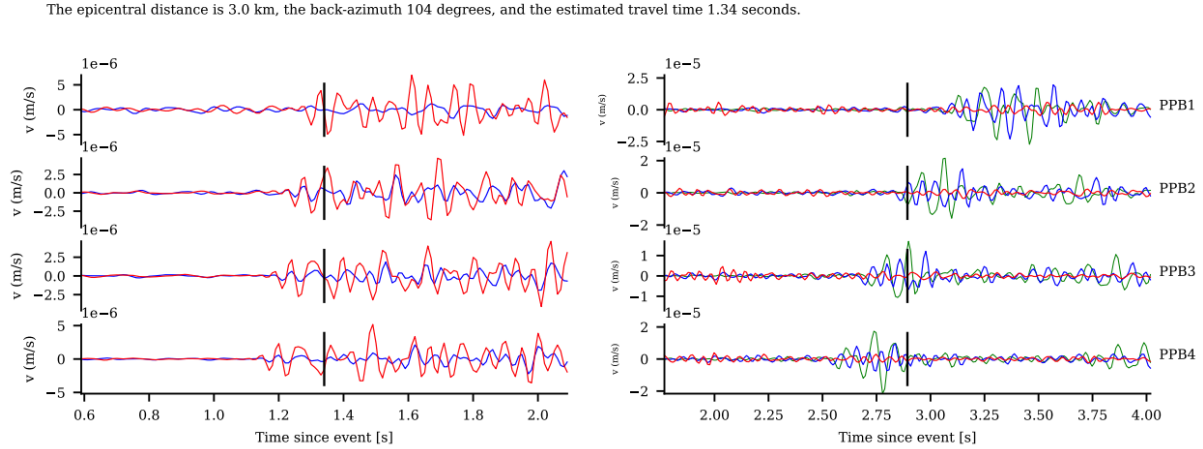

Figure 4.23: *Direct P-wave (left) and direct S-wave (right) at station PPB of a (relatively) nearby induced event in the north of the Netherlands during the second epoch; event details are provided at the top of the figure. For an explanation of the colors, we refer to the caption of Figure 4.7.*

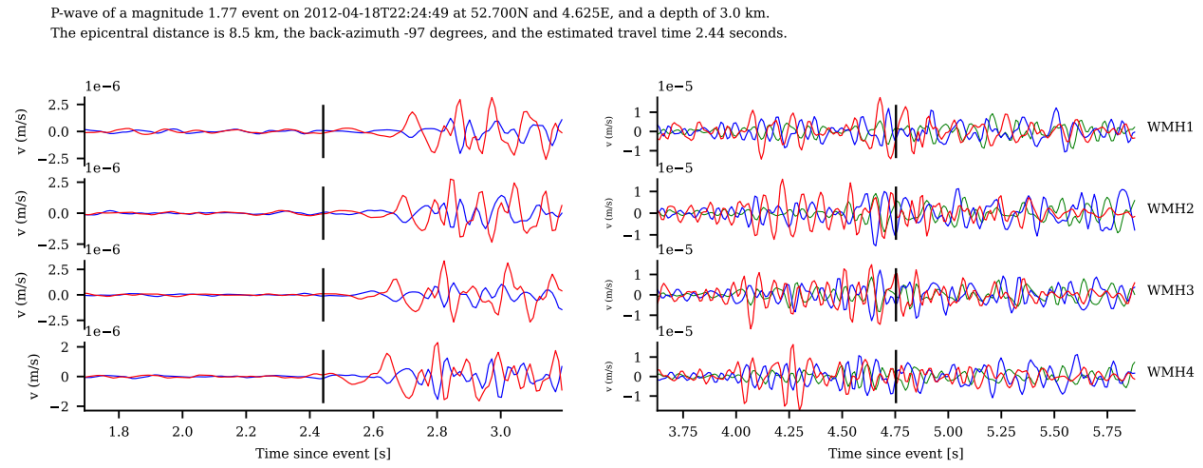

Figure 4.24: *Direct P-wave (left) and direct S-wave (right) at station WMH of a (relatively) nearby induced event in the north of the Netherlands during the second epoch; event details are provided at the top of the figure. For an explanation of the colors, we refer to the caption of Figure 4.7.*

4.3 Amplitudes

In this section, we focus on the amplitudes and spectral content of the borehole stations. The objective is to identify series of corrupted data that should be removed from our archive. We use a number of methods, measurables and visualizations for this purpose. First we compute, separately for each borehole station, the mean absolute amplitude of an individual channel's recording normalized with respect to the average over all geophones (for that channel). Second, we inspect the spectograms routinely computed as part of KNMI's suite of quality control tools. Third, we evaluate P and S-wave arrivals of nearby induced events (if any). We now first report, in detail, the parameters (and their values) that pertain to each of these three techniques; we use station FSW to showcase the application of the three techniques. Subsequently, we detail the analysis of the other borehole stations and discuss the implications for our data archive.

A first means to evaluate data quality relies on the (presumed) stability of a channel's recording in terms of amplitude. This stability is effectively assessed by computing, as a function of time and for each borehole station separately, the geophone and channel-specific mean absolute amplitude, and subsequently normalizing this mean absolute amplitude with respect to that channel's mean absolute amplitude averaged over all geophones. Due to computational constraints, we restrict our analysis to noise recorded between 03:00 and 03:30 UTC at regular intervals of two weeks. These recordings are demeaned, tapered and have their instrument response removed to recover the Earth's particle velocity at their respective depth level. Prior to the removal of the instrument response, overlapping samples are merged and gaps filled using the procedure described in Section 4.1. This ensures the artefacts shown in the same section do not arise. Furthermore, a (frequency-domain) pre-filter is applied in the process of removing the instrument response. As such, only signal between 5.0 and 40.0 Hz is retained. A cosine taper is applied between 2.5 and 5.0 Hz, and 40.0 and 50.0 Hz, on the low and high ends, respectively. The 5-40 Hz frequency band was chosen because it is adopted in most of our operational chains: a high SNR may be expected between 5 and 40 Hz for local and regional seismicity (Ruigrok et al., 2023).

Second, we inspect, for each channel of each geophone of each borehole station (210 channels in total) separately, the 14-year long spectogram. Effectively, these spectograms are an aggregate of the power spectral densities (PSDs) routinely computed as part of KNMI's suite of quality control tools. These PSDs can be accessed through an Application Programming Interface (API), and their computation is described in detail in Koymans et al. (2021). We only display the PSDs between 0.1 and 20 Hz. To somewhat limit the size of this report, we chose not to include all inspected spectograms, but merely provide an example. All spectograms can be found in the repository accompanying this report (Weemstra & Ruigrok, 2026). One general conclusion can be drawn from these spectograms: the replacement of the old acquisition setup (including the shaping filter to move the corner frequency to 1 Hz) with the Kinemetrics dataloggers effectively resulted in an increase of low frequency noise. Apparently, the pre-amplification of the lower frequencies allowed for a higher-fidelity (digital) registration of the wavefield below 1 Hz.

The third means to assess data quality constitutes the recordings of nearby induced events. The analysis is performed separately for each borehole station, and for both P and S waves. The P-wave arrivals are used to assess the data quality of the vertical components, whereas the S-wave arrivals are used to evaluate the recordings on the horizontal channels. For consecutive periods of three months, and for P and S arrivals separately, we select that event from our catalog, whose arrival has the highest SNR. Note that some borehole stations did not have an induced event occurring nearby for every three-month period. In fact, our catalog does not contain any induced events close to the three stations in western Friesland (WYN, ZWE, and FDG), rendering the assessment of data quality using the recordings of induced earthquakes impossible for those stations. The amplitude of the signal is defined as the maximum absolute amplitude in the signal window. The signal window has a length of 1.5 seconds for the P-wave and 3 seconds for the S-wave, both centered around the mean expected arrival time. The latter being computed based on the (simple) polynomial travel time models described in Section 2.6.1 of Ruigrok et al. (2023). The noise amplitude is defined as the root-mean-square of the 60 second long recording prior to the arrival of the P-wave. For all borehole stations, selected P and S-wave arrivals can be found in the repository accompanying this report (Weemstra & Ruigrok, 2026).

Based on the three just described techniques, we now assess the quality of the recordings of all borehole

stations. We do this for each borehole station separately, with the (presumed) stability of a channel's recording in terms of amplitude being leading. The other two techniques are used to yield more insight or merely confirm observations. Only for station FSW we therefore show a few spectograms (Figure 4.26) and examples of recordings of P- and S-wave arrivals of nearby induced events; All spectograms and recordings of nearby induced events can be found in the repository accompanying this report (Weemstra & Ruigrok, 2026). Frequently, we also show individual (noise) recordings to aid the assessment or identify the cause of the observed data degeneration. Series of corrupted data, which have been removed from our archive, are specified in Table 4.9.

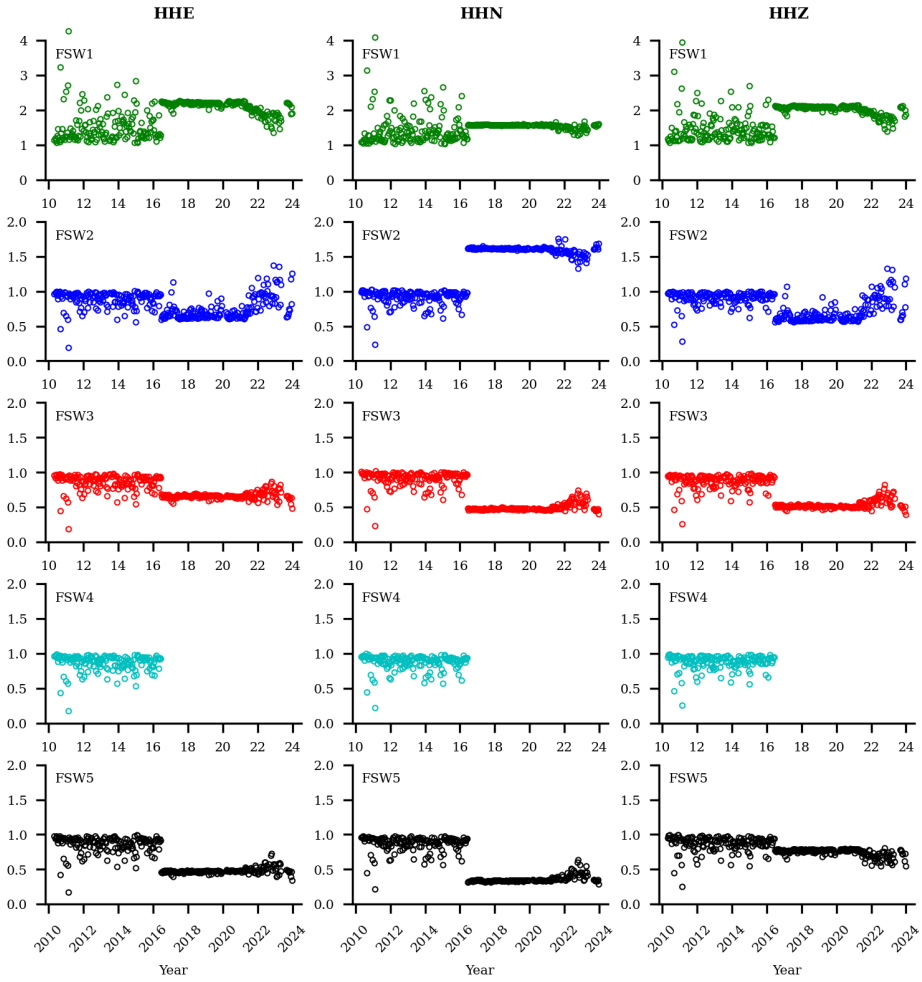

Figure 4.25: *Mean absolute amplitude of 30-minute noise recordings by individual borehole channels of FSW, normalized with respect to this channel's mean absolute amplitude averaged over all borehole levels.*

Series of normalized mean absolute amplitudes of borehole station **FSW** are shown in Figure 4.25. During the second epoch, we do not observe trends that suggest the presence of systematic noise or artifacts. Since, contrary to the shallowest geophone of the other borehole stations, geophone FSW1 is located at the surface, its recordings occasionally have particularly high amplitudes. We attribute this to either (transient) anthropogenic noise or wind-driven seismic seismic noise generated in the proximity of the borehole. In general, the amplitudes by geophone FSW1 are relatively high due to its presence at the surface. Coinciding with the change of the datalogger (2016-06-14; see Table 3.1), all four remaining geophones (geophone FSW4 is discontinued at this moment in time) start to exhibit anomalously low or high amplitudes; even after removal of the instrument response and application of the aforementioned frequency-domain pre-filter (signal between 5.0 and 40.0 Hz is retained).

In Figure 4.26, the spectograms of the HHZ recordings by FSW5 are shown for 2015 (top) and 2017 (bottom). It clearly shows the absence of signal in the recordings of this geophone during the third epoch. In an attempt to understand the deterioration of the recordings by FSW at the time of the

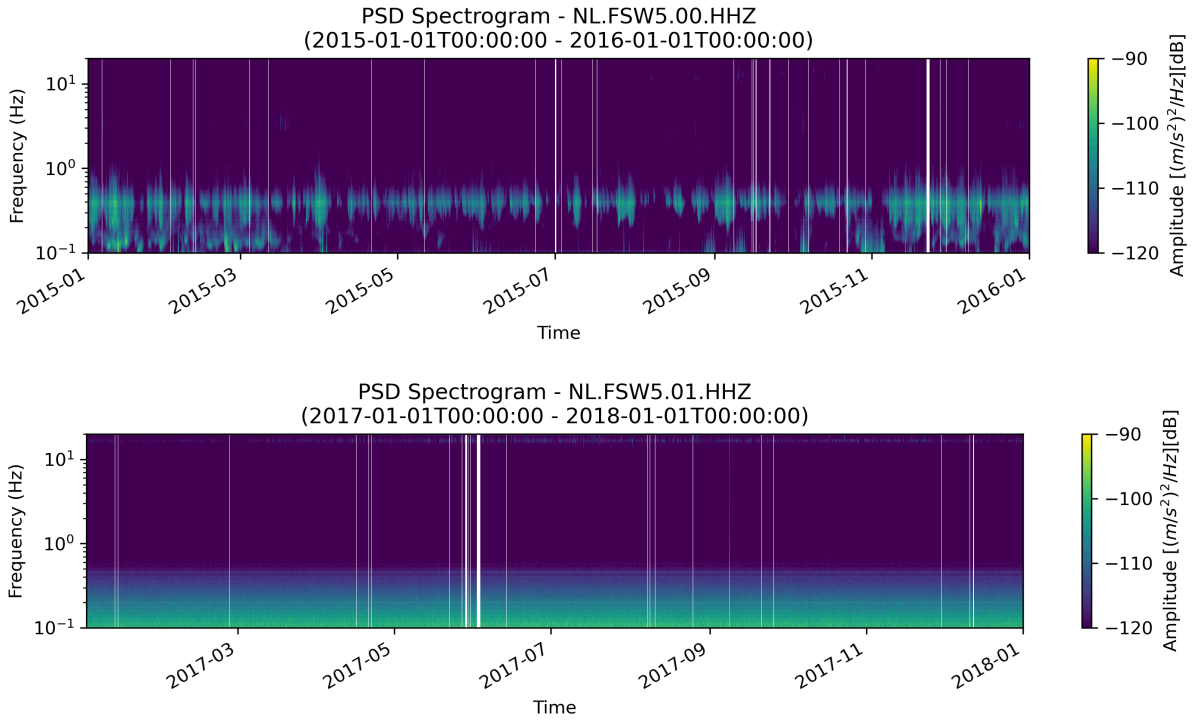

Figure 4.26: *Spectograms of the recordings by channel HHZ of geophone FSW5 for 2015 (top) and 2017 (bottom).*

change of datalogger (start of the third epoch), a number of site visits were undertaken. Eventually, this revealed an inconsistency in the wiring. In the shunt-box, which was designed to effectuate the desired damping, the plus and minus wire of the same channel were not connected to the correct pair of wires of the datalogger. This applied to all channels. Some wires leaving the geophone cable were in fact not connected at all. The miswiring resulted in practice in archived recordings being the result of a combination of the plus of a channel at one depth level and the minus of another channel at another depth level (i.e., another geophone). The field observation is confirmed by the poor fidelity of the spectograms, the teleseismic events and induced events published on the KNMI Data Platform (Weemstra & Ruigrok, 2026).

Occasionally, recordings of nearby strong induced events appear to have been recovered (see Figure 4.27). Due to the miswiring, however, these recordings do not represent the true particle velocity of a specific component of a specific geophone. They are merely the result of combining the plus wire of one channel with the minus wire of another channel. This also explains why their quality is generally rather low (low SNR and poor timing) and varies from one geophone to the other. Figure 4.28 shows the archived HHZ recordings of two induced events: an event that occurred during the second epoch (left) and an event that occurred during the third epoch (right).

Figures 4.27 and 4.28 do not only showcase the low fidelity of the recordings during the third epoch. They also reveal that the archived recordings suffer severely from the presence of the well-known 50 Hz grid distortion. This applies to all archived recordings of station FSW during the third epoch. This is exemplified in Figure 4.29 for the recordings on channel HHZ.

In conclusion, the combination of the miswiring and the 50 Hz grid distortion renders all third epoch recordings by station FSW useless. Consequently, the third epoch's recordings by FSW have been deleted from our archive. Importantly, none of the events in KNMI's public earthquake catalog which have occurred during the third epoch, contain either a pick or magnitude estimate by one of the geophones of borehole station FSW.

Series of normalized mean absolute amplitudes of borehole station **ENM** are shown in Figure 4.30. The relative mean absolute amplitude of channel HHE of the shallowest geophone (it is around 1) is lower

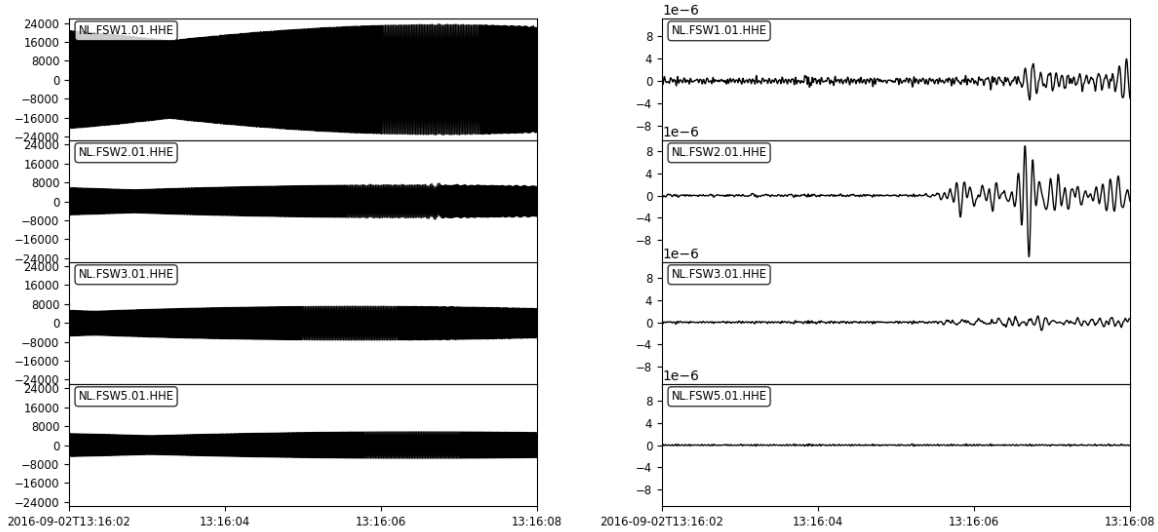

Figure 4.27: *Left: raw HHE recordings (vertical axis has units 'counts') for a period of six seconds, which include the response to a M_l 2.1 event at an epicentral distance of 18 km (event estimated to have occurred at 2016-09-02T13:16:00.90). Right: same six seconds after removal of the instrument response in conjunction with a 5-40 Hz frequency-domain band-pass pre-filter (particle velocity; vertical axis has units 'm/s') on channel HHE of (all geophones of) borehole station FSW. Both on the left and right side, the traces have coinciding scales.*

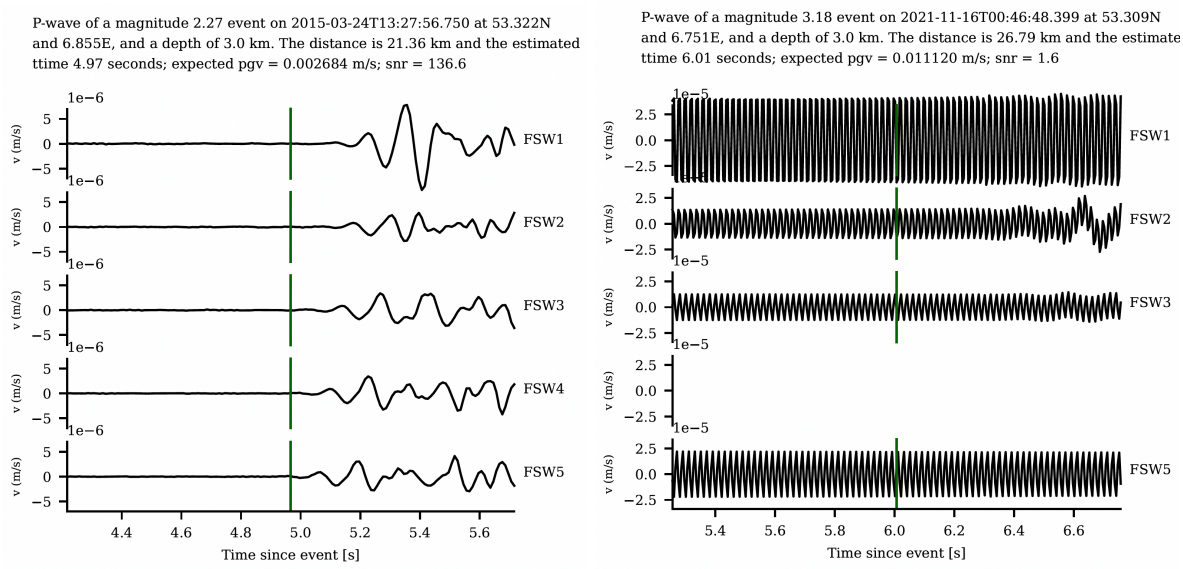

Figure 4.28: *Recordings by channel HHZ by all FSW geophones as they are present in our archive for an event prior (left) and after (right) the change of the datalogger. The left traces are the due to a magnitude 2.27 induced event on 2015-03-24 at an epicentral distance of 21.4 km. The right traces show some weak undulations due to a magnitude 3.18 induced event on 2021-11-16 at an epicentral distance of 26.8 km. Both on the left and right side, the traces have coinciding scales.*

than one would expect. Closer inspection reveals that this geophone's HHE channel appears to suffer from the 50 Hz grid distortion. Starting from the 29th of March 2015, this also applies to channel HHE of geophone ENM3. We could not identify the source of its sudden introduction on that date. The fact that it did not coincide with a change of datalogger, however, leads us to believe that it is geophone specific. At the same time, the other two channels of the same geophone appear to be unaffected. For both ENM1 and ENM3, the presence of the 50 Hz distortion is confirmed by the raw recordings of a nearby induced event (Figure 4.31). Unfortunately, the distortion corrupts the signal that much, that it effectively renders the HHE recordings by geophones ENM1 and ENM3 useless. That is, removal of

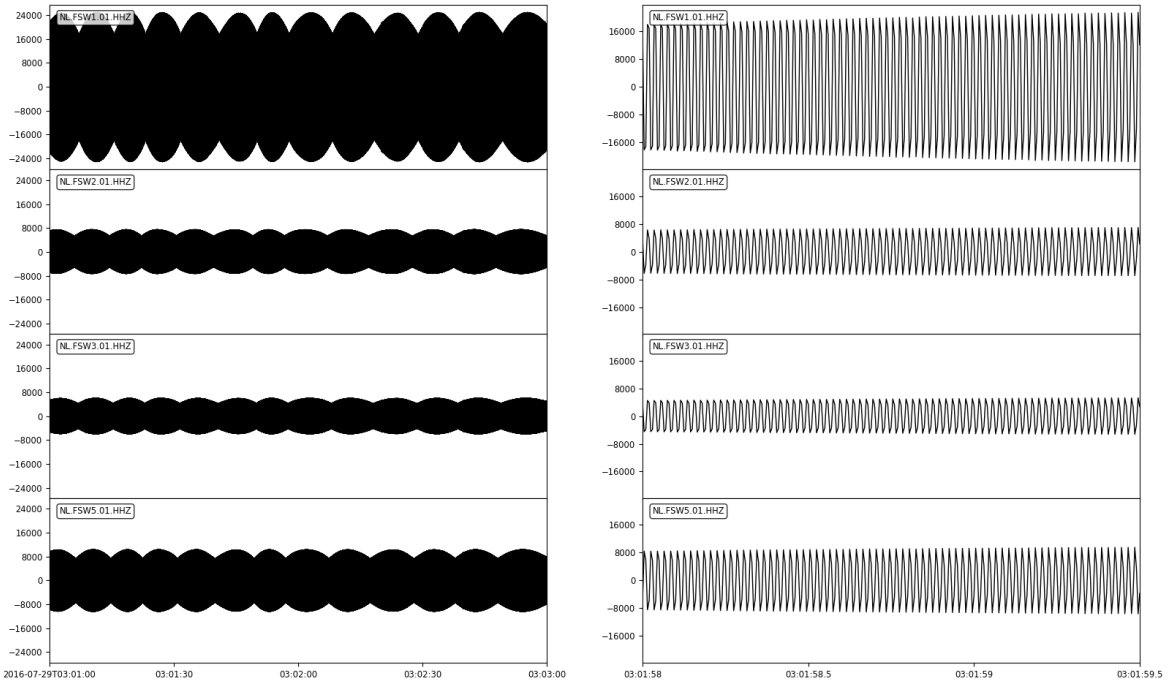

Figure 4.29: *Raw HHZ recordings (vertical axis has units 'counts') starting on 03:01:00 at 2016-7-29 of (all geophones of) borehole station FSW. The traces on the left have a length of two minutes, whereas the traces on the right have a length of 1.5 seconds (from 03:01:58 till 03:01:59.5). Both on the left and right side, the scale coincides for all geophones. The traces on the right clearly reveal the presence of the 50 Hz grid distortion.*

the instrument response in conjunction with the frequency-domain 5-40 HZ pre-filter does not allow the induced event's response to be recovered (see Figure 4.32).

Coinciding with the change of the datalogger (2016-05-04 for station ENM), both channel HHN and HHZ start to also contain significant 50 Hz noise (see Figure 4.33). This applies to all geophones. For channel HHZ, application of the pre-filter and removal of the instrument response effectively removes the monochromatic signal for all geophones. This implies high fidelity recordings of induced events can still be recovered. This is not the case for recordings by channel HHN of geophone ENM2. Signal from nearby induced events cannot be observed after application of the pre-filter and removal of the instrument response. Consequently, the third epoch's HHN recordings of ENM2 can be deleted from our archive. Signal of induced events can be recovered from the HHN recordings of the other three geophones. A site visit to station ENM lead us to conclude that the circuit was broken for all three channels (ENM1: HHE, ENM2: HHN, ENM3: HHE), as their resistance read infinity at the surface.

The normalized mean absolute amplitudes of borehole station **WDB** are shown in Figure 4.34. Up to the moment the datalogger has been changed (2016-06-14 for station WDB), amplitudes appear to be fairly stable for all components of all geophones. Closer inspection, however, reveals that recordings by channel HHZ and HHN of WDB3 contain only noise (see also the spectograms, teleseismic events, and induced events published on the KNMI Data Platform (Weemstra & Ruigrok, 2026)). In addition, the recordings by HHE deteriorate rapidly immediately after the start of the continuous data acquisition. In fact, even the first induced recorded events by WDB3's HHE channel are too noisy to yield reliable readings. Interestingly, the amplitude of the (recorded?) noise varies in sync with the amplitude of the noise on the other components and geophones. We did not further investigate why this is the case. In any case, the continuous recordings by WDB3 can be deleted from our archive. Note that none of the events in KNMI's public earthquake catalog which have occurred during the continuous acquisition period, contain either a pick or magnitude estimate based on the recordings by WDB3.

The change of the datalogger (2016-06-14 for station WDB) coincides with a "discontinuity" in the relative mean absolute amplitudes. The HHZ component's data, in particular, is affected. This is due to

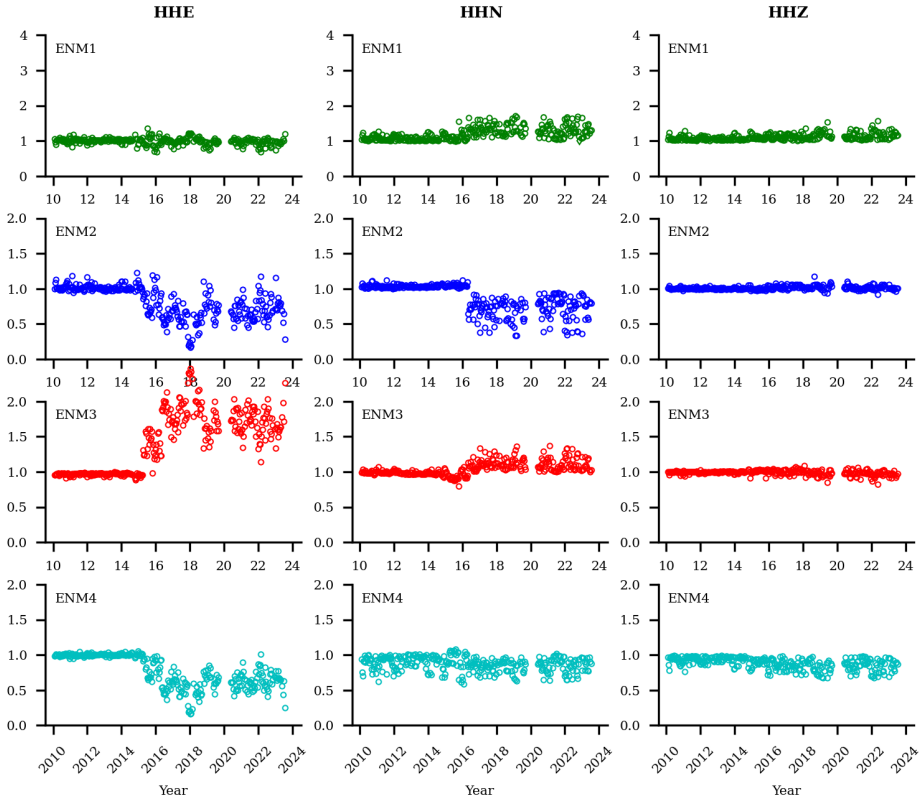

Figure 4.30: *Mean absolute amplitude of 30-minute noise recordings by individual borehole channels of ENM, normalized with respect to this channel's mean absolute amplitude averaged over all borehole levels.*

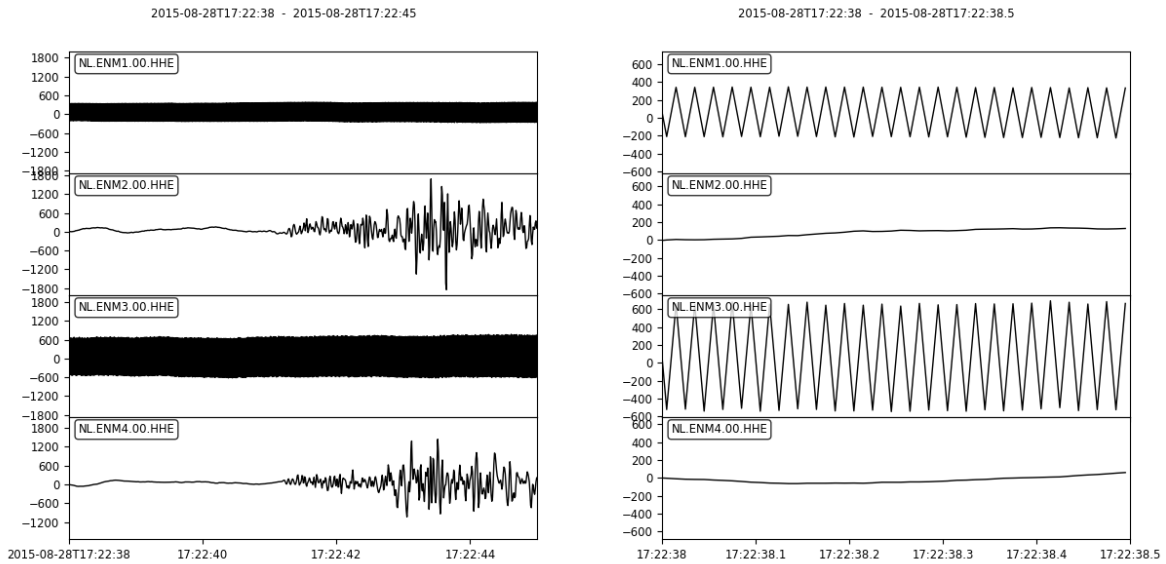

Figure 4.31: *Raw recordings (vertical axis has units 'counts') on channel HHE of (all geophones of) borehole station ENM. The traces on the left have a length of seven seconds, and include the response to a M_l 1.3 event at an epicentral distance of 7 km. The scale coincides for all geophones. For ENM1 and ENM3, the response to the induced event is completely overwhelmed by the 50 Hz grid distortion. That we are dealing with this type of distortion becomes particularly clear from the zooms on the first 0.5 second of the raw recordings (right side).*

a jump of the absolute amplitude of WDB1. Closer inspection reveals that this geophone's HHZ channel

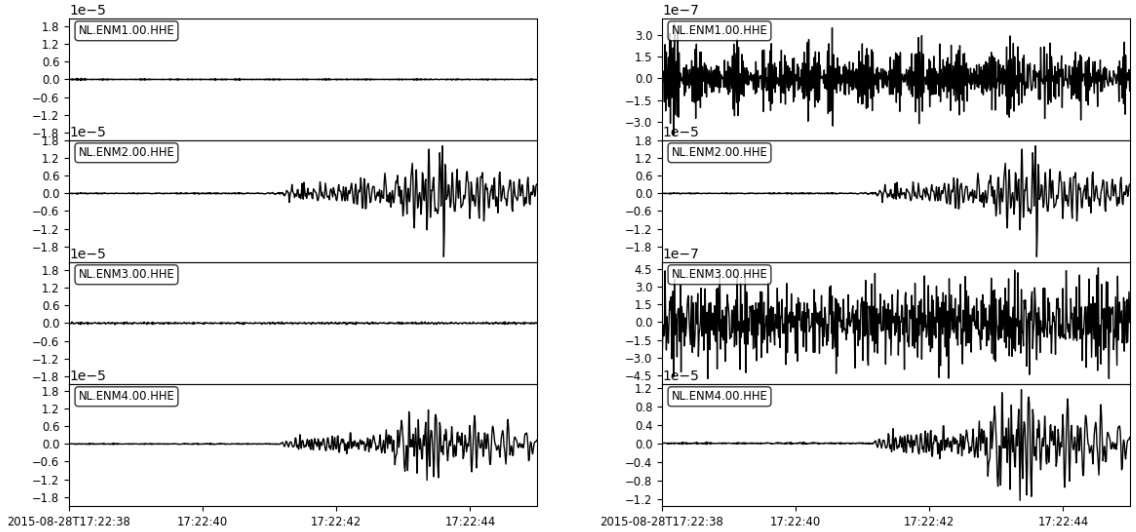

Figure 4.32: *Seven seconds of particle velocity (vertical axis has units 'm/s') on channel HHE of (all geophones of) borehole station ENM. These traces result from the removal of the instrument response in conjunction with a 5-40 Hz frequency-domain band-pass pre-filter. The traces on the left have coinciding scale, while the traces on the right have been normalized individually.*

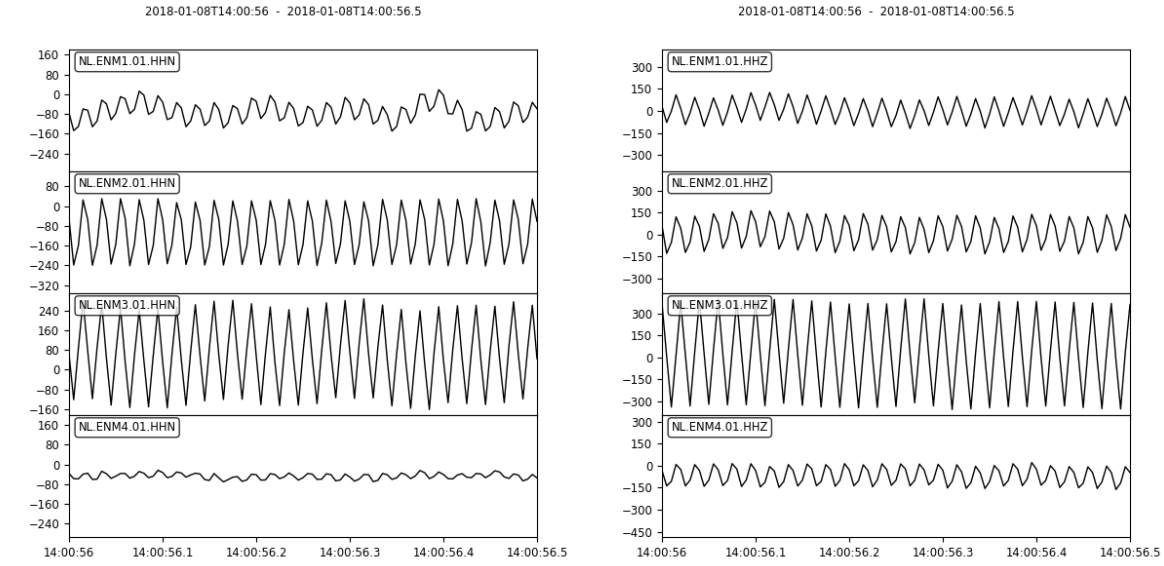

Figure 4.33: *Four seconds of raw recordings (vertical axis has units 'counts') on channel HHN (left) and HHZ (right) of borehole station ENM. The scale coincides for all geophones. On all geophones, both channels contain the typical 50 Hz noise, albeit with different amplitudes.*

starts to suffer severely from the 50 Hz grid distortion. This is confirmed by the spectograms, teleseismic events, and induced events published on the KNMI Data Platform (Weemstra & Ruigrok, 2026). The continuous HHZ recordings of WDB1 during the third epoch can hence be deleted from our archive. Note that none of the events in KNMI's public earthquake catalog which have occurred during the third epoch, contain either a pick or magnitude estimate based on the recordings by WDB1. In addition to WDB1, also the HHZ component of WDB4 contains some 50 Hz (grid) noise (see the plots of the induced events on the KNMI Data Platform (Weemstra & Ruigrok, 2026)). This geophone's HHZ component's data is fortunately only very slightly affected.

The normalized mean absolute amplitudes of borehole station **ZLV** are shown in Figure 4.35. At this station, the third epoch starts at the 15th of June 2016 (see Table 3.1). The acquisition of the data

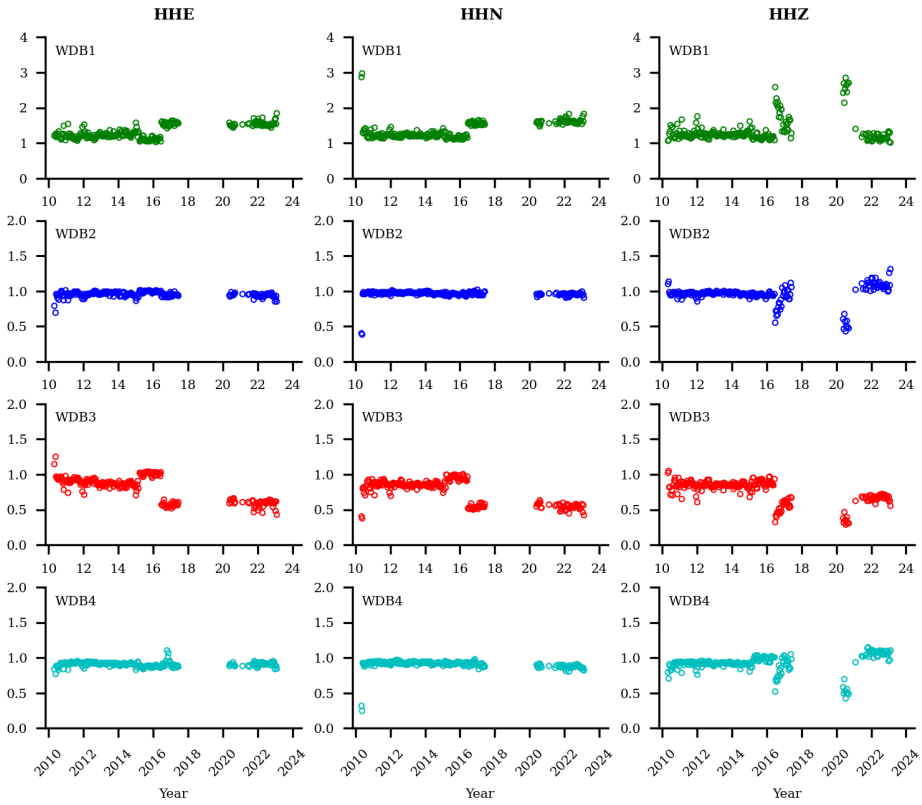

Figure 4.34: *Mean absolute amplitude of 30-minute noise recordings by individual borehole channels of WDB, normalized with respect to this channel's mean absolute amplitude averaged over all borehole levels.*

recorded by geophone ZLV0 was discontinued at this point in time. Inspections of the spectograms of this geophone reveal that the recordings by channel HHE did not record surface ground motion except for two brief periods (Weemstra & Ruigrok, 2026). These two periods are 2011-08-22 to 2011-10-06 and 2012-03-01 to 2012-03-26. We did not further investigate why, outside of these two relatively (seemingly arbitrary) short spells, this channel did not provide any ground motions. Note that the recordings of the selected induced events confirm this observation (Weemstra & Ruigrok, 2026). Similar to HHE, also the spectograms of the recordings by channel HHN reveal long periods for which no ground motions were recorded. These are also listed in Table 4.9, and also confirmed by the recordings of the selected induced events (Weemstra & Ruigrok, 2026). ZLV0's HHZ channel generated more high-fidelity recordings, but nonetheless contains two periods during which no surface vibrations have been recorded. In addition to the selected induced events, the recordings of the selected teleseismic events confirm this observation (i.e., the ones that were used to check the vertical polarities; Weemstra & Ruigrok, 2026).

Starting from the end of December 2022, the recordings by channel HHZ of geophone ZLV1 abruptly display a severe 50 Hz grid distortion. To some extent, this is visible in the normalized mean absolute amplitudes of this channel (right column of Figure 4.35). It is, however, more clear from the spectograms, the recordings of the selected induced events, and the recorded teleseismic phases (Weemstra & Ruigrok, 2026). We therefore indicated in Table 4.9 that, starting from the end of December 2022, the data recorded by this channel can be deleted from our archive. Starting from mid August 2017, recordings by channel HHN of geophone ZLV4 deteriorate abruptly. Rather powerful high-frequency monochromatic noise (50 Hz grid noise?) dominates its recordings since then, effectively rendering these useless. This is clearly apparent from the relative mean absolute amplitudes in Figure 4.35, but also from the other observables (Weemstra & Ruigrok, 2026).

The normalized mean absolute amplitudes of borehole station **ZL2** are shown in Figure 4.36. The third epoch of this station starts at the 15th of June 2014 (datalogger replacement; see Table 3.1) and runs till the beginning of 2018 only, after which ZL2 was dismantled. Amplitudes appear to be fairly stable for all components of all geophones, but, just as for the already discussed borehole stations, a jump is observed

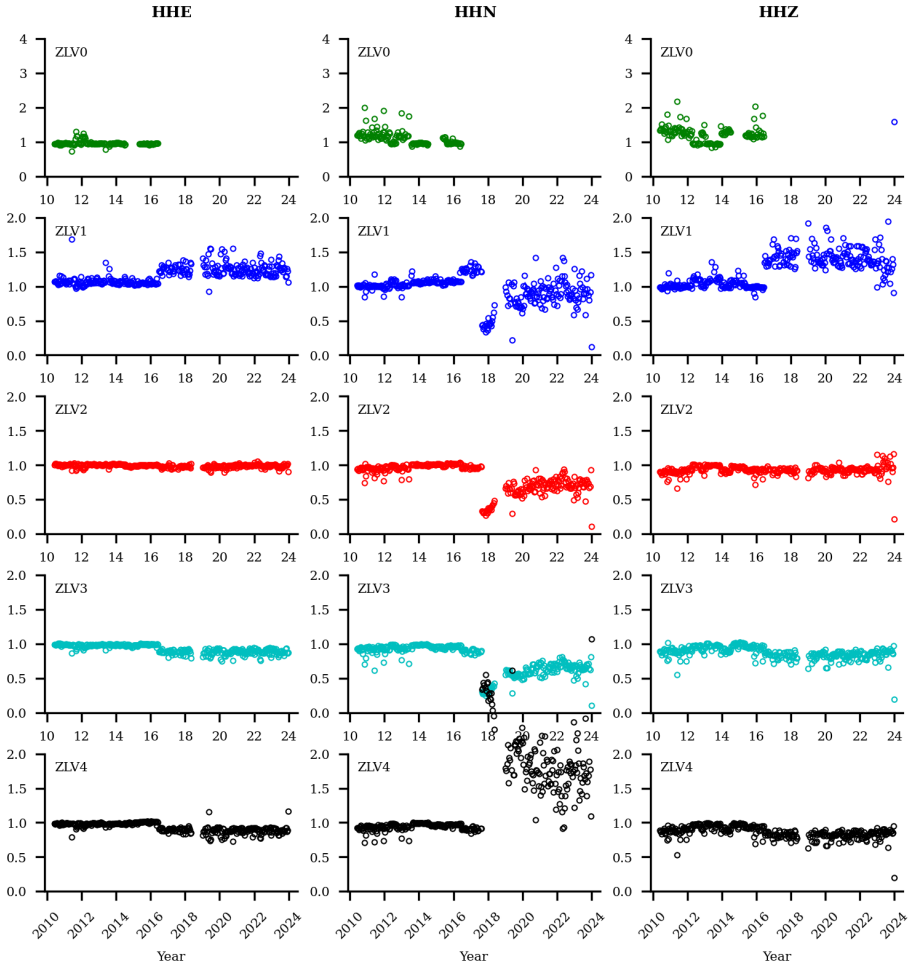

Figure 4.35: *Mean absolute amplitude of 30-minute noise recordings by individual borehole channels of ZLV, normalized with respect to this channel's mean absolute amplitude averaged over all borehole levels.*

at the moment the datalogger is replaced. Prior to this date, the relative mean absolute amplitudes of the shallowest geophones are lower than one would expect and those of the deepest geophones higher than one would expect. One typically expects the amplitudes in the 5-40 Hz frequency band to increase towards the surface due to a combination of the free-surface effect and amplification. Since many of the borehole stations do show this (expected) amplification during the third epoch, we delve a bit deeper into this.

The instrument responses of the borehole recordings are removed by means of a deconvolution applied in the frequency domain. In this section this deconvolution is paired with a 5-40 Hz pre-filter, including cosine tapers between 2.5 and 5.0 Hz, and 40.0 and 50.0 Hz on the low and high ends, respectively. Effectively, therefore, no signal below 2.5 Hz and above 50 Hz should be present in the data. The noise recordings recovered prior to the change of the datalogger appear to be subject to less amplification towards the surface. Clearly, this cannot be: neither the subsurface nor the nature of the wavefield will have changed at that point in time. To gain some more insight, we also computed (i) the normalized mean absolute amplitudes while applying a pre-filter between 5 and 20 Hz in the response deconvolution process (and a cosine taper on the high end between 20 and 40 Hz) and (ii) the normalized mean absolute amplitudes while applying a pre-filter between 10 and 40 Hz in this process (and a cosine taper on the low end between 5 and 10 Hz). These are both shown in Figure 4.37.

First, we observe that the amplification increases with decreasing frequency. That is, compared to the 5-40 Hz frequency band, the amplification towards the surface increases for noise recordings between 5 and 20 Hz. Conversely, the amplification towards the Earth's surface decreases for noise between 10 and 40 Hz. This trend applies to all channels and for both epochs.

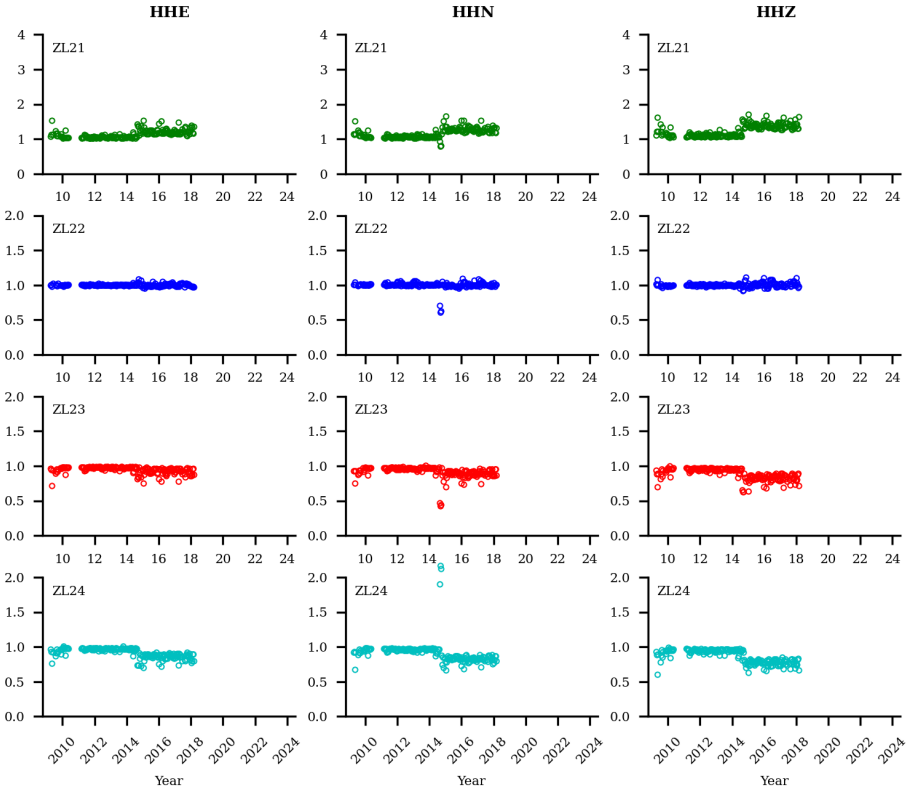

Figure 4.36: *Mean absolute amplitude of 30-minute noise recordings by individual borehole channels of ZL2, normalized with respect to this channel's mean absolute amplitude averaged over all borehole levels.*

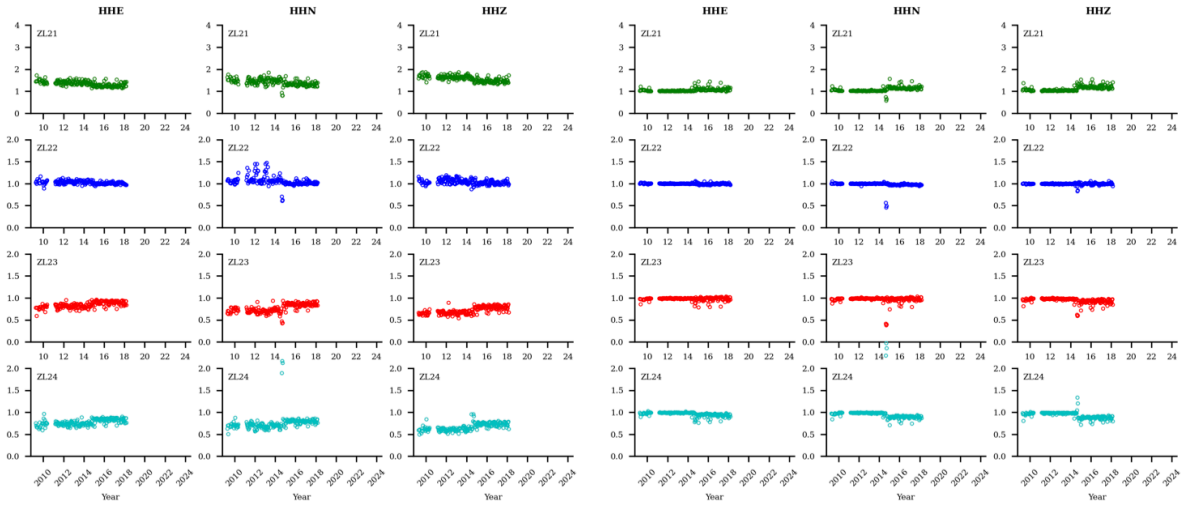

Figure 4.37: *Left: Same as Figure 4.36, but in this case the normalized mean absolute amplitudes were computed after applying a pre-filter between 5 and 20 Hz in the response deconvolution process (and a cosine taper on the high end between 20 and 40 Hz). Right: Same as Figure 4.36, but with the normalized mean absolute amplitudes computed after applying a pre-filter between 10 and 40 Hz in the response deconvolution process (and a cosine taper on the low end between 5 and 10 Hz).*

Second, compared to the 5-40 Hz frequency band, the observed increase in amplification between 5 and 20 Hz is higher during the second epoch than during the third epoch. A change of the recordings' spectral content due to the overhaul of the acquisition system marking the start of the third epoch can explain this. A combination of the analog high-pass, shaping, and anti-alias filters implies that the analog amplitude response during the second epoch is not flat between 2.5 and 50 Hz. Instead, Figure 3.2 shows

that the analog amplitude response has a lower corner frequency of 1 Hz, exhibits a bulge around 4.5 Hz, and has a higher corner frequency of 28 Hz during this epoch (Dost & Haak, 2002). Consequently, the observed increase in amplification at the surface for the 5-20 Hz frequency band (compared to the 5-40 Hz frequency band) merely appears to be higher during the second epoch. It can be attributed to the fact that the removal of the instrument response in the 5 to 40 Hz frequency band during the second epoch (partly) boosts datalogger noise above, approximately, 28 Hz. This amplification of datalogger noise will become most severe towards 50 Hz. Since the amplitude of this boosted signal will be the same for all depth levels, the true wavefield amplification towards the surface is partly masked. In other words, the amplification in Figure 4.36 is underestimated during the second epoch. This is not the case during the third epoch, as the corner frequency of the analog amplitude response during this epoch is 4.5 Hz (coinciding with the geophone's corner frequency; see Figure 3.3), and is flat beyond approximately 10 Hz. Note that the difference in overall instrument response between the two epochs is shown in Figure 3.1.

What remains unclear, however, is why in the 5-20 Hz band the amplification appears to be slightly higher during the second epoch than during the third epoch (Figure 4.37; left). Or, alternatively, why the amplification in this frequency band appears to be slightly lower during the third epoch. It might be due to overall elevated datalogger noise levels in the third epoch masking part of the actual wavefield amplification or some other unknown acquisition-related phenomenon. It is beyond the scope of this study to investigate this in more detail.

The normalized mean absolute amplitudes of borehole station **ENV** are shown in Figure 4.38. At this station, the third epoch starts at the 16th of June 2016 (see Table 3.1). In general, the quality of the recordings deteriorates towards the end of the third epoch. Most recorded events, however, still have sufficiently high SNRs to be of use for seismological studies and/or event analysis. At the same time, there are numerous (shorter) periods for which this is not the case. These periods can clearly be identified from the spectograms. The first half a year after the start of the continuous data acquisition, for example, did not yield any useful data for most channels and most geophones. Also, the recordings by ENV4 did not yield (high-fidelity) wavefield recordings for approximately the last two years of the second epoch. Per geophone and channel, these periods are listed in Table 4.9.

The normalized mean absolute amplitudes of borehole station **VLW** are shown in Figure 4.39. Continuous acquisition at Vlagtwedde started on 2010-10-29, whereas the third epoch starts at the 15th of June 2016 (see Table 3.1). Immediately from the start of the continuous acquisition, channel HHN of VLW1 did not deliver horizontal particle velocity. This is immediately clear from the spectograms. Looking at the recordings of selected induced events (Weemstra & Ruigrok, 2026), this channel's recordings contain powerfull glitches at regular intervals of about 1 seconds starting from mid 2014. This lasts until the moment the datalogger is replaced, after which the glitches are replaced by strong monochromatic noise. All in all, this leads to the conclusion that the continuous data recorded by VLW1's HHN channel can be deleted from our archive.

Channel HHN of geophone VLW2 correctly sampled the wavefield till mid 2022. From that moment onward, however, its recordings do not correctly represent horizontal particle velocity. This can be concluded from both the spectograms and its normalized mean absolute amplitudes (Figure 4.50, middle column). Starting from September 2014, the vertical component channel of this geophone barely delivered signal above 1 Hz. After the datalogger was replaced, this channel's data quality deteriorated even further. We did not investigate the cause of this deterioration. Channel HHN of geophone VLW3 functioned flawlessly until fall 2018. However, starting from the first of September that year it merely delivered noise. It is clear from Figure 4.39 that these noise recordings are in fact quite powerful. This figure also reveals that for a period of about one year (mid 2015 – mid 2016), channel HHE of geophone VLW4 generated anomalously high amplitudes. During this period, some instrument issue prevented the wavefield from being recorded (see also the spectograms). After the datalogger was replaced, its recordings are again of good quality. Finally, the HHZ recordings of this geophone do not allow the wavefield to be recovered for the entire continuous acquisition period. This is very clear from both Figure 4.39 (right column) and the spectograms. It is particularly evident from the comparison of the teleseismic events (see Weemstra & Ruigrok, 2026).

The normalized mean absolute amplitudes of borehole station **VBG** are shown in Figure 4.40. Continuous acquisition at VBG started on 2010-09-01, whereas the third epoch starts at the 16th of June

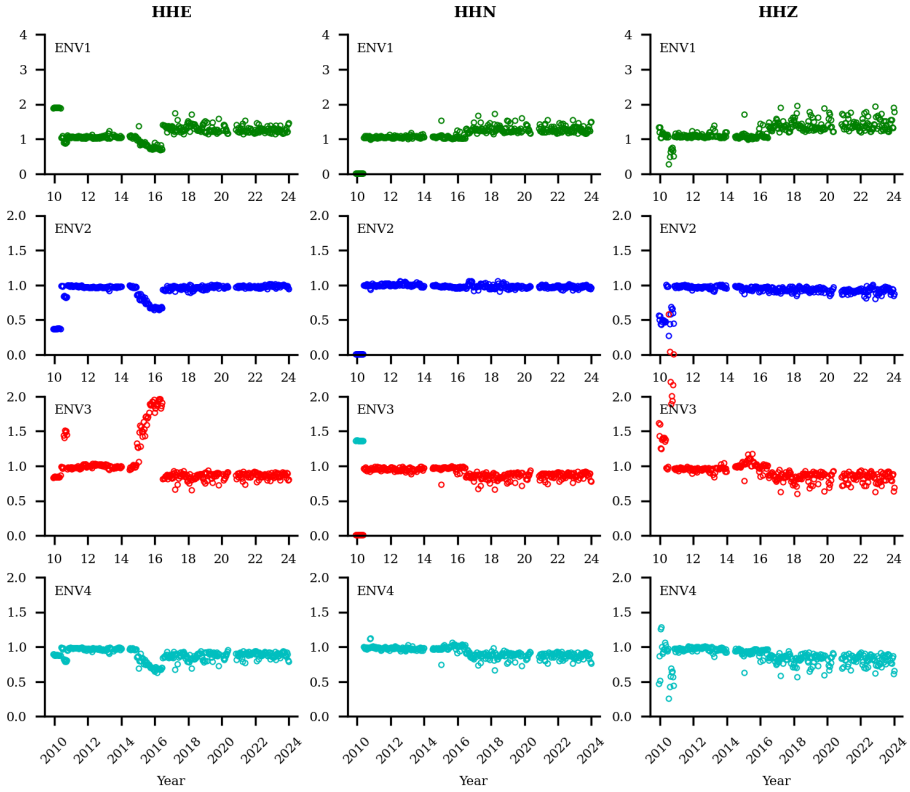

Figure 4.38: *Mean absolute amplitude of 30-minute noise recordings by individual borehole channels of ENV, normalized with respect to this channel's mean absolute amplitude averaged over all borehole levels.*

2016 (see Table 3.1). The only channel of this station that does not (and never did) deliver accurate continuous wavefield recordings is channel HHE of geophone VBG1. We do observe a relative amplitude "discontinuity" coinciding with the change of the datalogger. This can most likely be explained by amplified datalogger noise at frequencies beyond 28 Hz. Recall the discussion of the same discontinuity observed for station ZL2.

The normalized mean absolute amplitudes of borehole station **HWF** are shown in Figure 4.41. Continuous acquisition by HWF started on 2010-11-24, whereas the third epoch starts at the 13th of June 2016 (see Table 3.1). Channels HHN and HHZ start to generate pure (instrument) noise during 2020. For HHN this starts around the 20th of November of that year, whereas for HHZ this starts around the 10th of July. The effect on the amplitudes can be seen in Figure 4.41. The spectograms, selected induced events, and selected teleseismic events all reveal the sudden deterioration of these two channels. The other geophones do not show a (significant) decrease in data quality over the years.

The normalized mean absolute amplitudes of borehole station **OTL** are shown in Figure 4.42. Continuous acquisition by OTL started on 2010-10-11, whereas the third epoch started only at the second of July 2019 (see Table 3.1). Starting from the beginning of October 2014 channel HHN and HHE of both geophone OTL3 and OTL4 generated merely instrumental noise. This behavior ends at the beginning of June 2015. We did not investigate the cause. The fact that amplitudes are lower during this period is visible in Figure 4.42, but is more clear from the spectograms. Figure 4.43 shows the absence of the S waves generated by a Magnitude 7.2 event in Nepal on the HHE and HHN channels of OTL3 and OTL4. Note that amplitudes on channels bearing the same name may vary between the different geophones of a string due to the difference in azimuth of the horizontal channels of these geophones. The just described data corruption is also observed on channel HHZ of OTL4 for the period October 2014 to June 2015, but not on the same channel of OTL3 (see also the HHZ recordings of the teleseismic arrivals; Weemstra & Ruigrok, 2026).

The normalized mean absolute amplitudes of borehole station **PPB** are shown in Figure 4.44. Continuous

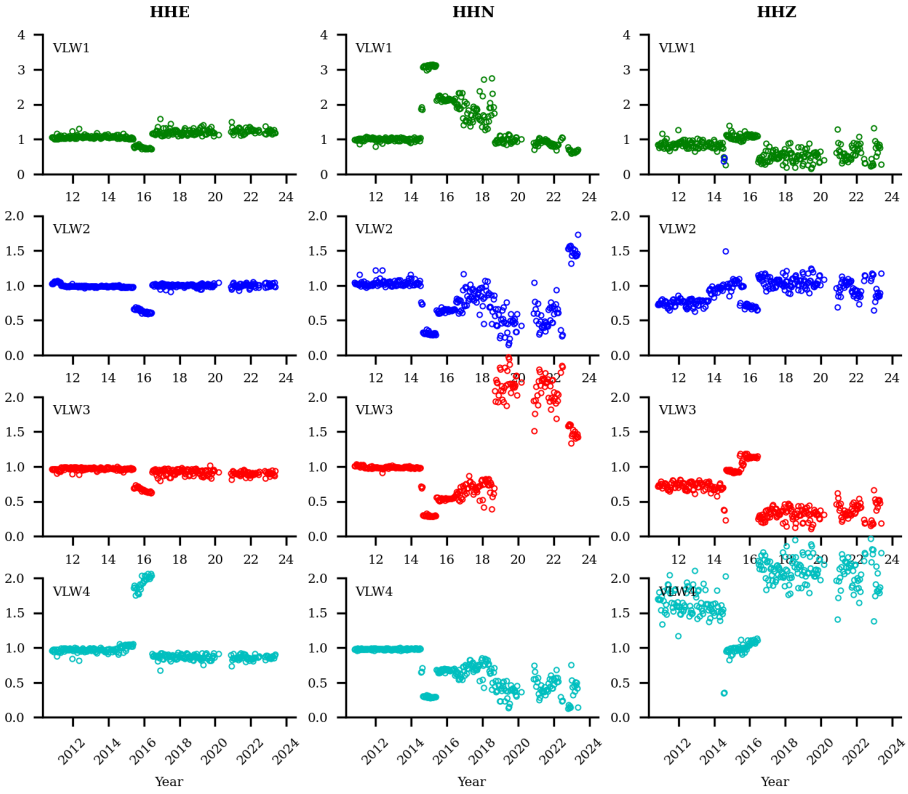

Figure 4.39: *Mean absolute amplitude of 30-minute noise recordings by individual borehole channels of VLW, normalized with respect to this channel's mean absolute amplitude averaged over all borehole levels.*

acquisition by PPB started on 2010-10-16, whereas, just as for OTL, the third epoch started on the second of July 2019 (see Table 3.1). For the first six to seven years, all recordings by station PPB are of good quality. From the beginning of 2017, however, the recordings by channel HHE of PPB4 contain frequent gaps at regular intervals. At the same time, the data that is recorded appears to be representative of the seismic wavefield (they contain both induced events and teleseismic events). From the moment the datalogger has been replaced, however, the spectogram is entirely flat in the sense that the neither high-frequency energy nor microseism energy can be observed (Weemstra & Ruigrok, 2026). A quick check taught us that, since then, events are indeed not present in the data of this channel anymore. An example is given in Figure 4.45.

Borehole station **WMH** is the third of the three stations located around the city of Alkmaar whose data quality we asses. Its normalized mean absolute amplitudes are shown in Figure 4.46. The start of the continuous acquisition by this station coincided with that of OTL (2010-10-16) and the start of the third epoch coincided with both OTL and PPB (see Table 3.1). During most of the 15 years, the recordings by all geophones of WMH are of good quality. During the years 2016 and 2017, however, the recordings by almost all channels contain frequent (short) gaps and the data is of lower quality. This two-year period was preceded by a period of about half a year during which no data was collected. The lower quality of the recordings is clear from both the spectograms and the teleseismic arrivals (Weemstra & Ruigrok, 2026). Since no induced events occurred in the region during this period, we can only evaluate the station's ability to record seismic phases using teleseismic arrivals. Some ad-hoc analysis taught us that teleseismic phases were properly recorded during this period, which renders it unnecessary and unjustified to remove the recordings (despite the overall lower quality). Note that the ability to recover these phases is conditional on the application of the procedure described in Section 4.1. All in all, station WMH does not occur in Table 4.9.

The last six borehole stations whose data quality is assessed concerns the six borehole stations that did not operate in an off-line, triggered mode prior to 2010. These were newly installed around that time, and are characterized by a vertical geophone spacing of 30 meters. The first of these six station is station

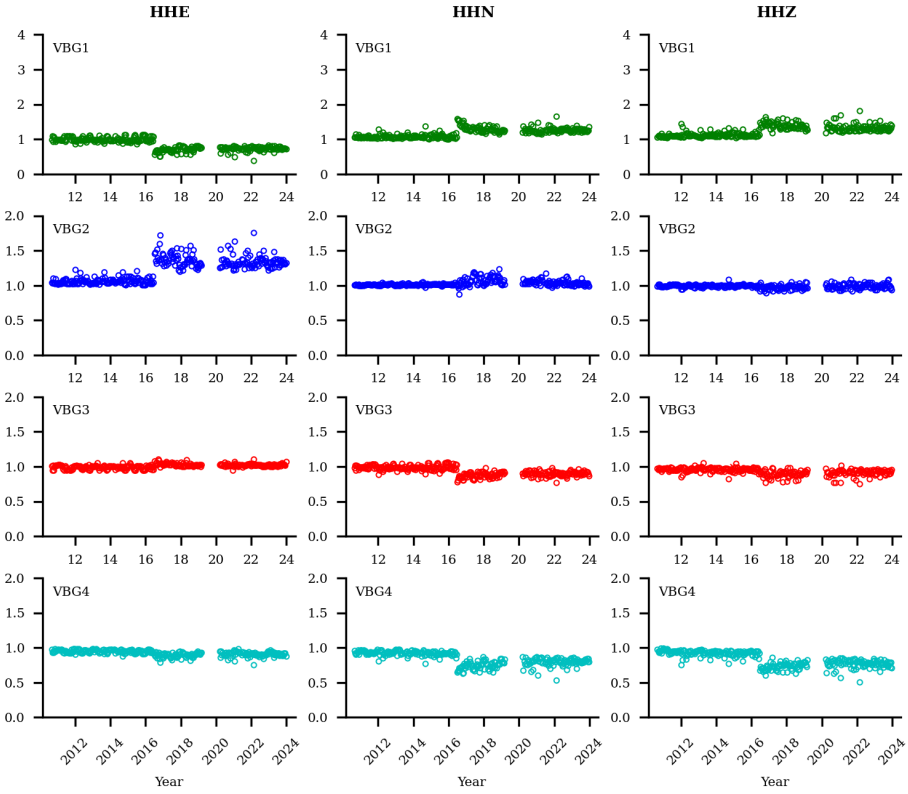

Figure 4.40: *Mean absolute amplitude of 30-minute noise recordings by individual borehole channels of VBG, normalized with respect to this channel's mean absolute amplitude averaged over all borehole levels.*

NIW. Its normalized mean absolute amplitudes are shown in Figure 4.47. Continuous acquisition at NIW started on 2009-05-20, and the third epoch starts at the 15th of February 2018 (see Tables 2.1 and 3.1, respectively). For some reason, the spectograms in our database do not cover all periods for which recordings are available. We therefore performed some additional ad-hoc analyses. These led to the conclusion that (i) the recordings by channel HHZ of geophone NIW2 are corrupt between the beginning of April 2018 and the end of 2021 and (ii) the recordings of channel HHN of geophone NIW3 are corrupt between 2016-05-01 and 2017-09-01. Finally, we observe in Figure 4.47 a strong increase of the amplitudes of the recordings by the vertical channel of NIW3 in 2023. We could not identify the root of this increase, but it may have something to do with the rather strong 50 Hz grid noise. We start to observe this noise after the replacement of the datalogger (see, for example, the induced events recorded by NIW; Weemstra & Ruigrok, 2026). After proper filtering, however, NIW3's HHZ recordings in this time period still show clearly the arrivals of nearby induced events. The recordings therefore remain a valuable asset for future (scientific) research.

The normalized mean absolute amplitudes of station **SUH** are shown in Figure 4.48. Continuous acquisition at SUH started on 2009-08-26, and the third epoch starts at the 13th of June 2016 (see Tables 2.1 and 3.1, respectively). Just as for NIW, the recordings by SUH suffer from stronger 50 Hz grid noise after replacement of the datalogger. Fortunately, upon application of a sufficiently strong low-pass filter (or low-pass pre-filter while removing the instrument response), arrivals of induced events can still be recovered. Apart from this 50 Hz grid noise, the recordings by SUH do not exhibit further shortcomings.

The normalized mean absolute amplitudes of station **SPY** are shown in Figure 4.49. Continuous acquisition at SPY started on 2010-07-08, and its third epoch starts on the 14th of June 2016 (see Tables 2.1 and 3.1, respectively). Even though the spectograms exhibit "anomalous" spectra during a few periods, careful analysis of a number of induced seismic phases reveals that these arrivals are well recorded and of good quality. Roughly speaking, this also applies to the teleseismic phases (see also Weemstra & Ruigrok, 2026). Consequently, none of the recordings by SPY need to be removed from the archive.

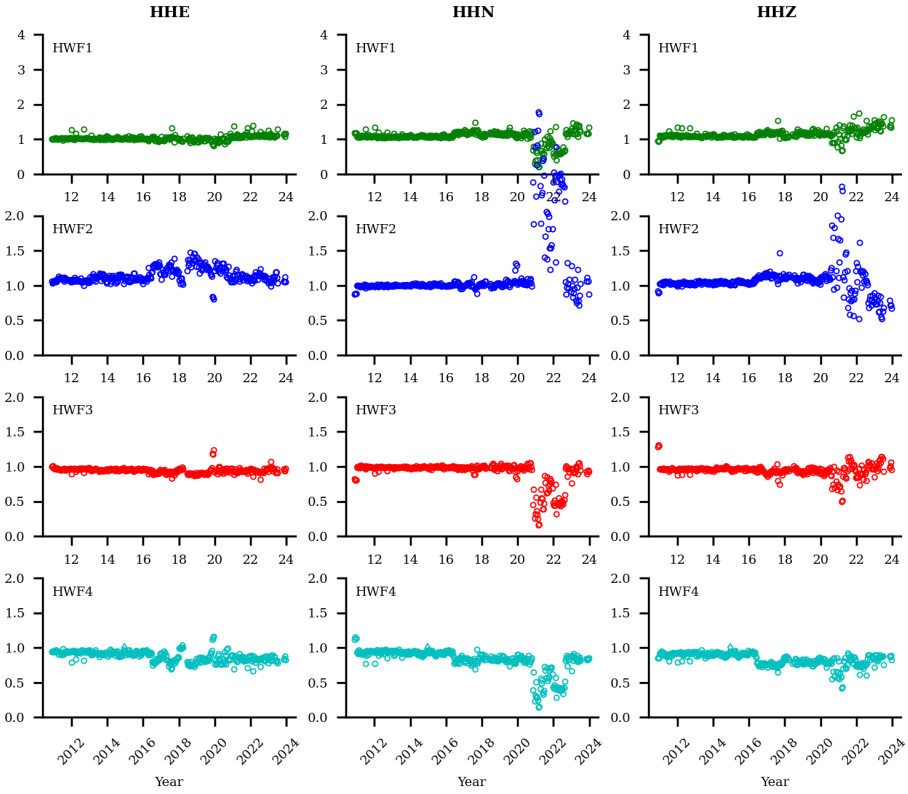

Figure 4.41: *Mean absolute amplitude of 30-minute noise recordings by individual borehole channels of HWF, normalized with respect to this channel's mean absolute amplitude averaged over all borehole levels.*

Station **FDG** is the first of the three borehole station in western Friesland. Its normalized mean absolute amplitudes are shown in Figure 4.50. Continuous acquisition at FDG started on 2009-10-13 and the station never had his datalogger replaced (i.e., it did not enter the third epoch). Both Figure 4.50 and the other indicators on Weemstra and Ruigrok (2026) reveal that, starting mid 2014, something caused the quality of the recordings by this station to deteriorate heavily. Some additional ad-hoc analyses (using teleseismic P and S waves) confirms this. Specifically, apart from the vertical channel of geophone FDG1 and the HHN channels of FDG3 and FDG4, its recordings do not represent the Earth's motions since the 10th of August 2014 and can hence be removed from archive. After this date, none of the events in our public earthquake catalog contain either a pick or magnitude estimate based on FDG's recordings.

Station **ZWE** is the second of the three borehole station in western Friesland and continuous acquisition started on 2010-03-24. Only recently has this station his datalogger replaced (2026-01-27). Its normalized mean absolute amplitudes are shown in Figure 4.51. Overall, the quality of the recordings by ZWE is good. In Figure 4.51, we do observe some amplitude variations over the course of the 12 years for which data is available. During 2013 and 2014, for example, the amplitudes of HHZ of geophone ZWE3 are lower. This is also clear from the spectograms and teleseismic phases (Weemstra & Ruigrok, 2026). At the same time, its recordings during those two years still contain the checked teleseismic arrivals. This implies that when it comes to the phase and hence the timing, this data can still be useful for (scientific) studies. After 2014, the amplitude appears again to be consistent with the amplitudes of third level geophones of the other borehole stations. Until approximately 2017, channel HHN of ZWE2 occasionally displays elevated noise amplitudes (Weemstra & Ruigrok, 2026). This channel's recordings of both teleseismic and induced events are of good quality though. We therefore did not further investigate this.

Station **WYN** is the last of the three borehole station in western Friesland whose data quality we assess. Continuous acquisition at this site started on 2010-03-03 and WYN never had his datalogger replaced. Its normalized mean absolute amplitudes are shown in Figure 4.52. Channel HHN of geophone WYN1

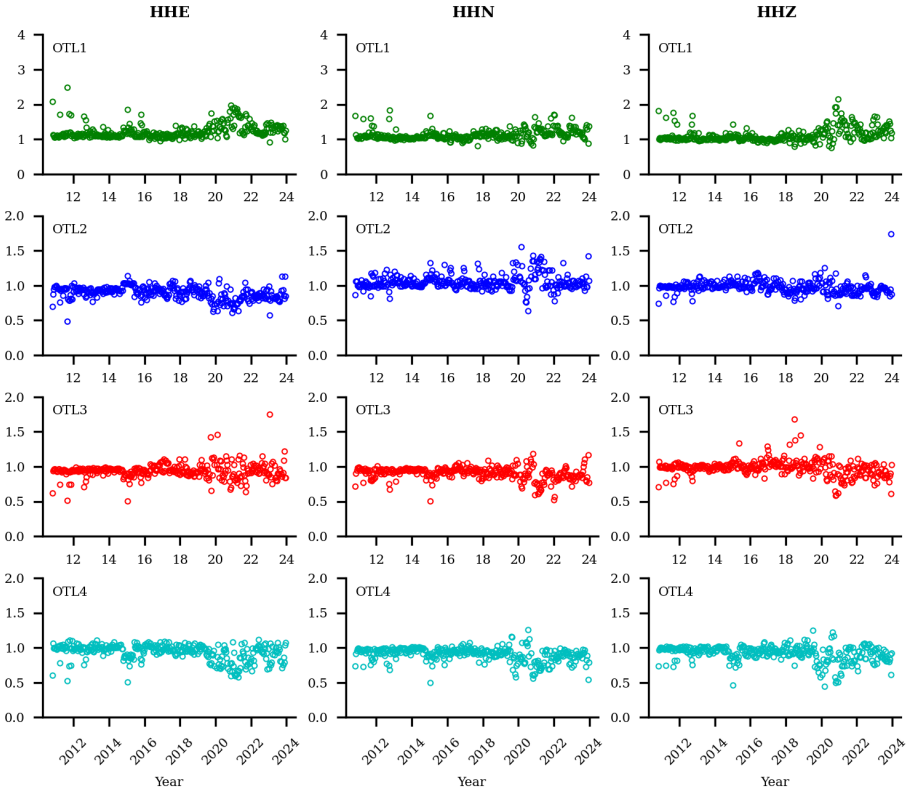

Figure 4.42: *Mean absolute amplitude of 30-minute noise recordings by individual borehole channels of OTL, normalized with respect to this channel's mean absolute amplitude averaged over all borehole levels.*

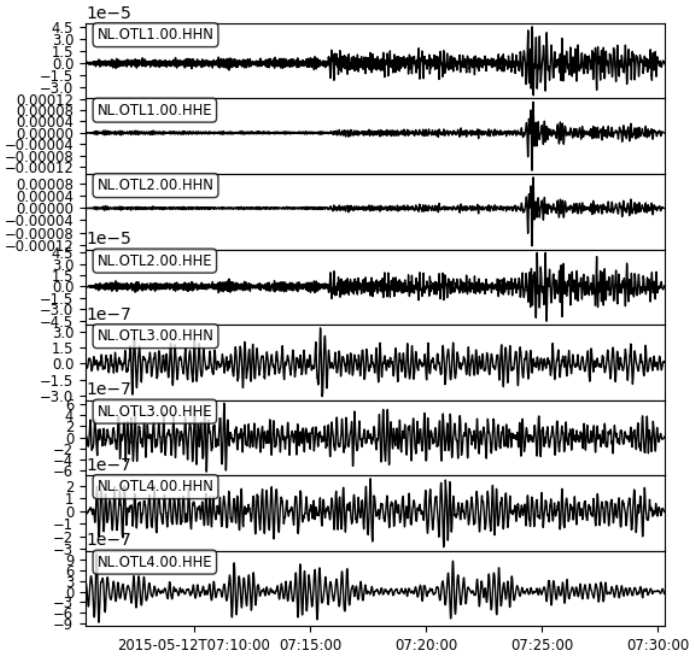

Figure 4.43: *S waves generated by a Magnitude 7.2 event in Nepal recorded by borehole station OTL. The event occurred on the 12th of May 2015. The recordings were band-pass filtered between 0.1 and 1.0 Hz and instrument responses were removed. The arrival of the direct S wave can clearly be identified on the horizontal channels of OTL1 and OTL2, whereas it is conspicuously absent in the recordings of the two deeper geophones. Note that traces were normalized individually.*

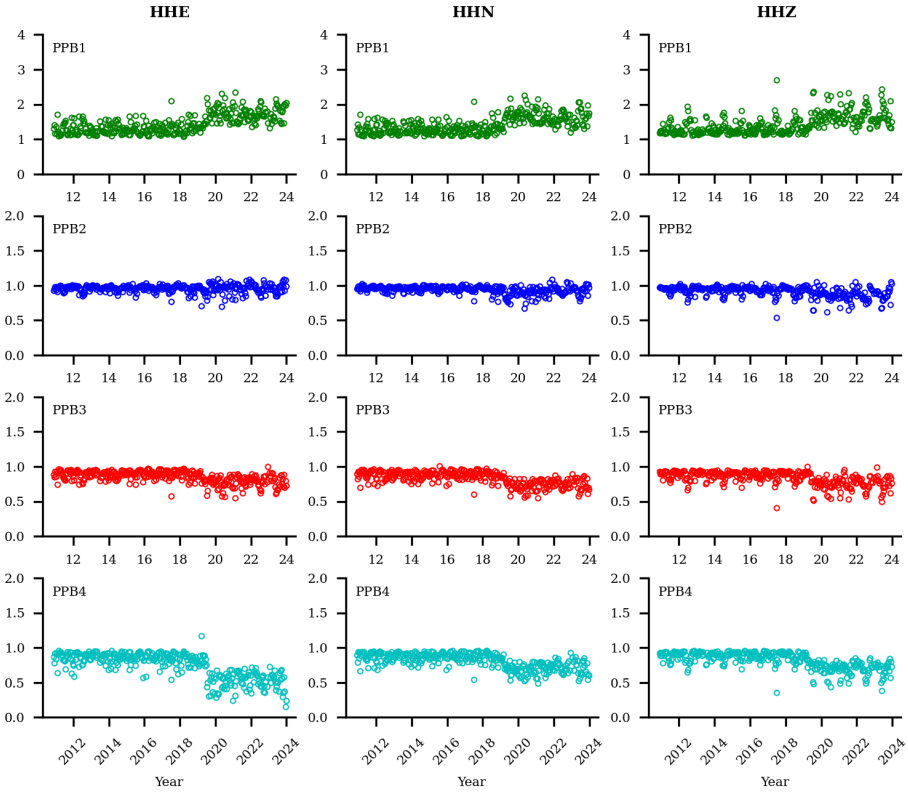

Figure 4.44: *Mean absolute amplitude of 30-minute noise recordings by individual borehole channels of PPB, normalized with respect to this channel's mean absolute amplitude averaged over all borehole levels.*

starts to deteriorate during 2013, and from the end of 2014 onward its recordings can be considered useless. Starting from October 2013, the vertical component of geophone WYN3 did not deliver correct readings. This is clear from both the spectograms and the teleseismic arrivals (Weemstra & Ruigrok, 2026). The same applies to channel HHE of that geophone. In both cases, this is also clear from the drop in amplitudes of these two channels' recordings at that moment in time (see Figure 4.52).

All periods of corrupted data have been summarized in Table 4.9. A quick check of Appendix G in Dost et al. (2023) reveals that the malfunctioning of some of these channels/geophones was already known. For the majority of the channels with corrupted data at the start of the second epoch, however, no data issues were reported during the first epoch. This suggests that the start of the continuous acquisition and the associated update of the A/D boards and PCs (described in Section 3.1) "triggered" these. This merely shows the vulnerability of a seemingly simple change in the hardware setup. Note that, in general, we often did not attempt to infer whether corrupted data was due to the geophone, the datalogger, or any other hardware component (e.g., a broken cable).

Finally, we observed that geophones NIW1, SUH1, SPY1, FDG1, ZWE1, and WYN1 generated a timing signal on a channel dubbed HHT. Such type of signal is described in detail in the report describing the triggered data (Dost et al., 2023). The HHT recordings are sampled at 100 Hz, and consist of pulses every second with a length of a few samples. The minute mark can be recognized by the omission of the last pulse before the minute mark. The timing signal is generated during the second epoch only and disappears with the advent of the Kinemetrics dataloggers (note that borehole stations FDG, ZWE, and WYN remained in the second epoch for the entire period of recording). We checked the timing signals for correlation with the segmentation of the raw wavefield recordings by those geophones, but did not find any. We therefore conclude that these data carry no information whatsoever, and can be removed from our archive.

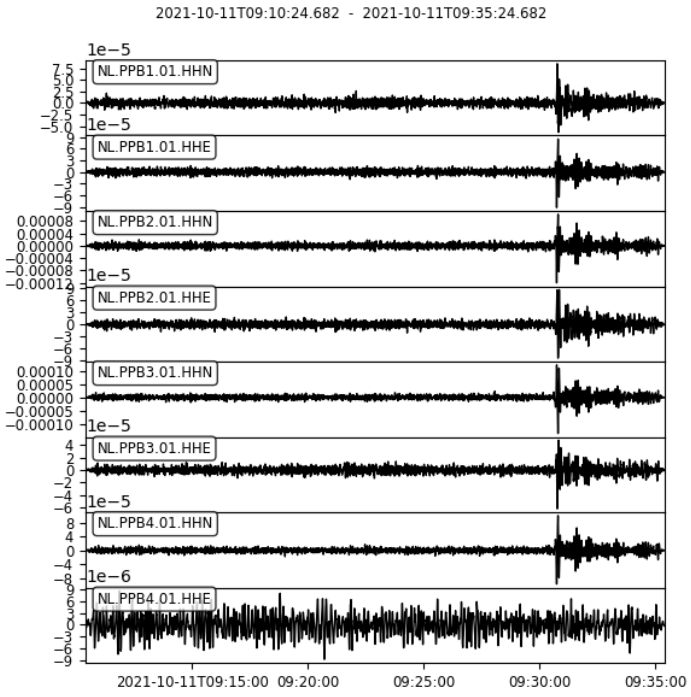

Figure 4.45: *S waves generated by a Magnitude 6.9 event south of Alaska recorded by borehole station PPB. The event occurred on the 11th of October 2021. The recordings were band-pass filtered between 0.1 and 1.0 Hz, and instrument responses were removed. Except for the recording by channel HHE of PPB4, the arrival of the direct S wave can clearly be identified on all horizontal channels. Traces were normalized individually.*

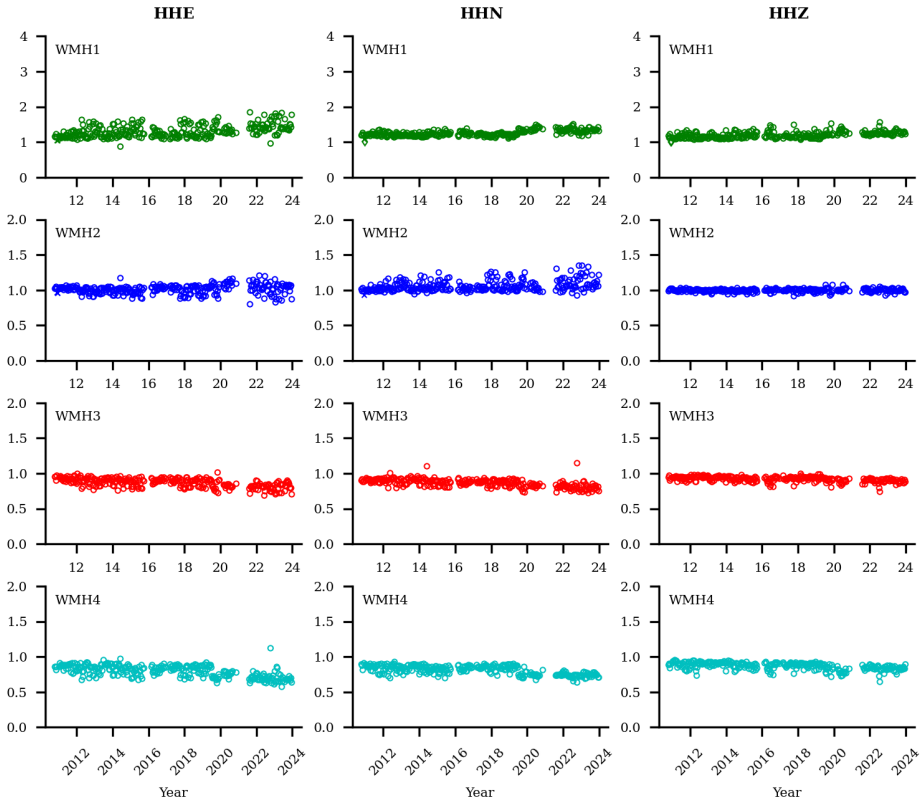

Figure 4.46: *Mean absolute amplitude of 30-minute noise recordings by individual borehole channels of WMH, normalized with respect to this channel's mean absolute amplitude averaged over all borehole levels.*

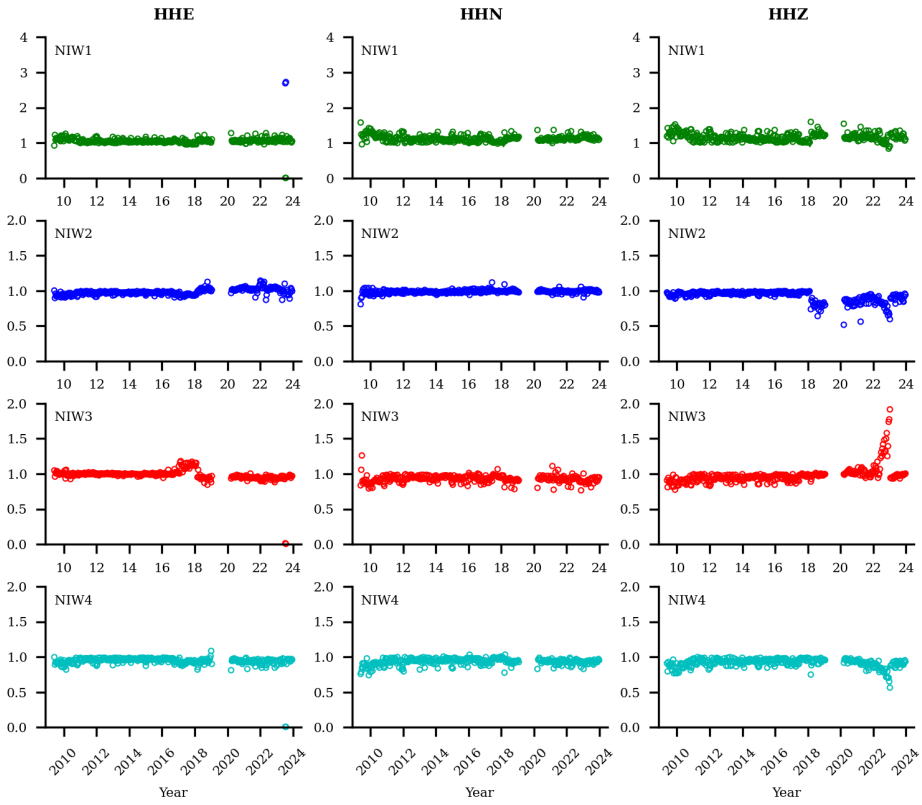

Figure 4.47: *Mean absolute amplitude of 30-minute noise recordings by individual borehole channels of NIW, normalized with respect to this channel's mean absolute amplitude averaged over all borehole levels.*

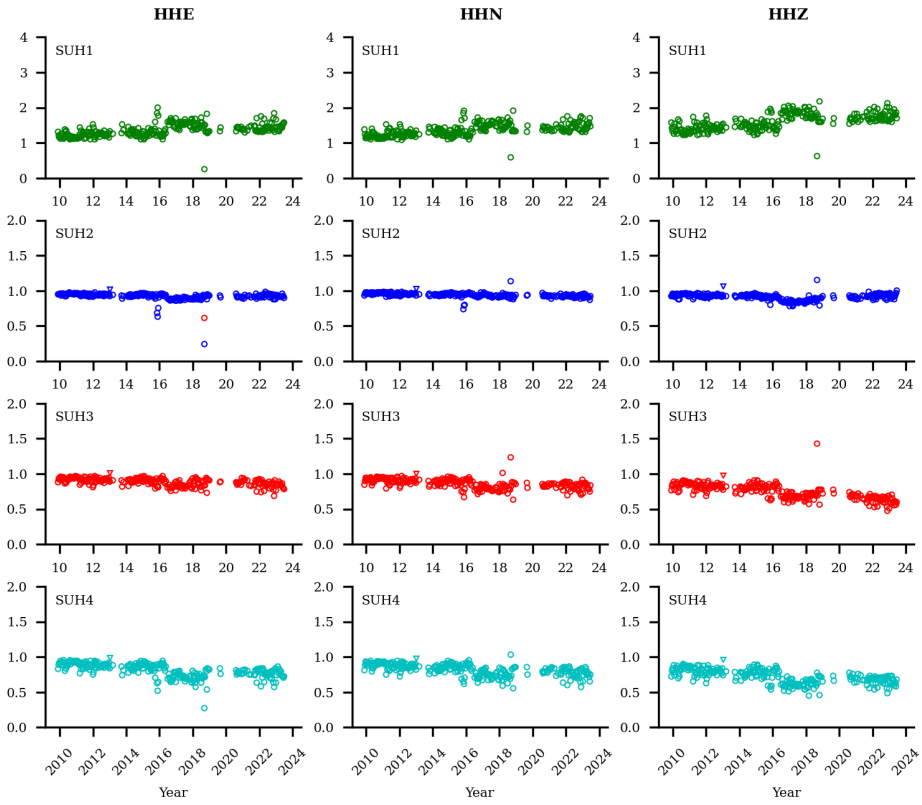

Figure 4.48: *Mean absolute amplitude of 30-minute noise recordings by individual borehole channels of SUH, normalized with respect to this channel's mean absolute amplitude averaged over all borehole levels.*

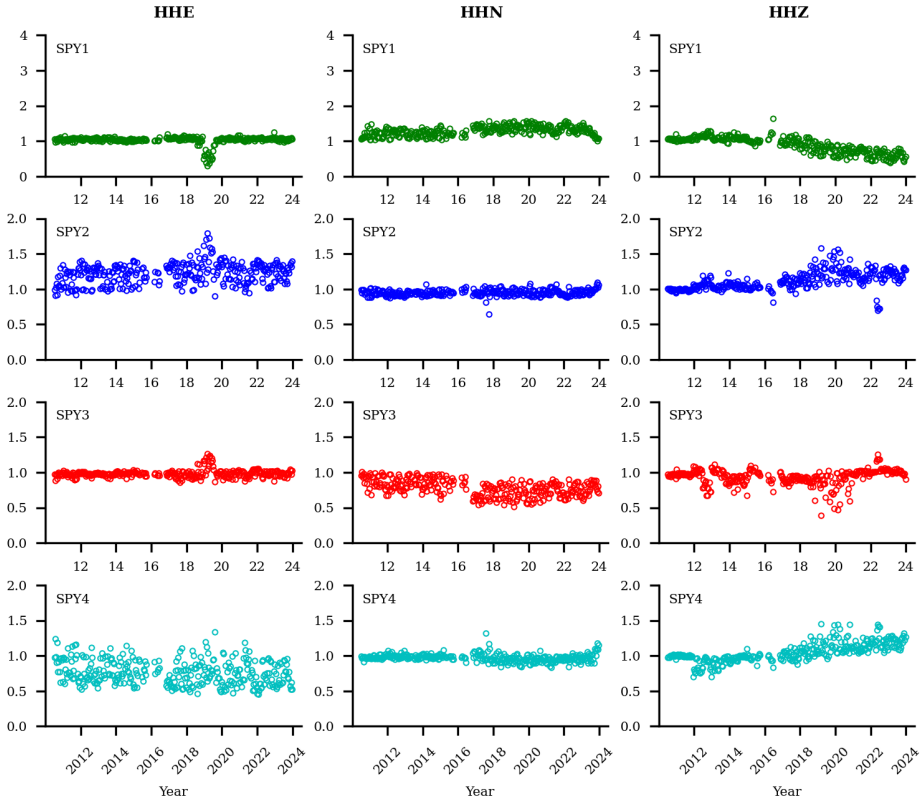

Figure 4.49: *Mean absolute amplitude of 30-minute noise recordings by individual borehole channels of SPY, normalized with respect to this channel's mean absolute amplitude averaged over all borehole levels.*

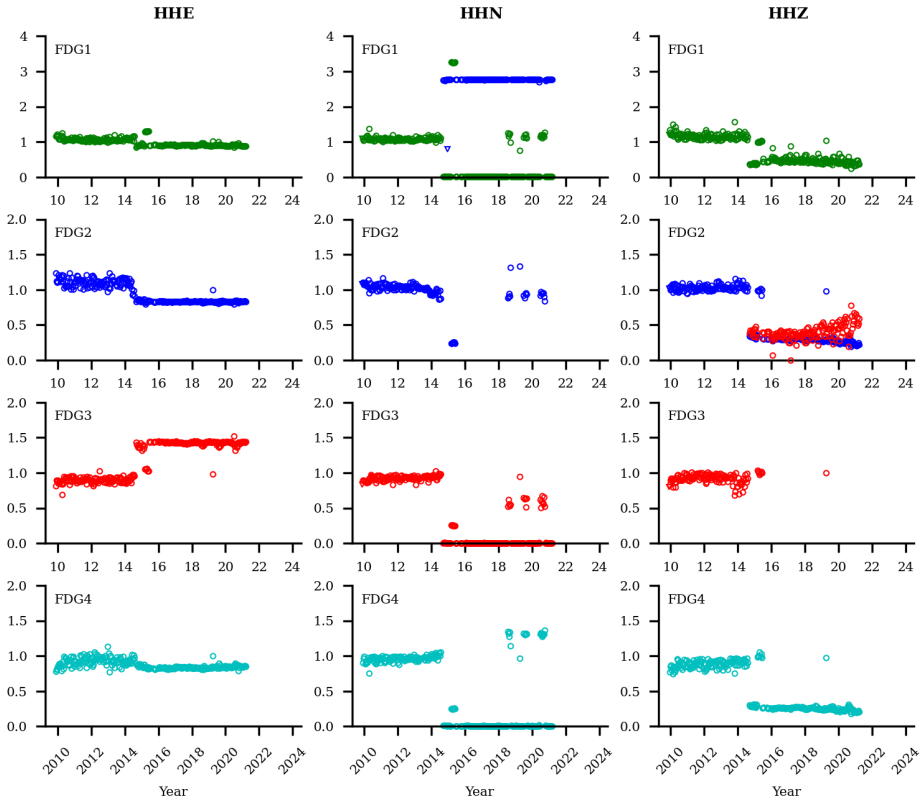

Figure 4.50: *Mean absolute amplitude of 30-minute noise recordings by individual borehole channels of FDG, normalized with respect to this channel's mean absolute amplitude averaged over all borehole levels.*

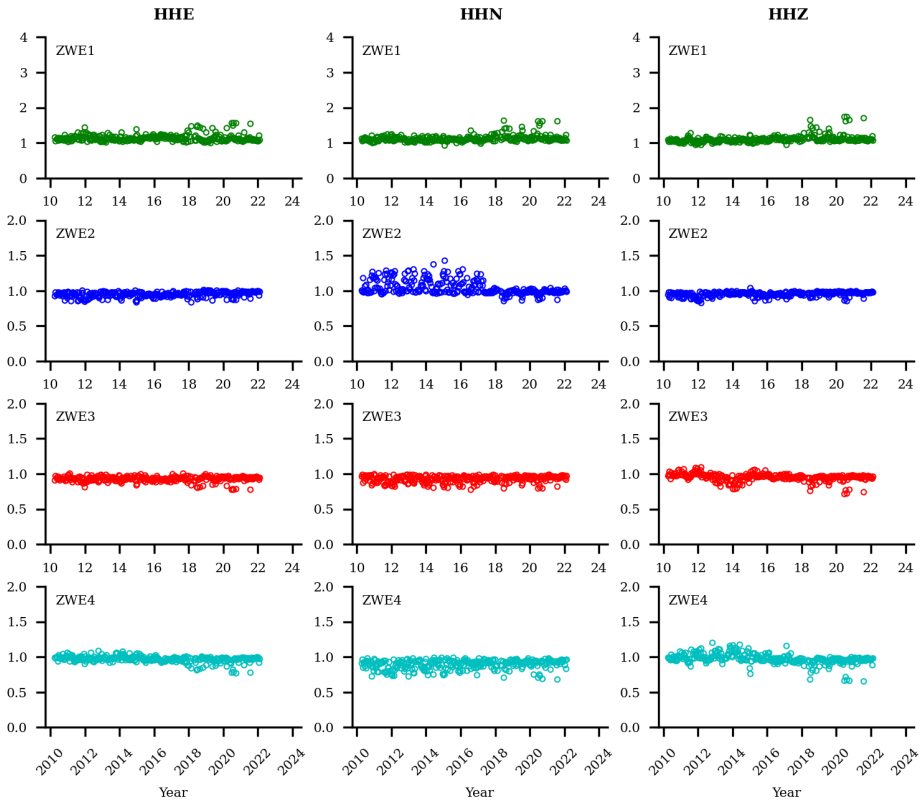

Figure 4.51: *Mean absolute amplitude of 30-minute noise recordings by individual borehole channels of ZWE, normalized with respect to this channel's mean absolute amplitude averaged over all borehole levels.*

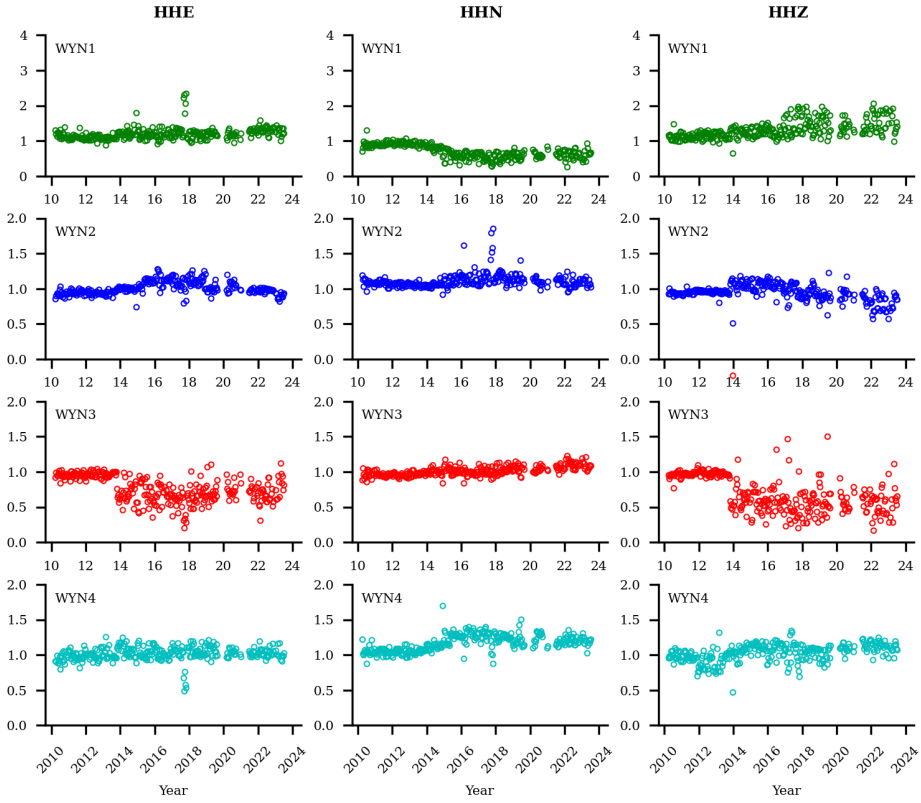

Figure 4.52: *Mean absolute amplitude of 30-minute noise recordings by individual borehole channels of WYN, normalized with respect to this channel's mean absolute amplitude averaged over all borehole levels.*

Table 4.9: *Continuous data that that has been removed from our archive, based on the analysis in this section. Unix-style wildcards are used in the sense that '?' can match any single character, whereas square brackets indicate which single characters could be matched. For example, 'FSW?' implies all geophones of borehole station FSW, whereas 'HH[NE]' indicates that the period of corrupt data applies to channels HHN and HHE. During the second epoch, geophones NIW1, SUH1, SPY1, FDG1, ZWE1, and WYN1 generated a timing signal on a channel dubbed HHT. These timing signals have been deleted from our archive (see main text). None of the events in KNMI's public earthquake catalog contain either a pick or magnitude estimate based on these removed continuous recordings.*

Station	Geophone	Channel	Periods	Close channel(s)?
FSW	FSW?	HH?	Third epoch	Yes
ENM	ENM1	HHE	Both epochs	Yes
	ENM2	HHN	Third epoch	Yes
	ENM3	HHE	2015-03-29 – now	Yes
WDB	WDB1	HHZ	Third epoch	Yes
	WDB3	HH?	Both epochs	Yes
ZLV	ZLV0	HHE	Start of second epoch – 2011-08-22	
			2011-10-06 – 2012-03-01	
			2012-03-26 – end of second epoch	N/A
		HHN	2012-04-20 – 2012-09-20	
			2013-01-01 – end of second epoch	N/A
		HHZ	2012-04-05 – 2012-10-02	
			2013-01-30 – 2013-12-10	N/A
	ZLV1	HHZ	2022-12-20 – now	Yes
	ZLV4	HHN	2017-08-16 – now	Yes
ZL2	ZL2?	HH?	None (all channels OK)	N/A
ENV	ENV1	HHE	Start of second epoch – 2010-06-01	No
		HHN	Start of second epoch – 2010-05-15	No
	ENV2	HHE	Start of second epoch – 2010-06-01	No
		HHN	Start of second epoch – 2010-06-01	No
	ENV3	HHE	Start of second epoch – 2010-06-01	
			2010-08-10 – 2010-12-01	
			2014-05-01 – end of second epoch	No
		HHN	Start of second epoch – 2010-06-06	
			2010-07-20 – 2011-03-15	
			2014-05-01 – end of second epoch	No
		HHZ	Start of second epoch – 2010-11-01	No
	ENV4	HHE	Start of second epoch – 2010-06-10	
			2010-08-01 – 2010-11-20	
			2014-05-01 – end of second epoch	No
		HHN	Start of second epoch – 2010-05-20	
			2010-07-10 – 2010-11-01	
			2014-05-01 – end of second epoch	No
		HHZ	Start of second epoch – 2010-05-20	
			2010-07-10 – 2010-11-01	
			2014-05-01 – end of second epoch	No
VLW	VLW1	HHN	Both epochs	Yes
	VLW2	HHN	2022-06-01 – now	Yes
		HHZ	2014-09-01 – now	Yes
	VLW3	HHN	2018-09-01 – now	Yes
	VLW4	HHE	2015-06-01 – end of second epoch	No
		HHZ	Both epochs	Yes
VBG	VBG1	HHE	Both epochs	Yes

Table 4.9: *Continued*

Station	Geophone	Channel	Periods	Close channel(s)?
HWF	HWF2	HHN	2020-11-20 – now	Yes
		HHZ	2020-07-10 – now	Yes
OTL	OTL3	HH[NE]	2014-10-05 – 2015-06-01	No
	OTL4	HH?	2014-10-05 – 2015-06-01	No
PPB	PPB4	HHE	Third epoch	Yes
NIW	NIW1	HHT	Second epoch	N/A
	NIW2	HHZ	2018-04-01 – 2021-12-31	No
	NIW3	HHN	2016-05-01 – 2017-09-01	No
SUH	SUH1	HHT	Second epoch	N/A
SPY	SPY1	HHT	Second epoch	N/A
FDG	FDG1	HHT	Second epoch	N/A
		HHZ	2014-08-10 – 2015-06-10	No
		HH[NE]	2014-08-10 – now	Yes
	FDG2	HH?	2014-08-10 – now	Yes
	FDG3	HH[ZE]	2014-08-10 – now	Yes
	FDG4	HH[ZE]	2014-08-10 – now	Yes
ZWE	ZWE1	HHT	Second epoch	N/A
WYN	WYN1	HHT	Second epoch	N/A
	WYN1	HHN	2014-10-01 – now	Yes
	WYN3	HH[ZE]	2013-10-01 – now	Yes

5. Conclusions

Prior to 2015, seismic monitoring in the north of the Netherlands relied predominantly on a set of 18 first-generation borehole stations. A number of these stations, however, continue to be online to date. At each of these sites, a vertical array of (typically four) three-component geophones is installed. Maximum depths range from 120 to 300 meters. In this report, we checked the quality of all continuous waveform data recorded by these 18 stations. A detailed analysis of the older, "triggered" recordings by 12 of these 18 borehole stations can be found in Dost et al. (2023). The data analysis pertains (i) an explicit computation and subsequent evaluation of the instrument responses, (ii) a careful check of the polarity and orientation of the different channels, and (iii) an elaborate assessment of the overall data quality of the recordings. Starting with the instrument responses, we now list the most important conclusions.

The instrument response, which is part of the meta-data, describes quantitatively the conversion from particle velocity in meters per second to counts. For the continuous data acquisition period we distinguish between two epochs. We refer to these two epochs as the second and third epoch, because the period in which the stations operated in a triggered mode (station-specific, but up to 2010 approximately) is referred to as the first epoch (Dost et al., 2023). During the second epoch, the hardware (amplifier, A/D converter, etc.) remained the same as during the first epoch. Up to a frequency-dependent deviation that does not exceed 1%, we find that the (StationXML-) reported instrument responses for this epoch are consistent with the electronic specifications of the instrumentation installed in the field. This small difference is due the incorrect assumption of the 8200 Ohm shunt resistance resulting in a damping of 0.707.

During the third epoch, the hardware and corresponding meta-data altered significantly. In particular, Granite dataloggers from Kinemetrics with an electrical resistance of 220,000 Ohm were installed. Since the (non-infinite) resistance of these dataloggers was not included in the computation of the instrument responses, again a small difference was found between the actual response of the instrumentation installed in the field and the reported instrument response. For this epoch, the maximum difference in amplitude (at 4.5 Hz) was close to 2%.

For both epochs, we deem the deviation of the recomputed instrument response from the reported instrument response too small to warrant an update of the meta-data: the found deviations translate to travel time errors and magnitude estimation errors that are one to two orders of magnitude smaller than typical (arrival-time) picking uncertainties and magnitude estimation uncertainties.

A second conclusion pertains the polarity and orientations of the different channels. We identify reversed polarities on both the horizontal and vertical components. In particular, we find that the replacement of the old acquisition setup with the Granite dataloggers, which marks the start of the third epoch, results in a polarity flip on all channels. This can be explained by the fact that a polarity flip was induced by the electronic circuits effectuating the different filters during the second epoch. This was, however, not taken into account while hooking the stations up to the Kinemetrics dataloggers at the start of the third epoch. Consequently, stations hitherto exhibiting a polarity consistent with the meta-data had their polarity becoming inconsistent with the meta-data during third epoch, and vice versa.

Finally, the overall quality of the recordings is assessed. This is achieved by (i) analyzing the stability of the amplitudes, (ii) inspecting the spectograms routinely computed as part of KNMI's suite of quality control tools, and (iii) evaluation of the P and S-wave arrivals of nearby induced events. The aggregate result of these three approaches is summarized in Table 4.9. Clearly, significant periods of corrupt data have been identified, which have been removed from our archive. Altogether, our analyses triggered the following actions:

- Table 4.9 summarizes the result of the overall quality analysis in Section 4.3. For all geophones for which periods of corrupt data are identified, this corrupt data has been removed from our waveform archive. In case the last column indicates that the channel should be closed, this has been implemented with the end date of the last epoch being the first day of the period for which recordings were identified to be corrupt.
- While transitioning from the second to the third epoch, the StationXMLs of three of the 15 stations whose datalogger was replaced report a different overall sensitivity (2.50205e+08 Counts/m/s versus 9.05611e+07 Counts/m/s for the other 12 stations). The reported instrument response is the same for all 15 though. These three stations are PPB, OTL, and WMH. Obviously, this cannot be. The sensitivity has been corrected in the StationXMLs of these stations.
- For the second epoch, the dips of all HHZ channels of stations NIW, SUH, and FDG has been set to 90 instead of −90 in their StationXML.
- For the third epoch, the dips of all HHZ channels of stations ENM, WDB, ZLV, ENV, VLW, VBG, OTL, WMH, SPY, HWF, and PPB, have been set to 90 instead of −90 in their StationXML.
- For the second epoch, 180 degrees has been added to the StationXML azimuths of all HHN and HHE channels of WDB, ZLV, ENV, VLW, HWF, OTL, and WMH.
- For the third epoch, 180 degrees has been added to the StationXML azimuths of all HHN and HHE channels of ENM, VBG, and PPB.
- The StationXML azimuths of the HHN channels of stations NIW, SUH, and SPY have been set to the values listed in Table 4.8, and the HHE channels to those values +90 degrees.
- In the dataloggers of stations NIW and SUH, HHN was renamed to HHE, and HHE to HHN (SPY has recently been dismantled).
- In the waveform database, for stations NIW, SUH and SPY, file and segment names have been renamed from HHE to HHN and from HHN to HHE.

Execution of these meta-data updates and archive cleanup increased the overall quality of KNMI's waveform archive. This is to the advantage of our own operations (and as such the general public), but also research institutes and academic institutions working with our data will reap the benefits of these efforts.

Bibliography

Aster, R. C., Shearer, P. M., & Berger, J. (1990). Quantitative measurements of shear wave polarizations at the Anza seismic network, southern California: Implications for shear wave splitting and earthquake prediction. *Journal of Geophysical Research: Solid Earth*, *95*(B8), 12449–12473.

Telford, W. M., Geldart, L. P., & Sheriff, R. E. (1990). *Applied geophysics* (Vol. 1). Cambridge university press.

Kennett, B. L. N., & Engdahl, E. R. (1991). Traveltimes for global earthquake location and phase identification. *Geophysical Journal International*, *105*(2), 429–465. https://doi.org/10.1111/j.1365-246X.1991.tb06724.x

KNMI. (1993). Netherlands Seismic and Acoustic Network. https://doi.org/10.21944/e970fd34-23b9-3411-b366-e4f72877d2c5

Diephuis, G., & Asmussen, U. (1995, June). *KNMI arrays in Groningen en Drenthe* (tech. rep.). NAM.

Crotwell, H. P., Owens, T. J., & Ritsema, J. (1999). The TauP Toolkit: Flexible Seismic Travel-time and Ray-path Utilities. *Seismological Research Letters*, *70*(2), 154–160.

Aki, K., & Richards, P. G. (2002). *Quantitative Seismology* [Medium: Hardcover]. University Science Books.

Dost, B., & Haak, H. (2002, July). *A comprehensive description of the KNMI seismological instrumentation* (tech. rep. No. TR-245). Royal Netherlands Meteorological Institute. De Bilt.

Storchak, D. A., Schweitzer, J., & Bormann, P. (2003). The IASPEI Standard Seismic Phase List. *Seismological Research Letters*, *74*(6), 761–772. https://doi.org/10.1785/gssrl.74.6.761

Drijkoningen, G. G. (2007). *GeoLOFAR-001: The geophysics applications in LOFAR*.

Helmholtz-Centre Potsdam - GFZ German Research Centre for Geosciences and gempa GmbH. (2008). The SeisComP seismological software package. GFZ Data Services. https://doi.org/10.5880/GFZ.2.4.2020.003

Hadziioannou, C., Larose, E., Coutant, O., Roux, P., & Campillo, M. (2009). Stability of monitoring weak changes in multiply scattering media with ambient noise correlation: Laboratory experiments. *The Journal of the Acoustical Society of America*, *125*(6), 3688–95. https://doi.org/10.1121/1.3125345

Dost, B., Ruigrok, E., & Spetzler, J. (2017a). Development of seismicity and probabilistic hazard assessment for the groningen gas field [Publisher: Cambridge University Press]. *Netherlands Journal of Geosciences*, *96*(5), s235–s245. https://doi.org/10.1017/njg.2017.20

Dost, B., Ruigrok, E., & Spetzler, J. (2017b). Development of seismicity and probabilistic hazard assessment for the Groningen gas field. *Geologie en Mijnbouw/Netherlands Journal of Geosciences*, *96*(5), s235–s245. https://doi.org/10.1017/njg.2017.20

Hofman, L., Ruigrok, E., Dost, B., & Paulssen, H. (2017). A shallow seismic velocity model for the Groningen Area in the Netherlands. *Journal of Geophysical Research: Solid Earth*, *122*. https://doi.org/10.1002/2017JB014419

Ntinalexis, M., Bommer, J. J., Ruigrok, E., Edwards, B., Pinho, R., Dost, B., Correia, A. A., Uilenreef, J., Stafford, P. J., & van Elk, J. (2019). Ground-motion networks in the Groningen field: Usability and consistency of surface recordings [Publisher: Journal of Seismology]. *Journal of Seismology*, *23*(6), 1233–1253. https://doi.org/10.1007/s10950-019-09870-x

Ruigrok, E., & Dost, B. (2019). Seismic monitoring and site-characterization with near-surface vertical arrays. *Near Surface Geoscience Conference and Exhibition*, 1–5. https://doi.org/10.3997/2214-4609.201902455

Ruigrok, E., Domingo-Ballesta, J., Hazel, G. J. V. D., Dost, B., & Evers, L. (2019). Groningen explosion database. *First Break*, *37*(8), 37–41.

FDSN. (2020). *Fdsn source identifiers*. Retrieved June 20, 2025, from https://docs.fdsn.org/projects/source-identifiers/en/latest/

Bader, M. K. M. (2021). *Seismic and Newtonian noise modeling for Advanced Virgo and Einstein Telescope* [PhD-Thesis - Research and graduation internal]. Vrije Universiteit Amsterdam.

Koymans, M. R., Domingo Ballesta, J., Ruigrok, E., Sleeman, R., Trani, L., & Evers, L. G. (2021). Performance Assessment of Geophysical Instrumentation Through the Automated Analysis of Power Spectral Density Estimates. *Earth and Space Science*, *8*(9). https://doi.org/10.1029/2021EA001675

International Federation of Digital Seismographs Networks (FDSN). (2022, February). StationXML, version 1.2.

Dost, B., Zhou, W., & Ruigrok, E. (2023, May). *Quality assurance and publication of the KNMI 1995-2013 induced seismicity data* (tech. rep. No. TR-412). KNMI, R&D Seismology and Acoustics. De Bilt.

Kinemetrics. (2023, August). *ROCK Digitizer user manual* (tech. rep. No. Document 300715, Revision K). KINEMETRICS, Inc.

Ruigrok, E., Kruiver, P., & Dost, B. (2023, August). *Construction of earthquake location uncertainty maps for the Netherlands* (tech. rep. No. TR-405). KNMI, R&D Seismology and Acoustics. De Bilt.

Masfara, L. O. M., & Weemstra, C. (2024). Hamiltonian Monte Carlo to Characterize Induced Earthquakes: Application to a ML 3.4 Event in the Groningen Gas Field and the Role of Prior. *Earth and Space Science*, *11*(1). https://doi.org/10.1029/2023EA003184

Spetzler, J., Ruigrok, E., & Bouwman, D. (2024). Hypocenter uncertainty analysis of induced and tectonic earthquakes in the Netherlands. *Journal of Seismology*. https://doi.org/10.1007/s10950-024-10205-8

Hainzl, S., Dahm, T., & Zöller, G. (2025). Modelling induced seismicity in Groningen based on subcritical stressed faults. *Geophysical Journal International*, *241*(2), 840–851. https://doi.org/10.1093/gji/ggaf064

Weemstra, C., & Ruigrok, E. (2026, November). Quality analysis of the continuous data recorded by KNMI's first-generation borehole geophone network: Supporting information. https://doi.org/10.5281/zenodo.18704381

Appendices

A. A StationXML example

In this Appendix we show a part of the StationXML (see International Federation of Digital Seismographs Networks (FDSN), 2022, for a detailed description of the StationXML format) for borehole station FSW3 to demonstrate how the response information during the second epoch (specified in Section 3) is captured. We show the response for channel HHZ and highlight the different stages: Stage 1 describes response of the sensor including filters (blue); Stage 2 the response of the datalogger (purple).

```
<Channel code="HHZ" startDate="2010-04-29T00:00:00.000000Z"
endDate="2016-06-14T08:00:00.000000Z" restrictedStatus="open" locationCode="00">
   <Latitude unit="DEGREES">53.2135</Latitude>
   <Longitude unit="DEGREES">7.1195</Longitude>
   <Elevation>1.0</Elevation>
   <Depth>150.0</Depth>
   <Azimuth unit="DEGREES">0.0</Azimuth>
   <Dip unit="DEGREES">-90.0</Dip>
   <SampleRate unit="SAMPLES/S">100.0</SampleRate>
   <SampleRateRatio>
     <NumberSamples>100</NumberSamples>
     <NumberSeconds>1</NumberSeconds>
   </SampleRateRatio>
   <ClockDrift unit="SECONDS/SAMPLE">0.0</ClockDrift>
   <Sensor resourceId="Sensor/20220524125311.55886.28">
     <Type>SM6</Type>
     <Description>SM6</Description>
     <Model>SM6</Model>
   </Sensor>
   <DataLogger resourceId="Datalogger/20220524125311.5588.27">
     <Description>FSW3.2010.119.HHZ00</Description>
   </DataLogger>
   <Response>
     <InstrumentSensitivity>
       <Value>107434000.0</Value>
       <Frequency>10.0</Frequency>
       <InputUnits>
         <Name>M/S</Name>
         <Description>None</Description>
       </InputUnits>
       <OutputUnits>
         <Name>COUNTS</Name>
         <Description>None</Description>
       </OutputUnits>
     </InstrumentSensitivity>

      <Stage number="1">
       <PolesZeros name="FSW3.2010.119.HE00" resourceId="ResponsePAZ#20140909071419.14789.44">
         <InputUnits>
           <Name>M/S</Name>
         </InputUnits>
```

```
<OutputUnits>
  <Name>V</Name>
</OutputUnits>
<PzTransferFunctionType>LAPLACE (RADIANS/SECOND)</PzTransferFunctionType>
<NormalizationFactor>7.981400148e+17</NormalizationFactor>
<NormalizationFrequency unit="HERTZ">10.0</NormalizationFrequency>
<Zero number="14">
  <Real>0.0</Real>
  <Imaginary>0.0</Imaginary>
</Zero>
<Zero number="15">
  <Real>0.0</Real>
  <Imaginary>0.0</Imaginary>
</Zero>
<Zero number="16">
  <Real>-28.4377</Real>
  <Imaginary>0.0</Imaginary>
</Zero>
<Zero number="17">
  <Real>-28.4377</Real>
  <Imaginary>0.0</Imaginary>
</Zero>
<Zero number="18">
  <Real>0.0</Real>
  <Imaginary>0.0</Imaginary>
</Zero>
<Zero number="19">
  <Real>0.0</Real>
  <Imaginary>0.0</Imaginary>
</Zero>
<Pole number="0">
  <Real>-19.99</Real>
  <Imaginary>19.996</Imaginary>
</Pole>
<Pole number="1">
  <Real>-19.99</Real>
  <Imaginary>-19.996</Imaginary>
</Pole>
<Pole number="2">
  <Real>-6.28931</Real>
  <Imaginary>0.0</Imaginary>
</Pole>
<Pole number="3">
  <Real>-6.28931</Real>
  <Imaginary>0.0</Imaginary>
</Pole>
<Pole number="4">
  <Real>-34.3278</Real>
  <Imaginary>173.108</Imaginary>
</Pole>
<Pole number="5">
  <Real>-34.3278</Real>
  <Imaginary>-173.108</Imaginary>
</Pole>
<Pole number="6">
  <Real>-98.348</Real>
  <Imaginary>145.623</Imaginary>
</Pole>
```

```
          <Pole number="7">
            <Real>-98.348</Real>
            <Imaginary>-145.623</Imaginary>
          </Pole>
          <Pole number="8">
            <Real>-147.079</Real>
            <Imaginary>96.3482</Imaginary>
          </Pole>
          <Pole number="9">
            <Real>-147.079</Real>
            <Imaginary>-96.3482</Imaginary>
          </Pole>
          <Pole number="10">
            <Real>-174.203</Real>
            <Imaginary>29.8213</Imaginary>
          </Pole>
          <Pole number="11">
            <Real>-174.203</Real>
            <Imaginary>-29.8213</Imaginary>
          </Pole>
          <Pole number="12">
            <Real>-0.666667</Real>
            <Imaginary>0.700877</Imaginary>
          </Pole>
          <Pole number="13">
            <Real>-0.666667</Real>
            <Imaginary>-0.700877</Imaginary>
          </Pole>
        </PolesZeros>
        <StageGain>
          <Value>32786.02006</Value>
          <Frequency>10.0</Frequency>
        </StageGain>}
      </Stage>
       <Stage number="2">
        <Coefficients>
          <InputUnits>
            <Name>V</Name>
          </InputUnits>
          <OutputUnits>
            <Name>COUNTS</Name>
          </OutputUnits>
          <CfTransferFunctionType>DIGITAL</CfTransferFunctionType>
        </Coefficients>
        <Decimation>
          <InputSampleRate unit="HERTZ">100.0</InputSampleRate>
          <Factor>1</Factor>
          <Offset>0</Offset>
          <Delay>0.0</Delay>
          <Correction>0.0</Correction>
        </Decimation>
        <StageGain>
          <Value>3276.8</Value>
          <Frequency>0.0</Frequency>
        </StageGain>}
      </Stage>
    </Response>
</Channel>
```

B. On the response of a shunted geophone

In this Appendix, we first introduce the model discussed in Section 12.3.2 of "Quantitative Seismology" of Aki & Richards (2002). Subsequently, we build on this using the description in Bader (2021). Let us start, however, by introducing the response function $X(s)$ describing the response of a passive (shunted) geophone. This response function reads

$$X(s) = S\frac{-s^2}{(s-s_1)\,(s-s_1^*)}, \tag{B.1}$$

where the complex numerator and denominator are written as (complex) polynomials. The complex variable s is defined as $s \equiv \sigma + j\omega$, where both σ and the angular frequency ω are real, and j is the imaginary unit. The response function has two zeros of $(0., 0.)$ and two poles: s_1 and it's complex conjugate s_1^*. Furthermore, S is an overall "gain" factor. This (non-complex) factor is commonly referred to as the *effective sensitivity*, and typically has units [V/(m/s)] in our context. It can be recovered from the StationXML by multiplying the *NormalizationFactor* with the *StageGain* of the stage describing the geophone response (provided these are reported at the same frequency). Below, we gradually build up the model that allows us to compute, explicitly, the poles and effective sensitivity.

B.1 General (spring-dashpot) description of an inertial seismometer

The following is predominantly based on, and extracted from Aki and Richards (2002). An appropriate model for an inertial seismometer is that of a mass m attached to a point of the Earth through a parallel arrangement of a spring and a dashpot, as shown in Figure B.1. Assuming that all motion is restricted to the x-direction, we denote the motion of the Earth in the inertial reference frame as $u(t)$ and the motion of mass m relative to the Earth as $\xi(t)$. The spring will exert a force proportional to its elongation $\xi - l_0$ from its zero-tension length l_0, and the dashpot will exert a force proportional to the relative velocity $\dot{\xi}(t)$ between the mass and the Earth (with a dot over a symbol indicating differentiation with respect to time). Representing these constants of proportionality as k and D, the equation of motion is given by

$$\begin{aligned} m\frac{\mathrm{d}^2\left[\xi(t)+u(t)\right]}{\mathrm{d}t^2} &= \sum_{i=1}^{3} F_i \\ &= mg - k[\xi(t) - l_0] - D\frac{\mathrm{d}\xi(t)}{\mathrm{d}t} \\ &= -k[\xi(t) - \xi_0] - D\frac{\mathrm{d}\xi(t)}{\mathrm{d}t}, \end{aligned} \tag{B.2}$$

where in the last step we have used the fact that if the initial length of the spring (with no tension) is l_0, then the equilibrium length ξ_0 for a vertical sensor is related to the spring modulus (k), to the mass (m), and to the strength of the gravitational field (g) by $k(\xi_0 - l_0) = mg$.

Rewriting the displacement $\xi(t) - \xi_0$ relative to the equilibrium position ξ_0 as $\xi(t)$, we have

$$-m\ddot{u}(t) = m\ddot{\xi}(t) + D\dot{\xi}(t) + k\xi(t). \tag{B.3}$$

The inertia sensor responds only to $\ddot{u}$, and Equation (B.3) shows that one can reproduce the acceleration of Earth motion by a linear and measurable combination of $\xi(t)$ and its time derivatives. For very rapid

Earth motion, the first term of the right-hand side of (B.3) dominates, and $\ddot{\xi}$ becomes nearly equal to $-\ddot{u}$. In other words, the record $\xi(t)$ reproduces the Earth's displacement $-u(t)$ if the movement is rapid. For very low frequency motion, in which the third term on the right-hand side dominates, the term $k\xi$ becomes nearly equal to $-m\ddot{u}$. It follows that the record $\xi(t)$ reproduces the acceleration $\ddot{u}(t)$ if the motion is slow. The sensitivity in this case is proportional to T_0^2, where $T_0 = 2\pi/\sqrt{k/m}$ is the undamped period of the sensor and $\sqrt{k/m}$ the corresponding *undamped angular frequency.*

B.2 Poles and zeros

In order to to comply with the description in Dost and Haak (2002) and Bader (2021, chapter 4), we now write the equation of motion in the complex domain using a Laplace transformation. The Laplace transform of an arbitrary function $h(t)$ is defined as

$$H(s) \equiv \int_0^\infty h(t)e^{-st}\mathrm{d}t \tag{B.4}$$

where $s \equiv \sigma + j\omega$. The Laplace transform can be considered an extension of the Fourier transform, which is recovered for $\sigma = 0$. In the complex domain (i.e., after Laplace transformation,) the relation between the time dependent functions $\xi(t)$ and $u(t)$ is given by a function $X(s)$, i.e.,

$$\xi(s) = U(s)X(s). \tag{B.5}$$

$X(s)$ is usually referred to as the *response function* of the linear system.

After Laplace transformation, Eq. (B.3) can be written as

$$-ms^2U(s) = ms^2\xi(s) + Ds\xi(s) + k\xi(s), \tag{B.6}$$

where we have used the fact that differentiation in the time domain corresponds to multiplication by s

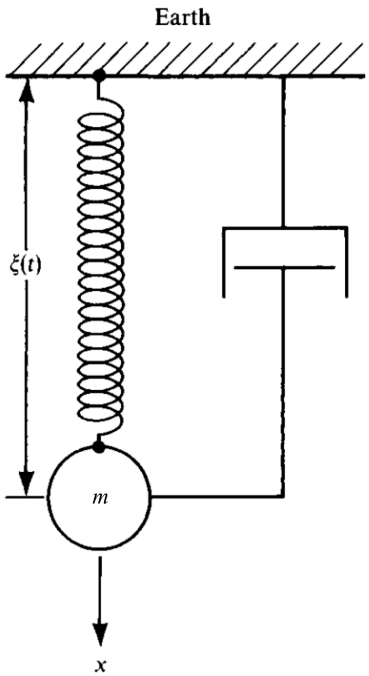

Figure B.1: *Adapted from Aki and Richards (2002): A seismometer based on an inertial sensor is essentially a mass suspended by a parallel arrangement of spring and dashpot. If the initial length of the spring (with no tension) is l_0, then the equilibrium length ξ_0 for a vertical sensor is related to the spring modulus (k), to the mass (m), and to the strength of the gravitational field (g) by $k(\xi_0 - l_0) = mg$.*

in the complex (Laplace) domain. Equation (B.6) implies that

$$X(s) = \frac{\xi(s)}{U(s)} = \frac{-s^2}{s^2 + (D/m)s + (k/m)}. \tag{B.7}$$

Introducing now, in line with Aki and Richards (2002), $\epsilon \equiv D/(2m)$ and $\omega_0^2 \equiv k/m$, this equation can be written as

$$X(s) = \frac{-s^2}{s^2 + 2\epsilon s + \omega_0^2}. \tag{B.8}$$

This response function has two zeros $(0, 0)$. Further introducing the *damping constant* $h \equiv \epsilon/\omega_0$, the denominator can be factorized as $(s + \epsilon - j\omega_0\sqrt{1-h^2})(s + \epsilon + j\omega_0\sqrt{1-h^2})$ in case the system is *underdamped* (i.e., $0 \leq h < 1$). This factorization implies that the two poles are $-\epsilon \pm j\omega_0\sqrt{1-h^2}$. For a detailed discussion of the representation of a response function in terms of poles and zeros, we refer to the International Federation of Digital Seismographs Networks (FDSN) (2022).

For $h > 1$, the system is overdamped and the response will be delayed longer in time for frequencies exceeding the eigenfrequency $f_0 \equiv 1/T_0 = \omega_0/(2\pi)$ (Aki & Richards, 2002). *Critical damping* is achieved using a value of $h = 1$, i.e., $D/(2m) = \sqrt{k/m}$, which implies that no undesirable ringing occurs. For $h < 1$, the system is underdamped and (some) ringing occurs. A damping of $h = 0.707$ (70.7% of critical damping) is considered ideal as the flat range of the response is slightly extended and the amplitude distortion is minimal (Telford et al., 1990). For this value, the gain at the eigenfrequency f_0 is -3dB of that in the flat range.

B.3 A modern geophone

The description of a seismometer as that of a mass attached to a point of the Earth through a parallel arrangement of a spring and a dashpot is merely a simple model. A modern geophone in fact consist of a moving mass m, a coil in a magnetic field $\mathbf{B}$ and a spring with stiffness k inside a case. In this case, the (velocity-proportional) mechanical damping force does not result from a dashpot, but is due to the (velocity-proportional) friction and mechanical damping between the mass and the housing. Furthermore, the relative motion of the coil (mounted to the housing and hence the Earth) with respect to the magnet (fixed to the mass m) induces an electrical damping force. With respect to the relative motion ξ, this second force coincides with $Bli(t)$, where l is the length of the coil wire, B the strength of the magnetic field (inside the coil) due to the magnet, and $i(t)$ the current in the coil (Biot-Savart Law; see Eq. 12.43 in Aki & Richards, 2002). Introducing the sensitivity of the geophone $G \equiv Bl$ in units [V/(m/s)], this force can be written as $Gi(t)$. The quantity G is often referred to as the *open-circuit sensitivity* in the geophone's specifications. It is a characteristic of the geophone and gives information on how the velocity of the ground is translated to a voltage. For example, for the SM-6 low frequency geophone (B-coil) deployed in the first-generation borehole network of the KNMI it coincides with 28.8 V/(m/s). Adding this second force to the equation of motion (Equation B.3), we obtain

$$-m\ddot{u}(t) = m\ddot{\xi}(t) + b\dot{\xi}(t) + Gi(t) + k\xi(t). \tag{B.9}$$

As we will derive further below, the mechanical damping force b (units: [N]) contributes to the unitless damping constant h, which was introduced above, with a value of $b/(2m\omega_0)$. The latter value is in the geophone's specifications often referred to as the *open-circuit damping*. Denoting the current in the complex domain by $I(s)$, Laplace transformation of equation (B.9) gives,

$$ms^2U(s) = \left(-ms^2 - bs - k\right)\xi(s) - GI(s). \tag{B.10}$$

The coil attached to the moving mass has a resistance R_c and inductance L_c. While moving in the magnetic field, a voltage $V_c = G\dot{\xi}(t)$ is induced, which is opposed by a voltage $V_{\text{emf}} = -L_c\dot{i}(t)$ due to the elektromotive force from the change in current in the system. Consequently the voltage equilibrium in the system is expressed as

$$V_c + V_{\text{emf}} = i(t)\left(R_s + R_c\right), \tag{B.11}$$

where R_s is the shunt resistance. Rewriting gives

$$V_c = (R_s + R_c)\, i(t) + L_c \dot{i}(t), \tag{B.12}$$

which, upon substitution of $G\dot{\xi}(t)$ for V_c, reads after Laplace transformation as

$$Gs\xi(s) = (R_s + R_c + L_c s)\, I(s). \tag{B.13}$$

B.4 response function for output voltage

Equations (B.10) and (B.13) allow us to derive the response function between the Earth's particle velocity $sU(s)$ and the output voltage $V_{out}(s) = R_s I(s)$ (Bader, 2021). Let us therefore first solve Equation (B.10) for $\xi(s)$, which gives

$$\xi(s) = \frac{ms^2 U(s) + GI(s)}{-ms^2 - bs - k} \tag{B.14}$$

Substituting this in Equation (B.13) and multiplying both sides by R_s, we obtain

$$GsR_s \left(\frac{ms^2 U(s) + GI(s)}{-ms^2 - bs - k} \right) = (R_s + R_c + L_c s) V_{\text{out}}(s) \tag{B.15}$$

which can be reformulated as

$$V_{\text{out}}(s) \left(1 + \frac{G^2 s}{(ms^2 + bs + k)\,(R_s + R_c)} \right) = \frac{-1}{(R_s + R_c)} \frac{GR_s ms^3 U(s)}{(ms^2 + bs + k)}. \tag{B.16}$$

Dividing both sides by $sU(s)$ and rearranging, we obtain

$$\frac{V_{\text{out}}(s)}{sU(s)} = \left(1 + \frac{G^2 s}{(ms^2 + bs + k)\,(R_s + R_c + L_c s)} \right)^{-1} \frac{-1}{(R_s + R_c + L_c s)} \frac{GR_s ms^2}{(ms^2 + bs + k)}, \tag{B.17}$$

which after some algebra yields

$$\begin{aligned} \frac{V_{\text{out}}(s)}{sU(s)} &= \left(\frac{-GR_s m}{R_s + R_c + L_c s} \right) \left(\frac{s^2}{ms^2 + \left(b + \frac{G^2}{(R_s + R_c + L_c s)} \right) s + k} \right) \\ &= \left(\frac{GR_s}{R_s + R_c + L_c s} \right) \left(\frac{-s^2}{s^2 + 2\omega_0 h s + \omega_0^2} \right), \end{aligned} \tag{B.18}$$

which is the response function of a damped harmonic oscillator with eigenfrequency $\omega_0 \equiv \sqrt{k/m}$ and damping $h = \frac{1}{2m\omega_0} \left(b + \frac{G^2}{R_s + R_c + L_c s} \right)$. Note that h can be separated in $h_0 = \frac{b}{2m\omega_0}$ and $h_e = \frac{1}{2m\omega_0} \frac{G^2}{R_s + R_c + L_c s}$, where h_0 represents the mechanical damping of the spring-mass system, and h_e the electrical damping. Furthermore, the prefactor in Equation (B.18) is the *effective sensitivity* that was introduced in Equation (B.1) (i.e., $S = \frac{GR_s}{R_s + R_c + L_c s}$).

It is usually assumed that the inductance L_c is rather small, in the order of a few Henry. This means that $L_c s$ is very small in comparison to R_s in the frequency range of interest and therefore often can be neglected. By adjusting the external shunt resistance R_s the damping can be used to re-shape the frequency response of the sensor. A geophone with a high shunt resistance will oscillate for a certain amount of time when subjected to an impulse. The number of oscillations can be damped by decreasing the shunt resistance down to a critical damping after which the coil does not oscillate anymore. A detailed discussion of the harmonic oscillator's damping is beyond the scope of this Appendix, and we refer Aki and Richards (2002) for this.

B.5 The (potential) effect of the datalogger

Ideally, the datalogger, which converts voltages to counts, has an input impedance R_{dl} that is several orders of magnitude larger than the shunt resistance. Only when this is true will the sensor damping

and sensitivity remain the same whether the datalogger is attached or not. If the impedance difference becomes smaller than a few orders of magnitude, the datalogger will influence the sensor electronics, changing damping and therefore its poles. This can be explained by the fact that the shunt resistor and the datalogger act in parallel. The total resistance of R_{tot} of this parallel arrangement is given by

$$R_{\text{tot}} = \frac{R_s R_{dl}}{R_s + R_{dl}}. \tag{B.19}$$

For $R_{dl}/R_s \to \infty$, $R_{\text{tot}} \to R_s$, and response function (B.18) correctly describes the response of the system (and hence so do the derived poles). If this is not the case, however, one needs to replace R_s by R_{tot} in equation (B.18), resulting in a different effective sensitivity, a different damping h, and hence different poles. The Granite dataloggers marking the start of the third epoch, for example, have a resistance R_{dl} of 220,000 Ohm (102,400 Ohm actual datalogger resistance, plus approximately 118,000 Ohm resulting from the breakout board mounted on top of the datalogger). This implies that not a value of $R_s = 8200$ Ohm should be used to compute h, but that it should be replaced with a value of $R_{\text{tot}} = 8200 \times 220000/(8200 + 220000) = 7905$ Ohm.

C. Daily data availability of channel HHE of geophone FSW5

Example of daily data availability for channel HHE of the lowest geophone of each vertical array. Here, the daily data availability of channel HHE of station FSW5 is shown. The daily data availability of channel HHE of the lowest geophone of the other borehole arrays can be found in the repository accompanying this report (Weemstra & Ruigrok, 2026). The data availability of the other two channels appears to coincide with HHE. We performed a brief check, and the data availability (of all channels) of the other geophones of the same borehole array in fact also largely coincides with the data availability of the lowest geophone. This is not surprising given that all borehole geophones of a station were hooked up to the same datalogger. These overviews were extracted from ORFEUS' European Integrated Data Archive (EIDA), which can be accessed from the following webpage.

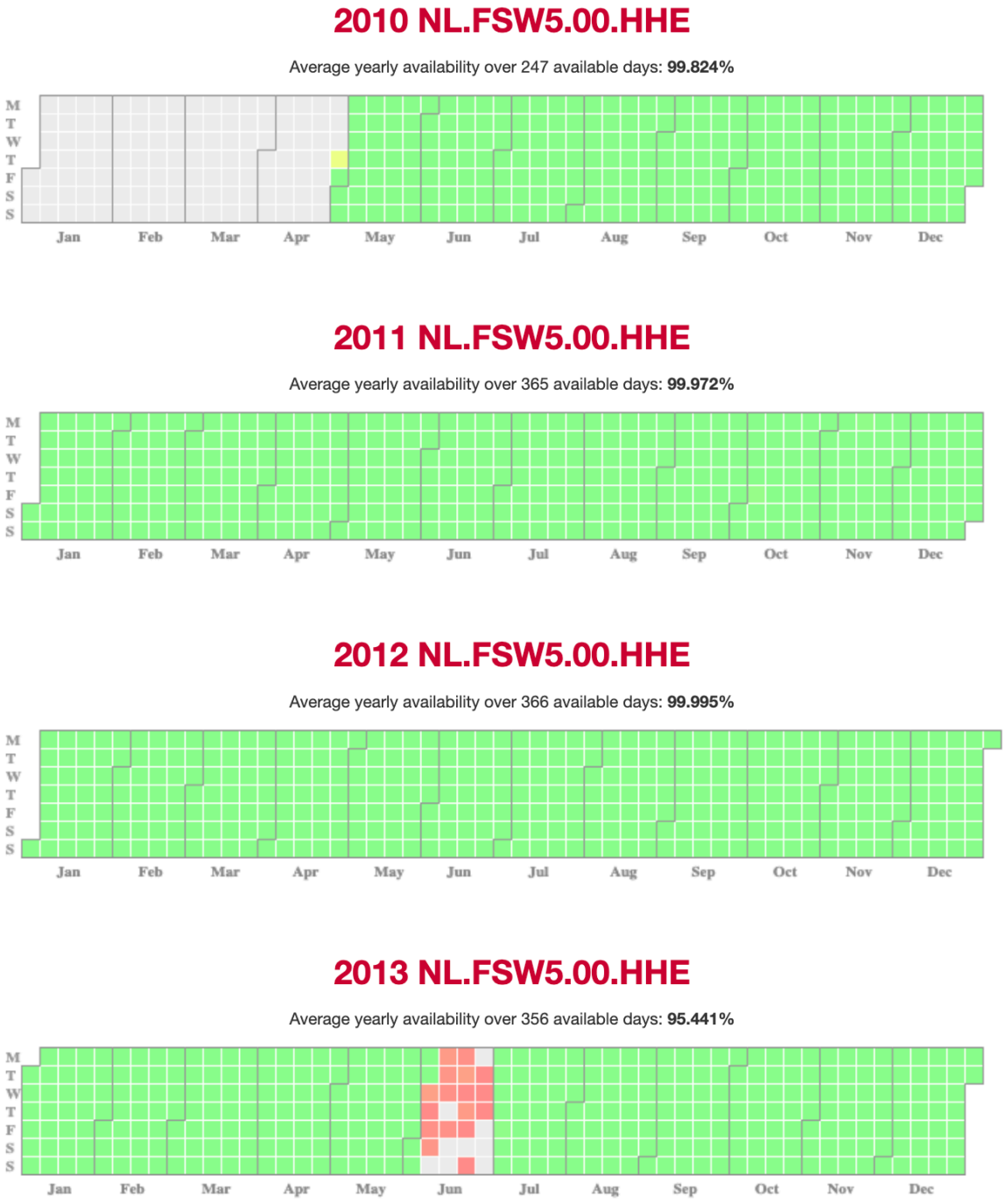

Figure C.1: *Daily data availability (percentages) of channel HHE of station FSW5. Color scale runs from red to green, with red indicating (almost) no data availability and green indicating (almost) 100% data availability. Grey indicates no metrics are available for that day (which in most instances probably implies that continuous recordings are unavailable). Days with 24 hours of data (100%) available are depicted with a star on top of them.*

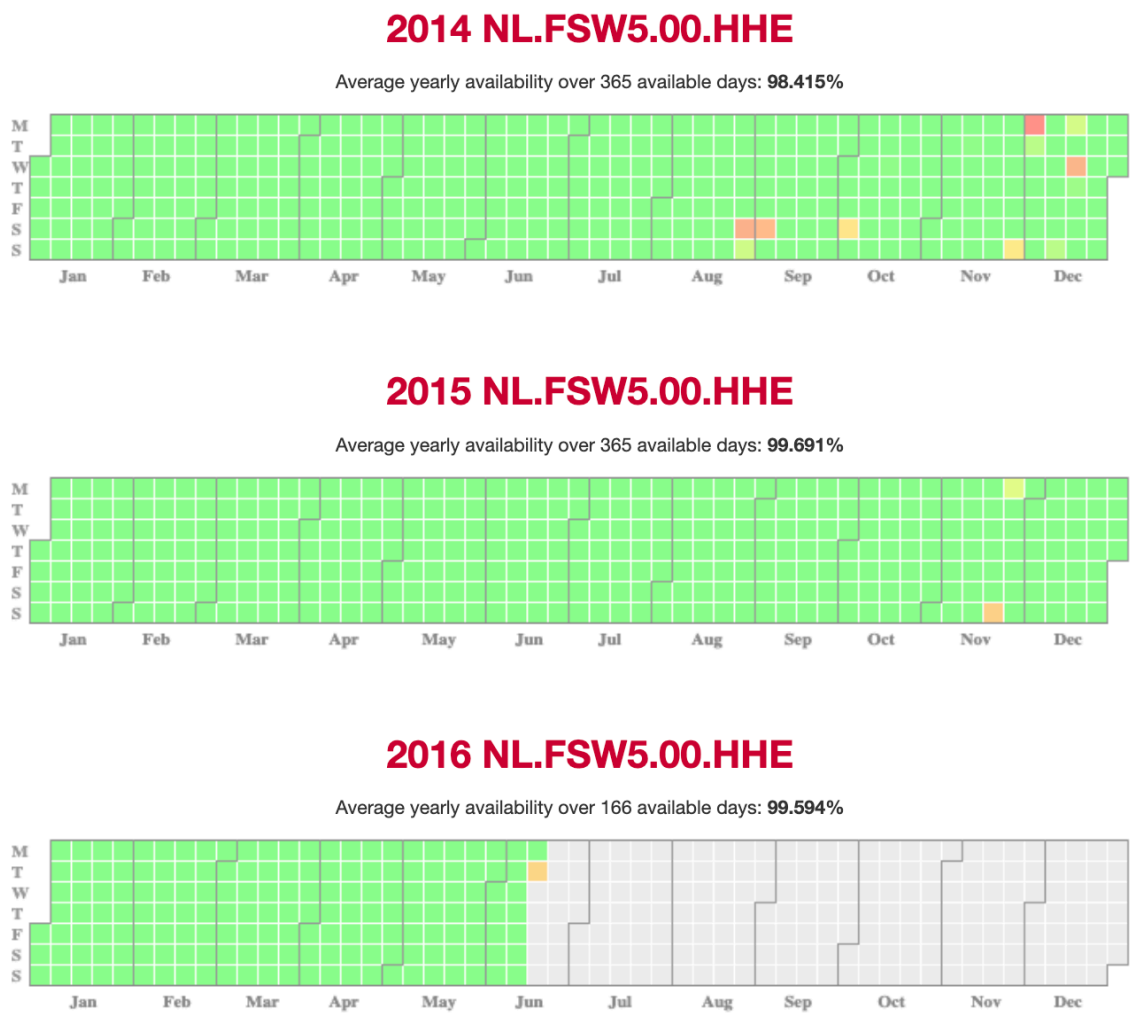

Figure C.2: *Daily data availability (percentages) of channel HHE of station FSW5 (continued). Color scale runs from red to green, with red indicating (almost) no data availability and green indicating (almost) 100% data availability. Grey indicates no metrics are available for that day (which in most instances probably implies that continuous recordings are unavailable). Days with 24 hours of data (100%) available are depicted with a star on top of them.*

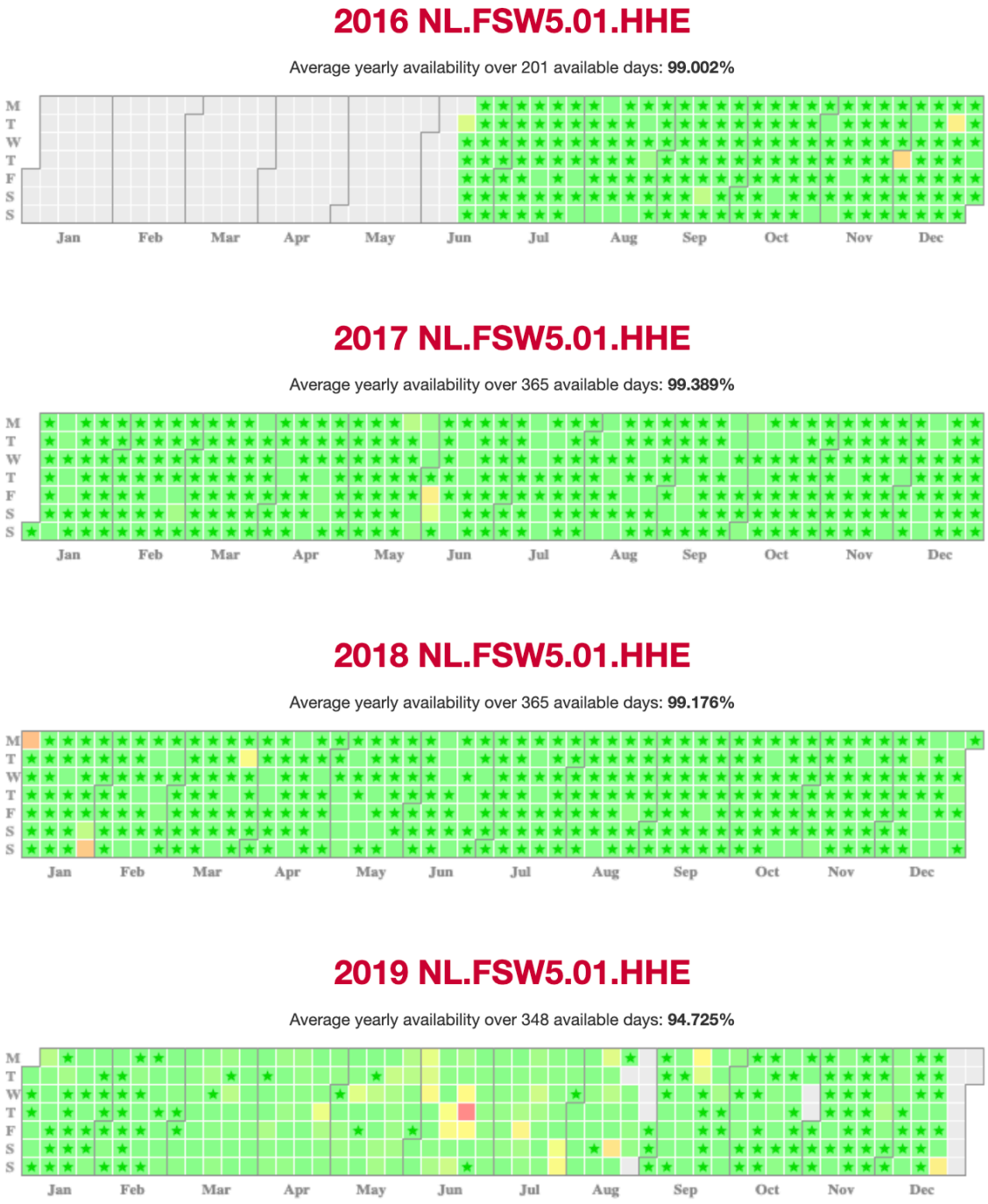

Figure C.3: *Daily data availability (percentages) of channel HHE of station FSW5 (continued). Color scale runs from red to green, with red indicating (almost) no data availability and green indicating (almost) 100% data availability. Grey indicates no metrics are available for that day (which in most instances probably implies that continuous recordings are unavailable). Days with 24 hours of data (100%) available are depicted with a star on top of them.*

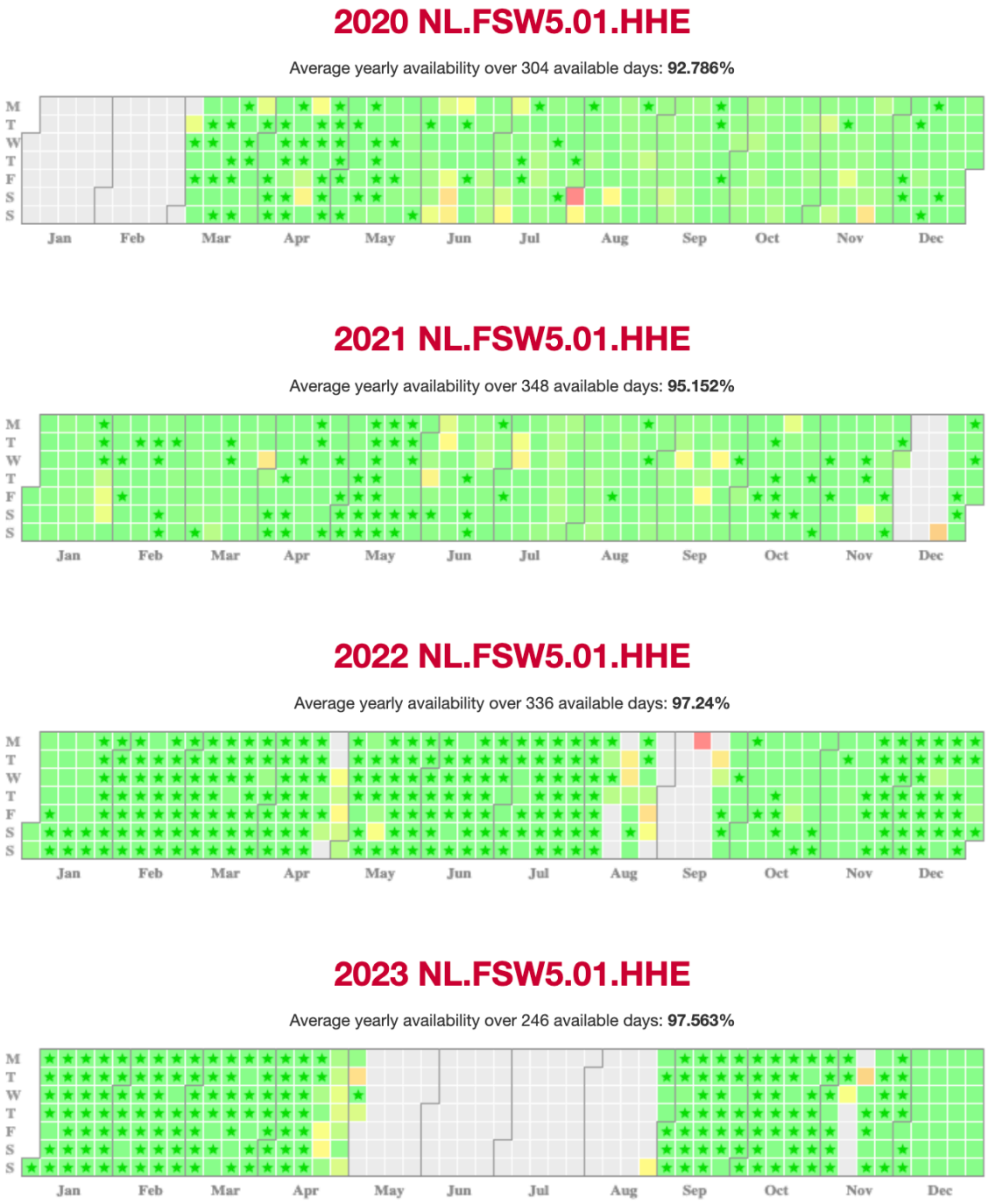

Figure C.4: *Daily data availability (percentages) of channel HHE of station FSW5 (continued). Color scale runs from red to green, with red indicating (almost) no data availability and green indicating (almost) 100% data availability. Grey indicates no metrics are available for that day (which in most instances probably implies that continuous recordings are unavailable). Days with 24 hours of data (100%) available are depicted with a star on top of them.*

Royal Netherlands Meteorological Institute

PO Box 201 | NL-3730 AE De Bilt
Netherlands | www.knmi.nl